BARYON DISTRIBUTIONS IN HIGH-ENERGY NUCLEAR COLLISIONS

A Dissertation Presented

by

James Dee

to

The Graduate School

in Partial Fulfillment of the Requirements

for the Degree of

Doctor of Philosophy

in

Physics

State University of New York
at
Stony Brook

May 1995

State University of New York
at Stony Brook

The Graduate School

James Dee

We, the dissertation committee for the above candidate for the Doctor of Philosophy degree, hereby recommend acceptance of the dissertation.

Johanna Stachel
Professor of Physics

Peter Paul
Professor of Physics

Edward V. Shuryak
Professor of Physics

Thomas W. Ludlam
Senior Physicist, Brookhaven National Laboratory

This dissertation is accepted by the Graduate School.

Graduate School

Abstract of the Dissertation

BARYON DISTRIBUTIONS IN HIGH-ENERGY NUCLEAR COLLISIONS

by

James Dee

Doctor of Philosophy

in

Physics

State University of New York at Stony Brook

1995

Inclusive double differential multiplicities $d^2N/dy\,dp_t$ and related quantities have been measured for protons and deuterons produced in 14.6 A GeV/c Si + Al and Si + Pb collisions using the E814 forward spectrometer at the AGS at BNL. Upgrades to the E814 apparatus and data acquisition system are described. An analytic method for cathode pad linearization is developed. Details of analysis, in particular momentum measurement and a precise geometric acceptance calculation, are described. Collision "centrality" is determined by measuring N_c, the total charged particle multiplicity in the pseudorapidity range $0.85 < \eta < 3.8$. For both systems Si + Al and Si + Pb, an increase in the proton rapidity distribution dN/dy at mid-rapidity and a corresponding decrease at higher rapidities are observed with increasing N_c. For Si + Pb, Boltzmann slope parameters T_B increase significantly in the most central collisions. The measured distributions exhibit a centrality dependence even when $\sigma/\sigma_{\rm geo} \lesssim 10\%$, where full overlap between the Si and Pb nuclei occurs in a simple geometric picture. The proton rapidity distribution dN/dy is presented for the symmetric system Si + Al over the entire rapidity interval. The total number of protons, which is the integral of this quantity over rapidity, varies with N_c. This number is corrected for the measured number of protons bound in deuterons and the multiplicity of protons lost to Λ^0 production, which is estimated via a detailed simulation. Results are compared with various model calculations, mostly using the hadronic cascade codes ARC and RQMD. No significant nuclear transparency is observed, indicating that large baryon and energy densities are produced in these collisions.

In loving memory of my late grandfather,

Merle Aubrey Schmidt,

1920–1992.

Contents

List of Figures

List of Tables

Acknowledgements

I want to apologize right away to the doubtless many people I am forgetting to acknowledge explicitly or even implicitly. I am indebted to so many that omissions are inevitable, and it is not for lack of appreciation or gratitude on my part. Often that which is most important is taken for granted. I beg your forgiveness.

I am forever grateful to my advisor, Johanna Stachel, for her unflagging support over the last several years. She refused to give up on me even on those not-rare-enough occasions when I was ready to give up on myself. I never would have finished this work without her help, financial suport, advice and friendship, and I owe her an enormous debt of gratitude.

To the rest of the Stony Brook Relativistic Heavy Ion Group, especially Professors Peter Braun-Munzinger and Tom Hemmick, I say thank you for putting up with me over the years. Your patience and indulgence did not go unnoticed, and I want to acknowledge it here.

To the Stony Brook people as well as the rest of the E814/E877 Collaboration I also owe essentially everything even remotely related to my work. I may have pulled my weight, but the experiment only runs because of the sweat and sleepless nights of dozens of people from all over the world. If I haven't said it before, now is the time: thank you.

To Stony Brook friends, both past and present, town and gown, I owe my sanity. Stress has been known to accompany large research projects, years of living in poverty as a student, uncertainty about the future, and all that graduate school is heir to. If not properly checked it can wear down the strongest among us. I would long ago have been packed off in a straitjacket if I hadn't on occasion been first packed off to the Checkmate Inn, that least savory of Setauket public establishments I'm pleased to have called my living room. To those who did the packing and saved me, who shared so many hard times with me, who plodded through it all beside me, and who even sometimes picked me up and carried me, I offer my humblest, most sincere thanks. You are too many to list here without requiring a second volume, but you know who you are, and you know you have my undying gratitude.

Finally, to my friends and family elsewhere, especially both my parents, though you haven't been present in body, your presence in spirit is responsible for much of what I have done and become here. You have lent me invaluable support in many forms—material, financial, emotional—and without it I could never even have considered undertaking this task. Thank you all.

"Jessica tells me you're—ah—a *math chap?*"

"Little sigma, times P of s-over-little-sigma, equals one over the square root of two pi, times e to the minus s squared over two little-sigma squared."

"Good Lord." Laughing, hastily checking out the room.

"It is an old saying among my people."

from *Gravity's Rainbow*
by Thomas Pynchon

Chapter 1

Introduction

1.1 Background and Motivation

Study of the distribution of baryons after ultrarelativistic heavy ion collisions can yield important information about the energy densities achieved. In particular, the distribution dN/dy of baryons in rapidity $y \equiv \frac{1}{2}\ln[(E + p_z)/(E - p_z)]$—where p_z is the longitudinal component of momentum, E is the energy, and the speed of light c is the unit of velocity—is directly related to the energy loss by the target and projectile nucleons during the collision. At very high energies, where the interval between the target and beam rapidities is large, even sizeable rapidity shifts of the nucleons (*e. g.,* $\Delta y \approx 2$, implying that the nucleons lose more than 90% of their energy during the collision) will leave the region of phase space near the center-of-momentum rapidity (*mid-* or *central rapidity*) nearly empty. This implies small baryon density at central rapidity; target and projectile are "transparent" to each other.[1]

---

[1] See, *e. g.,* Anishetty, Koehler and McLerran [Ani 80] or Bjorken [Bjo 76].

At lower energies, however, the rapidity interval between target and projectile is small, so transparency will imply small rapidity shifts, and thus little energy loss and low energy density. Baryon phase-space distributions offer information on the degree of transparency or its opposite—stopping—present in nuclear collisions. Initially, the target and projectile protons have rapidity distributions centered at $y_T = 0$ and $y_P = 3.44$, respectively, with widths of about 0.17 rapidity units from Fermi motion, and a rapidity density $dN/dy = 0$ in between these two peaks. If the nuclei were highly transparent to each other, one might expect to see some broadening and small shift toward mid-rapidity of the initial distributions and a sparse population of the central rapidity region in the final state; the final proton distribution would exhibit peaks at or near target and beam rapidities. On the other hand, if the nuclei, colliding at zero impact parameter, are fully stopped, one would expect most of the nucleons at mid-rapidity, with the width of the distribution determined by thermal and possibly hydrodynamic motion, and no peaks in the beam and target regions. Proton transverse momentum distributions $d^2N/dy\,dp_t$ offer a measure of the amount of equilibration or thermalization the system undergoes and reflect the actual temperature in a thermal model.

We wish to study the behavior of nuclear matter under extreme conditions. Fig. 1.1 shows schematically a phase diagram for nuclear matter. It has long been supposed[2] that at high temperatures and densities, nuclear matter enters

---

[2]See, *e. g.,* Refs. [Qua 82a, Qua 82b] and references therein, in particular Refs. [Fre 77, Kap 79, Shu 79, Shu 80, Raf 81].

Figure 1.1: Schematic phase diagram for nuclear matter. The dark spot at $T = 0$, $\rho = \rho_0$ represents normal nuclear matter in its ground state, where $\rho_0 \approx 0.17/\mathrm{fm}^3$ is the baryon density of an ordinary nucleus. The dashed curve represents a boundary between the low-temperature and -density hadronic phase and the hypothetical high-temperature and -density deconfined phase; T_c and ρ_c represent the critical temperature and density, respectively, at which the transition might occur. The solid curve illustrates the likely path taken by nuclear matter in the course of AGS heavy ion collisions.

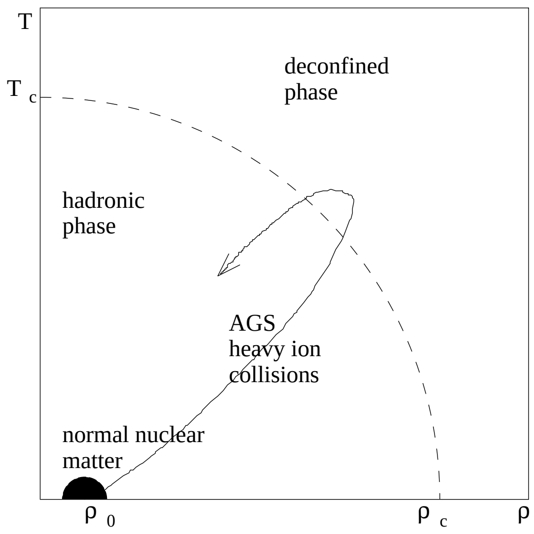

a phase different from the ordinary hadronic phase in which constituent quarks are bound together in color-neutral baryons and mesons. In this "deconfined" phase, because of the asymptotic freedom of the strong nuclear interaction between quarks and the considerable overlap among quark wave functions at high densities, quarks would no longer be confined to individual hadrons, but would be free to move in an extended volume. This hypothetical new phase has been dubbed the *Quark-Gluon Plasma* and is the subject of much speculation and investigation.[3]

There has been much speculation and controversy in recent years on the issue of transparency and baryon density at the AGS. Though it was initially supposed that projecile nucleons would lose about 2.5 rapidity units in heavy ion collisions and that the stopping regime would persist somewhat beyond AGS energies (14.6 A GeV/c/nucleon) [Bus 84, Dat 85], interpretations of early data published by Experiment 802 [Abb 90, Abb 91] suggested that the nuclear scattering length might be greater than 20 fm, resulting in very little energy loss by participant nucleons.[4] The analysis of Experiment 814 data presented here and elsewhere [Bar 90, Bar 92a, Bar 93a, Dee 93, Bar 94b] yields strong evidence that the in-medium nuclear cross section is large, that participant nucleons undergo several collisions in a heavy ion collision and that

[3]See, *e. g.,* the proceedings of the *Quark Matter* International Conferences on Ultra-relativistic Nucleus-Nucleus Collisions from 1983 to 1993 and references therein.

[4]See Chapman and Gyulassy [Cha 91, Cha 92] and the discussion at the end of Ch. 6.

large baryon densities and temperatures are achieved in these collisions.

1.2 Useful Quantities

We always work in units where the speed of light $c = 1$, unless otherwise specified. Consequently, mass, momentum and energy are all measured in the same units: electron Volts (eV). Sometimes we introduce one or more factors of c when discussing a specific value to emphasize that it is either a mass, a momentum, *etc.* Time and distance are measured in femtometers (fm), also called Fermi. Again, sometimes when discussing a time interval, we will measure it in fm/c to emphasize that it is a time instead of a distance. Sometimes we also use units where the charge e on the proton is unity (see App. D).

When characterizing individual particles, we often use the *transverse momentum* p_t and the *longitudinal momentum* p_l or p_z. These are defined with respect to the beam axis. We define the *transverse mass* $m_t \equiv \sqrt{m^2 + p_t^2}$. We define the *rapidity*

$$y \equiv \frac{1}{2} \ln \frac{E + p_z}{E - p_z}, \tag{1.1}$$

where the energy $E = \sqrt{m_t^2 + p_z^2}$. We also define the *pseudorapidity*

$$\eta \equiv -\ln \tan \frac{\theta}{2} \tag{1.2}$$

where θ is the usual polar angle. See App. A for a more detailed discussion of the rapidity and pseudorapity variables.

1.3 Simple Models

A purely thermal (Boltzmann) model predicts that the number d^3N of particles of a given species produced into an element of phase space d^3p satisfies

$$\frac{d^3N}{d^3p} \propto \exp\left(-\frac{E-\mu}{T}\right), \tag{1.3}$$

where T is the temperature of the source, E is the center-of-momentum energy associated with d^3p, and μ is the chemical potential. Expressed in terms of the invariant multiplicity, rapidity and transverse mass $m_t \equiv \sqrt{m^2+p_t^2}$, one finds

$$\frac{1}{p_t}\frac{d^2N}{dp_t\,dy} = \frac{1}{m_t}\frac{d^2N}{dm_t\,dy} = A_B(y)\frac{m_t}{m}\exp\left(-\frac{m_t-m}{T_B(y)}\right), \tag{1.4}$$

where $A_B(y) \propto m\cosh(y-y_{\rm cm})\exp(\mu/T - m/T_B(y))$ is the $p_t = 0$ intercept of the function at rapidity y, $y_{\rm cm}$ is the center-of-momentum rapidity of the "fireball," and $T_B(y) = T/\cosh(y-y_{\rm cm})$. This rapidity dependence of A_B and T_B only holds if the "fireball" emits particles isotropically. If the emission is not isotropic, the shape of the rapidity distribution and of $T_B(y)$ may vary, but if the system thermalizes, one still expects to see the general behavior indicated by Eq. (1.4).

Another convenient parametrization is

$$\frac{1}{p_t}\frac{d^2N}{dp_t\,dy} = \frac{1}{m_t}\frac{d^2N}{dm_t\,dy} = A_0(y)\exp\left(-\frac{m_t-m}{T_0(y)}\right), \tag{1.5}$$

which does not have a direct physical interpretation, but is often used to parametrize charged particle spectra in high-energy collisions. We will consider both these parametrizations later on.

Chapter 2

Apparatus

The data presented here were obtained in March, 1991, with the E814 apparatus (Fig. 2.1), most notably its forward spectrometer, at the Alternating Gradient Synchrotron (AGS) at Brookhaven National Laboratory (BNL). Silicon ions from a tandem Van de Graaff accelerator are fed to the AGS by a heavy ion transport line and accelerated to 14.6 GeV/c/nucleon. These ions are extracted from the AGS in spills of approximately 1 s every 3–4 s and magnetically steered down several beam lines onto targets in the the various experimental areas. In this work, we will discuss collisions of Si nuclei with targets of aluminum (2.3% nuclear interaction length) and lead (1.2% and 2.4% nuclear interaction length) in the C5 beam line. Information about the targets used is listed in Tab. 2.1.

In what follows, we will refer to a right-handed coordinate system defined with origin at the intersection of beam and target, the z axis in the direction of the incident beam and y axis vertically upward. Consequently the x axis points to the left if the experiment is viewed from the vantage of the incident beam.

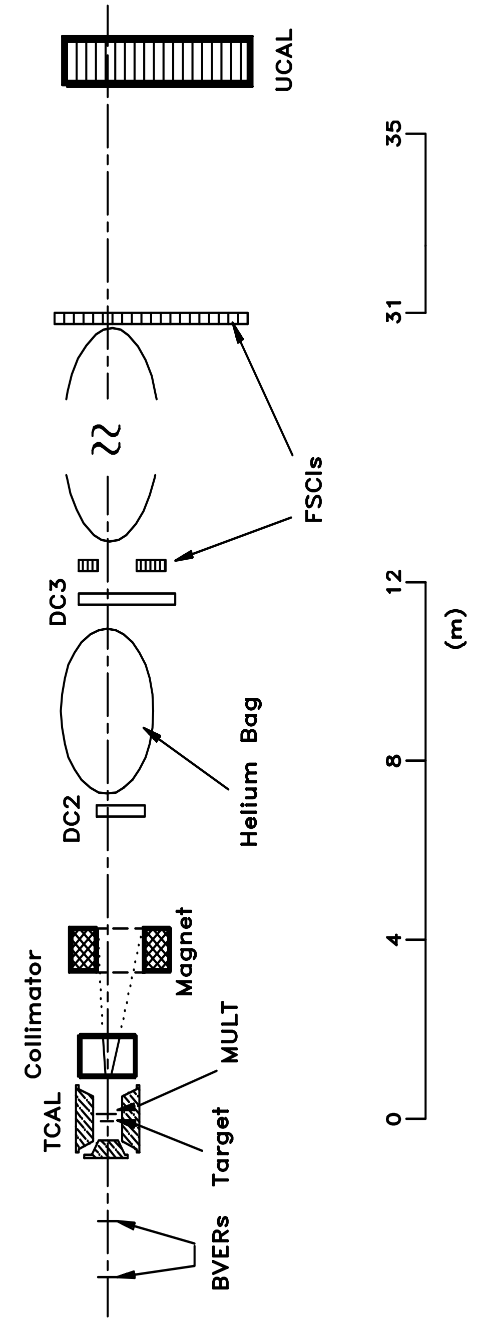

Figure 2.1: The E814 apparatus.

Target	Int. Length (^{28}Si) (%)	Scatt. Dens. (10^{21}/cm^2)	Mass Dens. (g/cm^2)	Thickness (mm)	Rad. Length (%)
Al	2.31	14.0	0.628	2.33	2.62
Pb	1.20	3.30	1.140	1.00	17.9
Pb	2.38	6.55	2.263	1.99	35.5

Table 2.1: For the three targets used: fraction of an interaction length for ^{28}Si; scattering center density; mass density; thickness; and fraction of a radiation length.

Most detectors in Fig. 2.1 extend farthest from the z-axis in the negative x direction.

In this portion of the 1991 run and in subsequent runs of E814 and E877, based on a design study I performed, we modified the E814 apparatus from its previous configuration, which used the 1 m thick participant calorimeter (PCal), standing 74 cm from the target, to collimate particles entering the spectrometer. A small hole in the calorimeter limited the acceptance to $\theta \lesssim 14$ mrad. This small acceptance permitted the use of two long spectrometer magnets—about 1 and 2 m long—for strong deflection. The experiment was originally designed to study electromagnetic dissociation of relativistic Si projectiles. The projectile fragments in peripheral nuclear collisions are highly relativistic, so a large magnetic field integral $\int B \cdot dl$ was needed to deflect these very rigid particles significantly, and the magnets were usually run very near full current.

For this portion of the 1991 run, we replaced the PCal with a lead collimator that accepts particles emitted into $-115 < \theta_x < 14$ mrad and $|\theta_y| < 21$ mrad, an acceptance much larger than that of the PCal opening ($\theta \lesssim 14$ mrad). We also removed the second spectrometer magnet and ran the first at about 10% of its maximum current. Because we wished to study lower momentum particles, we wanted a smaller field integral. We also shifted the first magnet in the negative x direction. All this served to extend considerably the acceptance of the forward spectrometer in p_x and hence transverse momentum. Also, the much smaller field integral allowed us to accept particles of much lower momenta and consequently extended the low-p_t acceptance to lower rapidities.

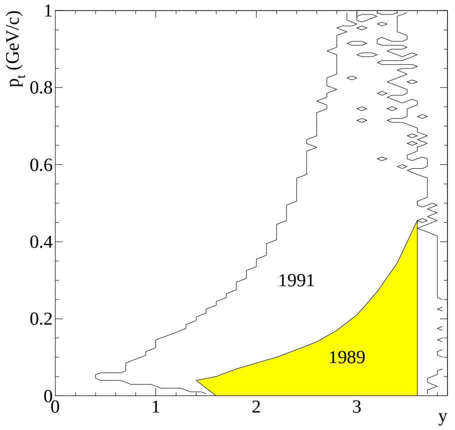

Figure 2.2: Proton acceptances in 1989 and 1991.

This is illustrated in Fig. 2.2, where we have plotted the proton acceptance from 1989 [Bar 92a] along with that from 1991.

Table 2.2 lists z positions of several of the detector systems used in this analysis. The detectors are described below.

2.1 Target Area

Upstream of the target are located two silicon microstrip beam vertex detectors (BVERs) with 50 μm pitch between strips that run in the y direction. These measure the incident beam trajectory in each event. The multiple-scattering dominated resolution is about 40 μrad in the incident beam angle and 80 μm in the x coordinate of the beam at the target.

Transverse energy is measured in the pseudorapidity ranges $-2 < \eta <$

Table 2.2: Detector and magnet z coordinates

detector	z (cm)
MULT	3.4
Magnet Front	263.4
Magnet Back	354.8
DC2	692.2
DC3	1156.3
FSCI Upstream	1211.4
FSCI Downstream	3133.7

-0.9 and $-0.5 < \eta < 0.8$ by the target calorimeter (TCAL), an electromagnetic calorimeter composed of 992 NaI(Tl) crystals.

A silicon pad detector (MULT) located downstream of the target measures the total multiplicity of charged particles in the pseudorapidity range $0.85 < \eta < 3.8$. This detector is discussed in detail in Ref. [Bar 92b].

2.2 Forward Spectrometer

Charged particles produced in the forward direction either stop in the collimator or pass through its aperture to be momentum-analyzed by the dipole spectrometer magnet and detected by two tracking chambers (DC2 and DC3), each of which has six drift planes with 300 μm resolution in the x direction. Each also has a segmented cathode plane with chevron-shaped pads providing measurement of the y coordinate with resolution varying from 2.3 to 36 mm [Gre 92]. The size and corresponding resolution of the pads varies across each chamber according to the anticipated density of charged particle tracks.

After passing through the tracking chambers, charged particles are detected by a hodoscope of 10 cm wide plastic scintillation counters (FSCIs). One group of these scintillators sits 12 m from the target and has better than 200 ps time resolution; the second set sits 31 m from the target and has 350 ps resolution. The relative mass resolution due to the time resolution δt is $\delta m/m = (\delta t/z)\,\beta\gamma^2$. For the downstream counters, from which most of the present data are obtained, $\delta t/z = 0.3\%$. Since all particles accepted in the spectrometer are close to minimum ionizing or higher in momentum, the pulse height from the scintillators allows measurement of the magnitude of the charge of each particle striking them. The empty space between DC2 and DC3, as well as that between DC3 and the downstream scintillators, is occupied by bags of helium to minimize the effects of reinteraction and multiple scattering.

Finally, sets of uranium/copper/scintillator hadronic calorimeters are located 12.7 and 36.3 m from the target and measure the kinetic energy of most particle species striking them. Some particle species annihilate in the calorimeters, so their rest energy is measured as well. This measurement was not used in this analysis.

Chapter 3

Data Acquisition and Monitoring

3.1 E814/E877 Data Acquisition

In E814 and E877, digitized data is read out using the Fastbus and CAMAC electronics protocols. An SSP (SLAC Scanner Processor) [Bra 84, Bar 85] resides in each Fastbus crate. During an event each SSP collects data from the Fastbus electronics (*e. g.,* ADCs and TDCs) in its crate. A master SSP known as SSP0 polls all the lower level SSPs and the CAMAC electronics for data, assembling the entire event and passing it onto the main data acquisition (D/A) computer, where it is recorded to tape or sent off to other computers for analysis, as illustrated in Fig. 3.1.

The SSPs run a program called SSPDAQ [Hac 89]. This includes an interpreter that allows flexible programming of the SSPs. SSP0 reads a "device list": an ASCII file containing a sequence of instructions. It passes these instructions on to the appropriate slave SSPs, which read, write and clear different addresses in the sequence specified by the device list. At the end of

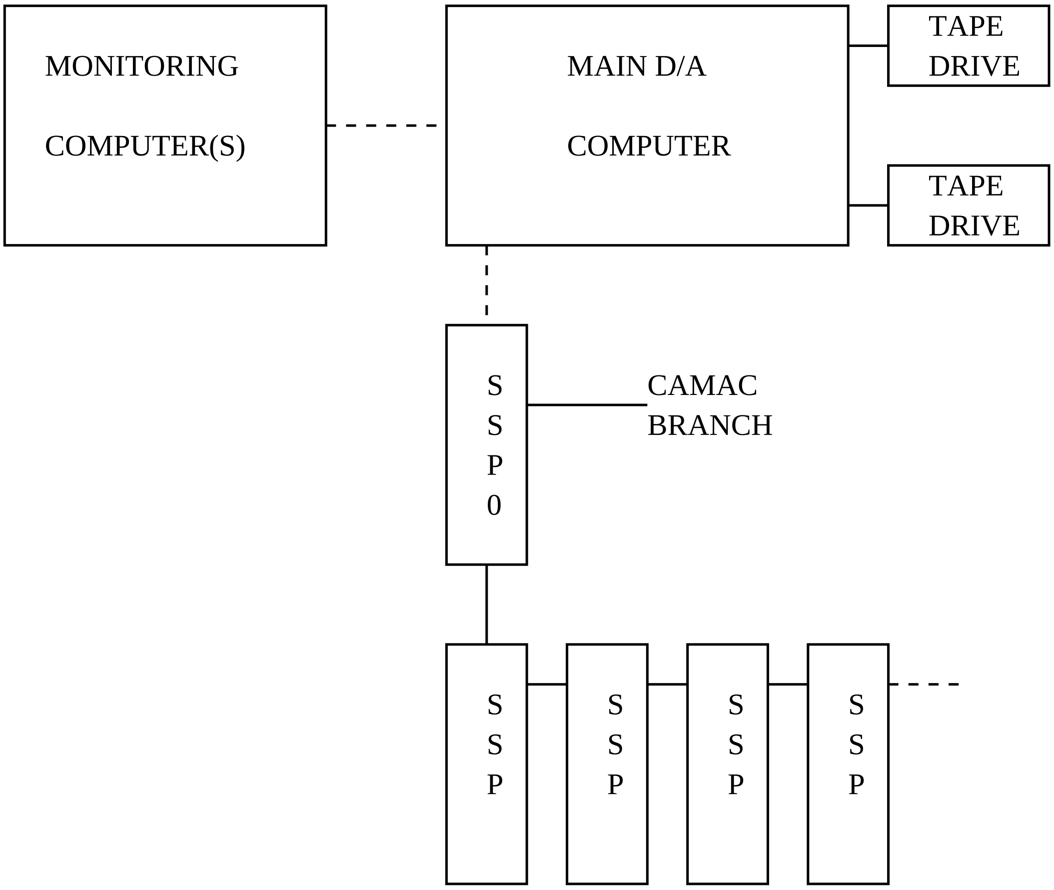

Figure 3.1: Schematic overview of the E814/E877 data acquisition and monitoring system.

the event, SSP0 collects the data and associates Logical Identifier (LID) words with sets of ADCs, TDCs, scalers, *etc.,* corresponding to different detectors. This allows easy identification of the data modules during later analysis.

E814 in its original form drove SSP0 from a DEC MicroVAX 3900 series server that wrote data from SSP0 to 9-track, 6250 b. p. i. magnetic tapes. The data tapes were copied to physically smaller, larger capacity 8 mm video cassettes as this technology became available. A 9-track reel holds about 140 MB, while an EXABYTE 8200 drive will write 2.2 GB to an 8 mm tape. The higher-density 8500 drives write as much as 5 GB on a single cassette without data compression. Typically about 12 9-track reels were copied onto a single low-density 8 mm tape. This made later analysis much more convenient.

The data acquisition in E814 was originally handled using a number of large, complex software packages, including the VAXONLINE suite from FNAL (Fermi National Accelerator Laboratory), written in a variety of languages, usually FORTRAN or assembler. For the last run of E814 and all runs of E877, the data acquisition was run from a VME crate containing a CES Fast Intelligent Controller (FIC) 8232 with a Motorola 68030 CPU on board. The Motorola runs the OS-9 operating system, reads SSP0 using a Fastbus-VSB Interface (FVSBI) and writes data directly to SCSI EXABYTE 8500 drives in the VME crate, as illustrated in Fig. 3.2. The data acquisition code was totally rewritten in the C programming language. It is much smaller and more uniform than the previous version, allowing greater ease of use and making it easier to debug. The ability to write directly to 8 mm video cassette improves the overall efficiency of the experiment. Formerly, a tape was filled every 15 or

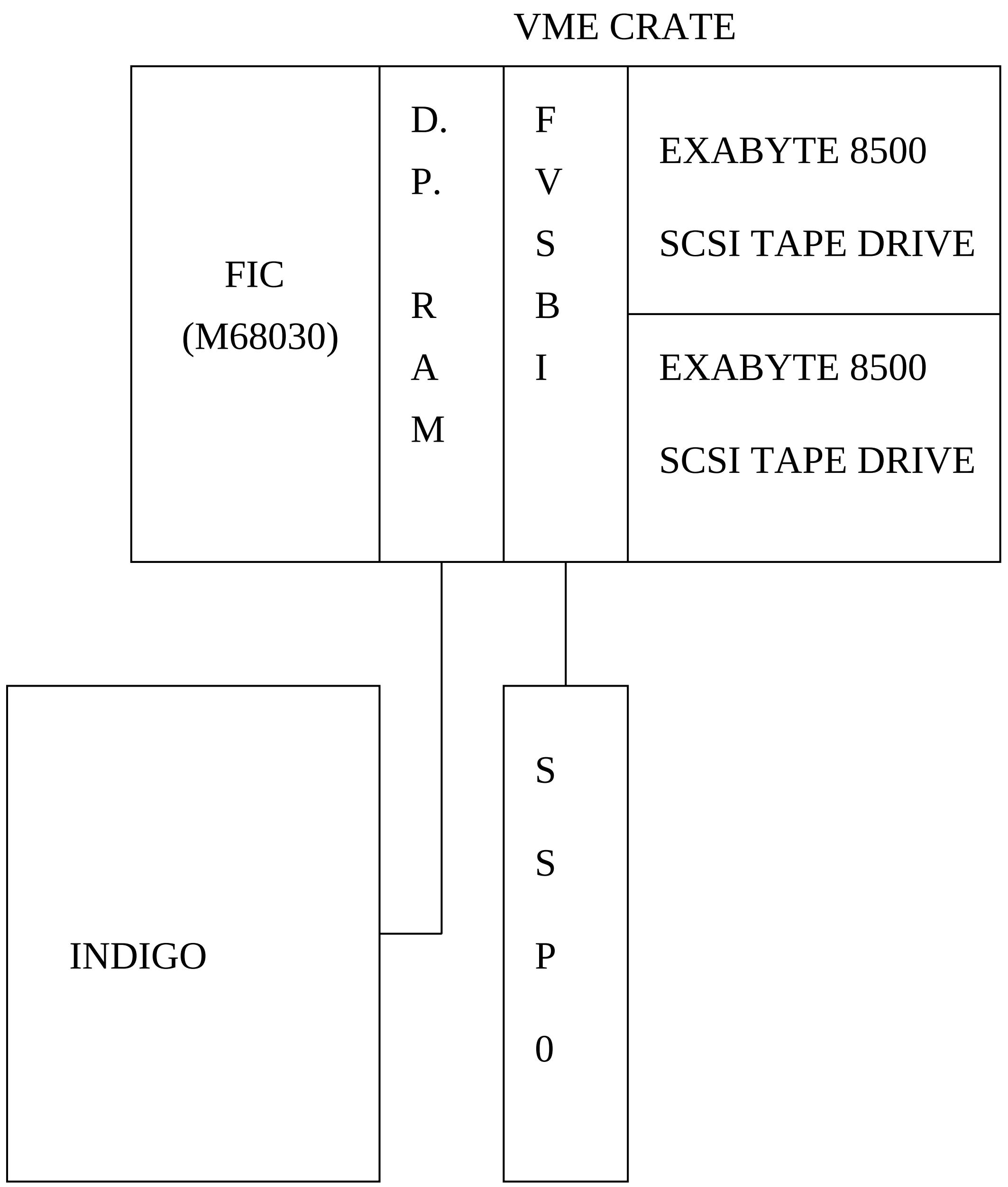

Figure 3.2: Detail of the E877 data acquisition and monitoring system.

20 minutes, requiring a shift crew to spend most of their time changing tapes. Now tapes run for at least two hours before acquiring 1.8 GB. Also the tape copying process is greatly improved, and much less physical tape storage space is required.

3.2 STEP1 and E877 Online Data Analysis

In E814, online data monitoring was done using the VAXONLINE Pool/ Consumer system from Fermilab on DEC VAXstations. This scheme involved multicasting of event buffers over ethernet by the data acquisition system. These multicast events were read off the network by a *producer* process on each workstation and stored in a global memory section called a *pool.* Client processes called *consumers* requested events from the pool and analyzed whatever portion of them was desired.

Offline analysis of E814 data was done using a software package developed for E814 called STEP1. This package was intended to analyze many different data formats, including the ZEBRA format used by CERN software, but initially it could only read one particular format. A program called STEP0 was run to convert the data to the universal STEP1 format. Early in its evolution, STEP1 assimilated STEP0 and became capable of reading any of the available data formats, though only the raw data format used by the D/A is routinely used.

Once the data are read in, either from tape or disk, STEP1 "unpacks" data modules, copying them to memory locations where they are accessible to user subroutines. Unpacking routines scan the raw data buffers, looking for LID words corresponding to different detectors. Having identified any particular detector, the unpack procedure copies the corresponding data into the appropriate memory location. User routines are called at appropriate points, once the data are in place.

By contrast, online users were provided with raw data buffers, writing their own "unpacking" routines to identify data they were specifically interested in. These routines were generally written only to serve a user's particular purpose and were not flexible enough to be useful in an offline analysis library, so STEP1 had to develop its own unpacking routines independently of the online analysis. This dichotomy led to some repetition of effort.

For the first run of E877, I and other collaborators redesigned the online data analysis scheme. The analysis is done on a Silicon Graphics, Inc., (SGI) Indigo workstation which originally had a 100 MHz MIPS R4000 CPU rated at about 60 SPEC marks (1 SPEC $\approx$ 1 MIPS), a factor of 15 or 20 increase in CPU speed over a VAXstation 3100/38. This workstation has since been upgraded to a 150 MHz R4400 CPU rated at about 90 SPECs. In addition, we use a BIT3 VME/GIO dual-port RAM interface that sits in the data acquisition VME crate (see Fig. 3.2). A cable running to a board on the Indigo makes this interface look like 8 MB of RAM both to the Indigo and to the Motorola data acquisition computer.

While collecting data, the Motorola stores events in a circular buffer in the BIT3 interface. A server process on the Indigo responds to client requests for data by reading events from the circular buffer directly. Clients use the

RPC (Remote Procedure Call) package to communicate with the server. This package allows procedures to be executed by other processes. Effectively, a procedure call is made in the (local) client process and the procedure is executed in the (remote) server process. The server returns a copy of data from the circular buffer in the BIT3 interface to the client process.

The server was designed to ensure that while a client never gets the same event twice, several clients may access the same data. In order that n clients will not be limited on the average to a fraction $1/n$ of the data, the server was designed to store a single event in memory and to keep a list of the clients that have already seen the event. It reads a new event only if it has none in memory or if the requesting client has already seen the current event. Otherwise, it returns to the client a copy of its current event. This way, two clients may analyze the same data in parallel and not restrict each other.

Client processes use the STEP1 package to analyze the data, just as is done with data on tape after a run. This allows considerable flexibility and uniformity in analysis. Code developed during a run may be applied directly to data analysis offline. Even during a run, after analyzing data online, one may use the same program without recompilation to analyze data from a tape simply by changing an input parameter. This improves code uniformity and prevents repetition of effort.

The use of a dedicated data link (the BIT3 interface) and request-driven online analysis have also drastically improved the efficiency of the system. To begin with, data no longer travels over the ethernet, so it does not compete with normal network traffic. The network is not saturated, and data analysis is not hindered by other routine tasks. And because the RPC server only reads data when it is requested by a client, CPU cycles and bandwidth are not wasted reading unwanted data. The current analysis efficiency is between 30% and 60%, depending on operating conditions, analysis complexity, *etc.,* constituting an increase of about two orders of magnitude over the previous scheme.

The offline form of STEP1 was substantially improved at this stage too. Originally STEP1 was run mostly on VAXes, and data from tape was read using a CERN subroutine called VAXTIO, handling generic tape I/O on VAXes. When STEP1 was originally ported to Unix machines, E814 developed an alternative to VAXTIO. UNXTIO was written using Unix system calls, associating a stream with the tape drive file descriptor and reading the variable-length records off the tape.

When the E814 data acquisition was moved to the Motorola, the data structure was changed. The OS-9 SCSI tape device driver only wrote fixed-length records. We knew the optimal record length from the helical scan on the EXABYTE 8200 drives to be 1024 bytes. We also knew that the 8500 drives wrote twice as much data in the same space: the physical motion of the head was no different. So we decided to use 2048 bytes as the record length for E814/E877 data tapes. The variable-length event buffers now span several tape records (up to 16), so the tape-reading routine had to be modified.

The optimal I/O buffer size for streaming the EXABYTE drives is 128 kB, or 64 records. This is several times the maximum event buffer length of 32 kB (a typical buffer is 16-20 kB). Reading single event buffers with each read would not enable us to stream the drives and run them at their maximum speed (480–500 kB/s for the 8500 drives). I rewrote UNXTIO to implement a large, 128 kB internal buffer. This fixed amount is read with every system call, and individual calls to UNXTIO return individual event buffers, reading only when necessary. This approach increased the tape analysis speed to the maximum allowed by I/O—a factor of about 6 from the previous approach. I used a similar approach to improve the copying speed dramatically. This became a significant factor when a typical E814/E877 run recorded more than 200 8 mm tapes. At the maximum speed, each tape takes an hour to copy. The copying speed increase turned weeks into days.

Note that this approach would not have been possible without the change in data structure. Multiple records may not be read simultaneously with a single call if the data is variable-length; each call returns a single record. So an EXABYTE drive cannot be operated in stream mode with a variable-length device driver. Note also that this would be impossible on a VAX, since the VMS SCSI tape driver only drives the EXABYTEs in TK50 emulation mode, and cannot stream the drives either.

Chapter 4

Data Analysis

4.1 Per-Event Quantities

Several quantities are measured on an event-by-event basis. The quantities used here are the charged particle multiplicity N_c and the incident beam particle trajectory in the bend plane of the dipole magnet.

The total charged particle multiplicity in the forward direction is measured by the muliplicity detector, whose acceptance is $0.85 < \eta < 3.8$ as reported in Sec. 2.1. The multiplicity N_c is used as a "trigger" variable. Fast electronics measure this quantity immediately when a collision is detected. If it is above a certain threshold, the event is written to tape. Several parallel triggers with different thresholds were taken at different rates; *i. e.,* those that occurred more frequently were downscaled.

For Si + Al, only one trigger was analyzed, corresponding to the top 27.5 mb of the cross-section. This is 1.67% of the geometric cross-section $\sigma_{\text{geo}} \equiv \pi r_0^2 (A_T^{1/3} + A_P^{1/3})^2$ where A_T is the number of nucleons in the target

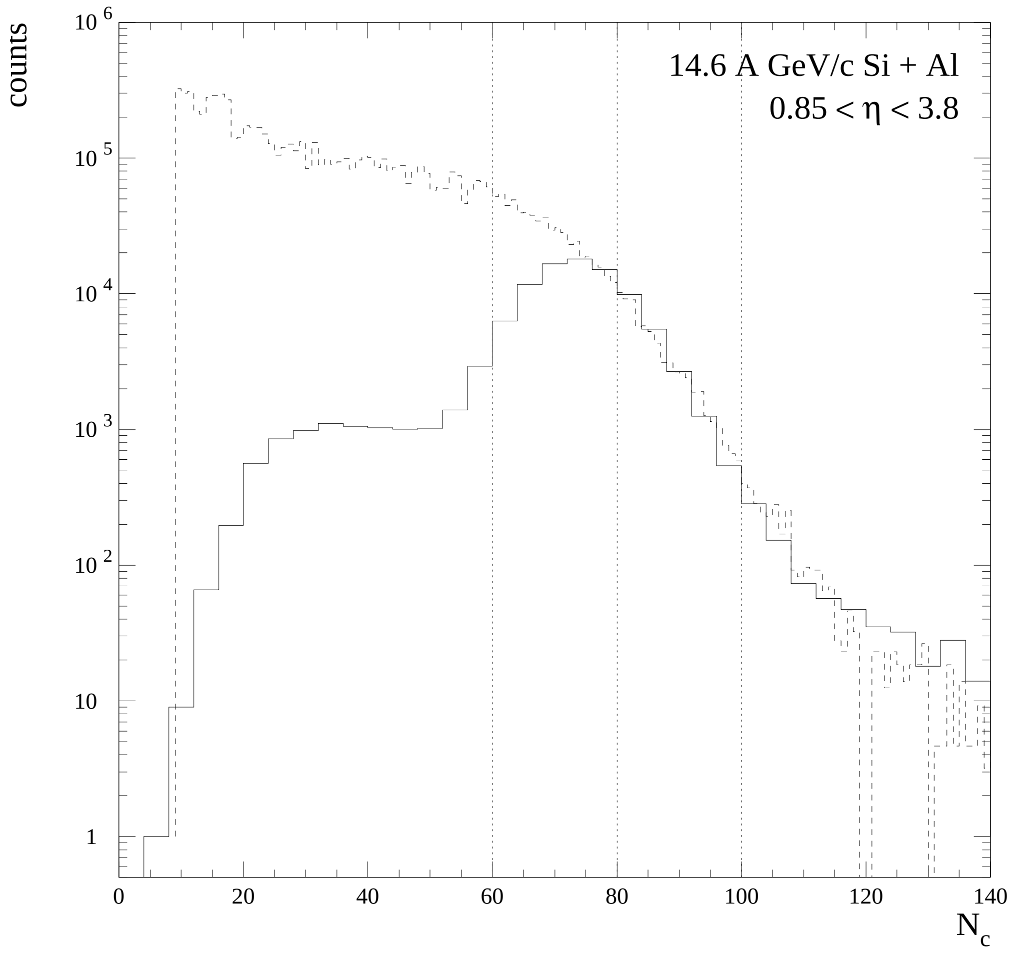

Figure 4.1: Distributions of charged particle multiplicity N_c in $0.85 < \eta < 3.8$ from Si + Al collisions for the high multiplicity trigger. Vertical dotted lines delimit the N_c bins used in the analysis. The dashed curve is the minimum bias N_c distribution on the same scale as the triggered data [Bar 92b].

N_c	$\sigma/\sigma_{\text{geo}}$	N_{ev}
60–80	1.7%	85268
80–100	0.19%	20181

Table 4.1: Multiplicities and centralities in Si + Al.

nucleus (27 for Al, 208 for Pb), $A_P = 28$ is the number of nucleons in the projectile nucleus and $r_0 = 1.2$ fm. The geometric cross-section $\sigma_{\text{geo}} = 1.649$ b for Si + Al. The multiplicity distribution from this trigger is shown in Fig. 4.1 along with dotted lines indicating the N_c bins used in the analysis and a minimum bias multiplicity distribution from Si + Al [Bar 92b]. Below $N_c \approx 60$, the events became unanalyzable because of the large multiplicities of projectile spectator protons in the spectrometer in these peripheral collisions. The fraction of the geometric cross-section above the middle of the bin and the number of events are shown in Tab. 4.1 for each of the N_c bins used.

Figure 4.2 shows multiplicity distributions for two triggers with different N_c thresholds in Si + Pb with the 1.2% interaction length target. In the upper panel are plotted the distributions of actual numbers of events written to tape by each of the two triggers. The trigger with the lower threshold is downscaled by a factor of 6; only every 6th event that satisfied this trigger was accepted by the data acquisition system.

The bottom panel of Fig. 4.2 shows the distribution from the higher

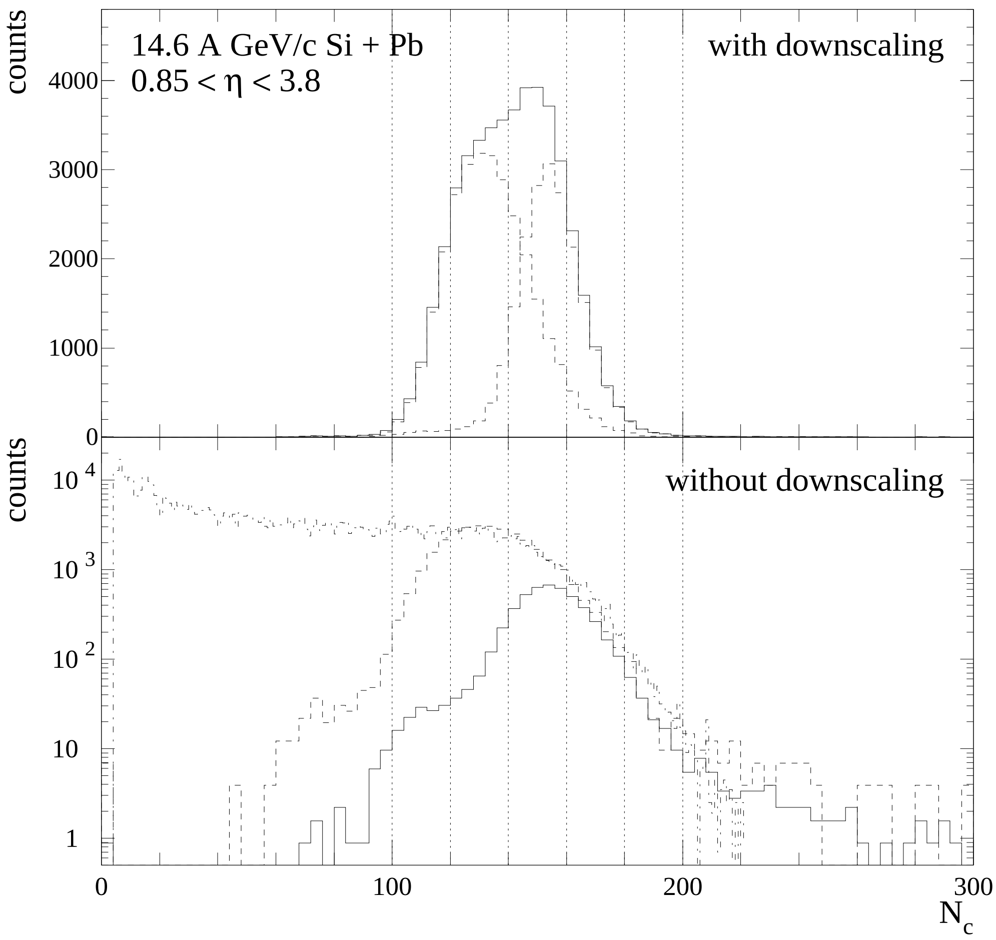

Figure 4.2: Distributions of charged particle multiplicity N_c in $0.85 < \eta < 3.8$ from Si + Pb collisions. In the upper panel, the two dashed curves are the number of events per unit N_c recorded on a tape for each of two triggers with different N_c thresholds. The trigger with the lower threshold is downscaled by a factor of 6. The solid curve is the sum of the other two curves. In the bottom panel, the solid curve is the higher threshold trigger again, while the dashed curve is the lower threshold trigger multiplied by 6. Vertical dotted lines delimit the five N_c bins used in the analysis. The dot-dashed curve is the minimum bias N_c distribution [Bar 92b] on the same scale as the triggered data.

threshold trigger and the distribution from the lower threshold trigger corrected for downscaling, *i. e.,* multiplied by 6. Downscaling allows us to measure the more probable portion of the distribution with the lower threshold trigger while collecting good statistics with the higher threshold trigger on the less probable tail of the distribution. Note that though these data are taken by triggering on an N_c threshold, the lower edges of the distributions are not sharp. This is due to the accuracy of the fast electronics in measuring the analog signal. Also shown is a minimum bias multiplicity distribution from Si + Pb [Bar 92b]. The higher threshold trigger contains 72.3 mb of the total cross-section, or 1.99% of the geometric cross-section ($\sigma_{\text{geo}} = 3.636$ b for Si + Pb, where $A_T = 208$). The lower threshold trigger constitutes 460 mb, or 12.6% of the geometric cross-section.

We analyze data in the five N_c bins illustrated by the dotted vertical lines in Fig. 4.2. As with the Al target, data were available taken with a still lower threshold trigger, downscaled even further, but most of the events that satisfy that trigger are from collisions too peripheral for us to analyze because the spectrometer contains too many projectile spectator protons.

The N_c bins used are tabulated in Tab. 4.2. For each bin are indicated the N_c boundaries, the centrality as a fraction of the geometric cross section above the middle of the bin, and the total number of events analyzed. A more thorough discussion of N_c distributions is available in Ref. [Bar 92b].

Transverse energy $E_t \equiv \int \sin\theta \, dE = \int \operatorname{sech}\eta \, dE$, as measured in the pseudorapidity ranges $-2 < \eta < -0.9$ and $-0.5 < \eta < 0.8$ by the TCal, is also often a good measure of centrality, but it was not used in this analysis because

N_c	$\sigma/\sigma_{\rm geo}$	$N_{\rm ev}$
100–120	16.2%	28229
120–140	8.6%	92313
140–160	2.8%	122381
160–180	0.52%	70173
180–200	0.07%	9941

Table 4.2: Multiplicities and centralities in Si + Pb.

it is well correlated with the charged particle multiplicity.

The incident beam trajectory is measured by the BVer detectors. There are 384 vertical 50 μm strips in each detector. In the first, 11 were "hot"—*i. e.,* they often fired even when no beam particle passed through them. There was only one "hot" strip in the second detector. Suppression of the "hot" strips leads to about a 3% inefficiency of this detector system. This inefficiency slightly reduces statistics but otherwise affects none of the following results.

4.2 Momentum Measurement

4.2.1 Track reconstruction

The hits in the various detectors downstream of the magnet are reconstructed into tracks by an E814 pattern recognition program that runs as part of the STEP1 package described in Sec. 3.2. This program is called "Quanah" and is based on the tree-climbing algorithm of Cassel and Kowalski [Cas 81]. Quanah is also discussed in some detail in Refs. [Bar 92a, Bar 94b].

Hits in the drift section of a chamber are reconstructed into partial tracks called *elements,* comprising hits in at least three of the six wire planes in a chamber. Each element is projected to the pad plane of the chamber to look for pad hits called *clusters.* A cluster is formed under a given wire by looking for the pad with the most charge on it and computing the charge-weighted centroid $y_{\rm cent}$ of the y positions of that pad and its neighbors. This centroid $y_{\rm cent}$ still needs to be corrected for some nonlinearity in the charge

Figure 4.3: Image charge configuration for a charge q a distance a from a single ground plane.

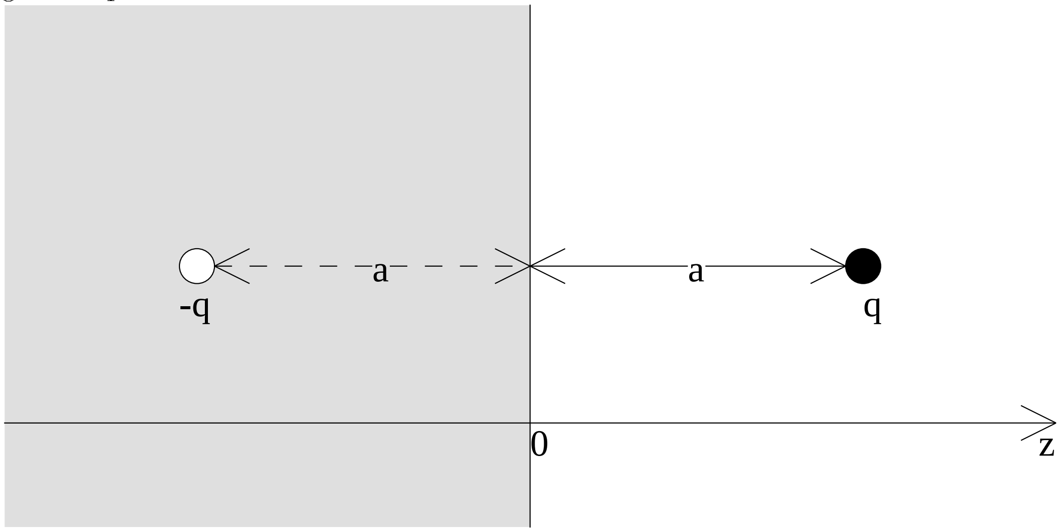

sharing between pads; $y_{\rm cent}$ is mapped to an actual position via a calculation I performed involving the induced charge on the pad plane from a point charge on the associated wire. The induced charge is used to compute $y_{\rm cent}$ as a function of the actual y position. This map then allows determination of the actual y position of the charge on the wire from the measurement of $y_{\rm cent}$.

The calculation was originally done modeling the induced charge distribution on the pad plane as that induced by a point charge near a large conducting plane, as illustrated in Fig. 4.3. We use the standard method of images[1] to reproduce the boundary condition of zero electrostatic potential everywhere on the plane by introducing a fictitious second "image" charge on the other side of the plane, as illustrated in Fig. 4.3, where a is the wire-cathode-plane

[1]See, *e. g.,* Ch. 2 of Jackson [Jac 75].

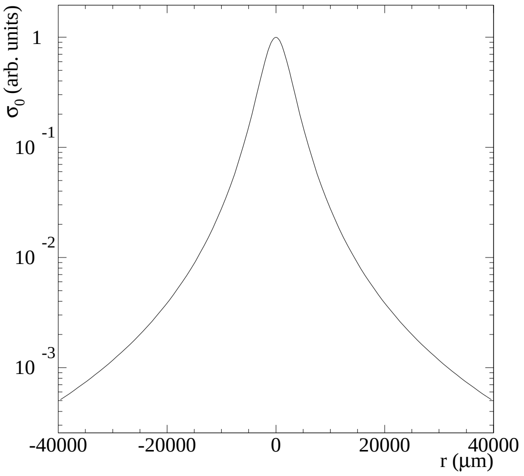

Figure 4.4: Surface charge distribution induced on a conducting plane by a point charge 3175 μm away.

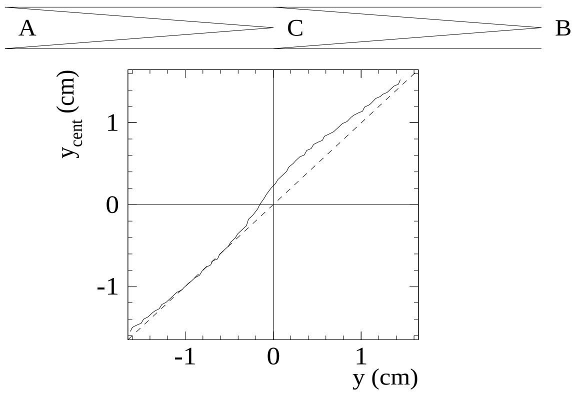

Figure 4.5: Position calculated from the charge centroid of three pads *vs.* actual position in the high-density region of DC2. The actual geometry of three such pads, labeled A, B and C, is shown above the plot on the same scale.

Figure 4.6: Position calculated from the charge centroid of three pads *vs.* actual position in the low-density region of DC3. The actual geometry of three such pads, labeled A, B and C, is shown above the plot on the same scale.

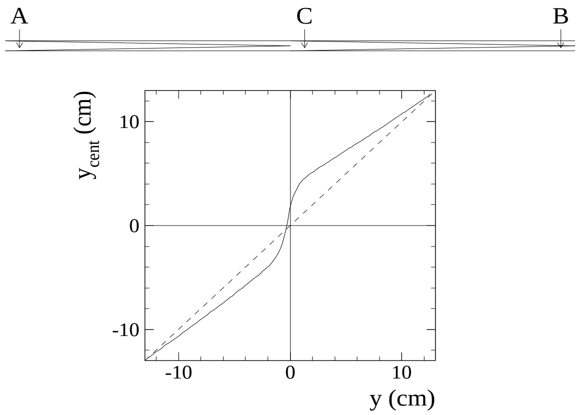

distance. The electrostatic potential φ_0 thus produced is

$$\varphi_0 = \frac{q}{\sqrt{r^2 + (z-a)^2}} - \frac{q}{\sqrt{r^2 + (z+a)^2}}, \tag{4.1}$$

where r is the distance to the axis between the two point charges. We can determine the surface charge distribution σ_0 on the plane by taking the derivative:

$$\sigma_0 = -\frac{1}{4\pi}\frac{\partial \varphi_0}{\partial z}(z=0) \tag{4.2}$$

$$= -\frac{q}{2\pi a^2}\left(1 + \frac{r^2}{a^2}\right)^{-\frac{3}{2}}. \tag{4.3}$$

This function is plotted in Fig. 4.4 for $a = 3175$ μm, the wire-cathode-plane distance in DC2, and arbitrary q. This is the charge distribution used in the computation of y_{cent} as a function of y in DC2. The results are shown for the

Figure 4.7: Image charge configuration for a charge q between two ground planes separated by a distance d. The charge is a distance a from one plane.

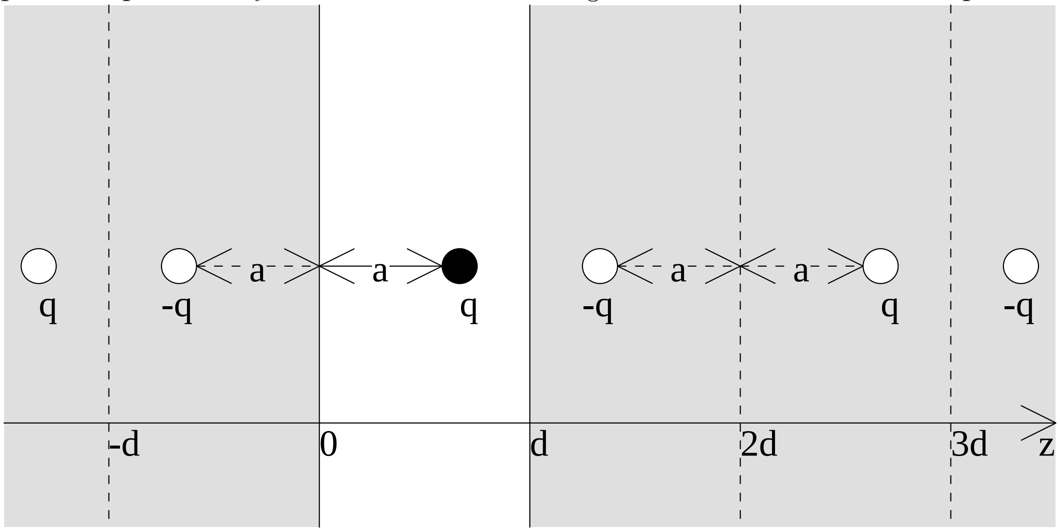

high-density region in Fig. 4.5. A similar computation is done for DC3. The results are shown for the low-density region in Fig. 4.6.

In each drift chamber, however, there is a second ground plane parallel to the cathode pad plane on the other side of the anode wire, so the charge distribution is better modeled as that induced by a point charge between two large, parallel conducting planes. It is possible to express the potential for this configuration in terms of Bessel functions—*e. g,* as a Fourier decomposition of the potential using Bessel functions as the base functions.[2] For computational purposes, however, it is easier to use the method of images again. In this case, there are infinitely many "image" charges, as illustrated in Fig. 4.7. The

---

[2]See, *e. g.,* problem 3.17 in Jackson [Jac 75] and references therein.

electrostatic potential φ induced is

$$\begin{aligned}
\varphi &= \frac{q}{\sqrt{r^2+(z-a)^2}} - \frac{q}{\sqrt{r^2+(z+a)^2}} \\
&+ \sum_{j=1}^{\infty}\left[\frac{q}{\sqrt{r^2+(z-2jd-a)^2}} - \frac{q}{\sqrt{r^2+(z-2jd+a)^2}}\right] \\
&+ \sum_{j=1}^{\infty}\left[\frac{q}{\sqrt{r^2+(z+2jd-a)^2}} - \frac{q}{\sqrt{r^2+(z+2jd+a)^2}}\right] \qquad (4.4)
\end{aligned}$$

or

$$\begin{aligned}
\varphi &= \varphi_0 \\
&+ \sum_{j=1}^{\infty}\left[\frac{q}{\sqrt{r^2+(z-2jd-a)^2}} - \frac{q}{\sqrt{r^2+(z-2jd+a)^2}}\right] \\
&+ \sum_{j=1}^{\infty}\left[\frac{q}{\sqrt{r^2+(z+2jd-a)^2}} - \frac{q}{\sqrt{r^2+(z+2jd+a)^2}}\right] \qquad (4.5)
\end{aligned}$$

where φ_0 is the potential from the single ground plane case in Eq. 4.1 above.

As in Eq. 4.2, we can write

$$\begin{aligned}
\sigma &= -\frac{1}{4\pi}\frac{\partial\varphi}{\partial z}(z=0) \qquad (4.6) \\
&= \sigma_0 - \frac{q}{2\pi d^2}\left[f(\rho;\alpha) - f(\rho;-\alpha)\right] \qquad (4.7)
\end{aligned}$$

where $\rho \equiv r/d$, $\alpha \equiv a/d$, σ_0 is defined in Eqs. 4.2 and 4.3 above, and

$$f(\rho;\alpha) \equiv \sum_{j=1}^{\infty}\frac{2j+\alpha}{(\rho^2+(2j+\alpha)^2)^{\frac{3}{2}}}. \qquad (4.8)$$

This sum cannot be easily expressed in terms of elementary functions. For computational purposes, we use the first ten terms of the series, which converges like $\sum_j 1/j^2$. The results of taking the first 3, 6 and 10 terms of this series are plotted in Fig. 4.8 for $a = 3175$ μm and $d = 9525$ μm, as in DC2.

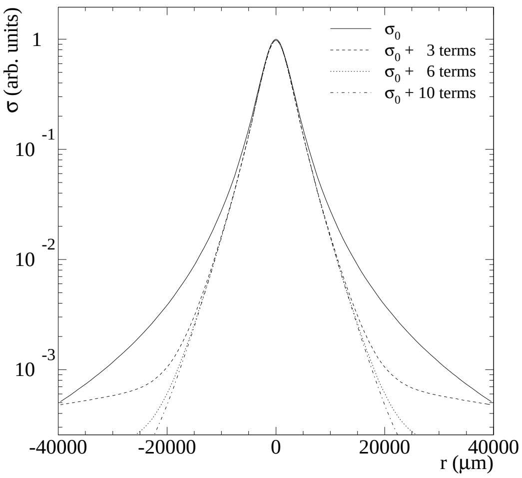

Figure 4.8: Surface charge distribution induced on a conducting plane by a point charge 3175 μm away with another grounded conducting plane 6350 μm beyond that. The solid curve is σ_0 from Eq. 4.3. The other curves indicate the modification to this distribution by taking 3, 6 and 10 terms from the series in Eq. 4.8.

Each successive term makes the distribution narrower near the peak, while flattening out the tails at large distances. For large r, the charge density falls off [3] like $r^{-\frac{1}{2}}\exp(-\pi r/d)$.

In the end, the charge centroid positions y_{cent} computed from this charge distribution do not differ visibly from those plotted in Figs. 4.5 and 4.6.

If a cluster is found on the pad plane matching the projected position of an element, the associated vertical position information is used. If no cluster is found, an inefficiency is avoided by using the element alone with no vertical position information. This is necessary because in the region where the beam traverses the chamber, the residual signal from the heavy ion in the pads it crosses prevents the ADC from giving useful information for minimum-ionizing particles that cross them close in time to a previous beam particle.

Hits from each chamber are combined with hits in the scintillators to form *segments.* The algorithm requires that the segments be straight within the detector resolutions, and based on the apparatus geometry, we place a loose cut on the angles they make with the beam axis. Position information in both dimensions is available from the scintillators, though with limited resolution. The horizontal position is specified by the hodoscope granularity to within ± 5 cm, and the vertical position is obtained either from the time or amplitude signals from the phototubes at each end of the scintillator slats. The resolution in this coordinate is 3–4 cm, comparable to the resolution in the horizontal coordinate.

---

[3] See, *e. g.,* problem 3.17 in Jackson [Jac 75].

Figure 4.9: Bend-plane geometry of a track passing through a region of uniform magnetic field.

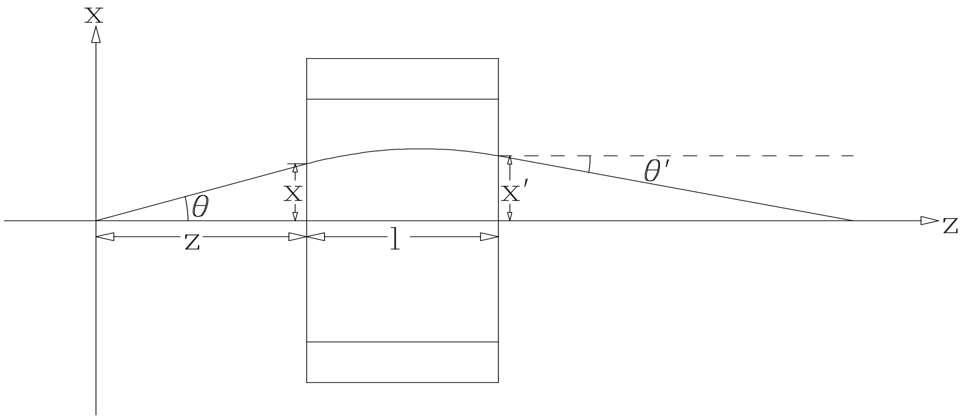

Segments that point back into the magnet aperture are assigned vector momenta, becoming *candidates.* Since the apparatus in this configuration has no tracking between the target and the magnet, determination of the momenta requires assuming that the candidates originated where the beam struck the target. Each component of the magnetic field has been measured as a function of position inside and near the magnet. We have determined that the effect of the fringe field can be accurately accounted for by using an effective length somewhat greater than the length of the magnet itself. This allows us to model the apparatus as a region of uniform magnetic field with only a y component surrounded by a region of zero field.

With these assumptions, we can make the following statements (see Fig. 4.9):

$$R(\sin\theta' - \sin\theta) \quad = \quad -\ell \tag{4.9}$$

$$x = z\tan\theta \tag{4.10}$$

$$x' - x = R(\cos\theta' - \cos\theta) \tag{4.11}$$

where R is the radius of the circular projection onto the bend plane of the helical trajectory of the track through the region of magnetic field, with the convention that $R > 0$ if a particle is deflected in the $-x$ direction, as shown in Fig. 4.9. Note that x and x' are measured relative to the vertex x position, as determined by the BVERs. The angle the particle's trajectory makes in the bend plane with the z axis before the magnet is θ, and that after the magnet is θ'. The effective length of the magnetic field region is denoted by ℓ. The radius of curvature R is related to the magnetic rigidity p_{zx}/Z by

$$R = \frac{p_{zx}}{ZeB} \tag{4.12}$$

where $p_{zx} \equiv \sqrt{p_x^2 + p_z^2}$ is the momentum component in the bend plane, e is the proton charge, Z is the particle's charge number, and B is the magnitude of the magnetic field. The exact value of B is verified by comparing the known beam momentum and the measured momentum of beam-rapidity protons.

Combining Eqs. (4.9) and (4.11), we eliminate R:

$$\frac{\sin\theta - \sin\theta'}{\ell} = \frac{\cos\theta' - \cos\theta}{x' - x}. \tag{4.13}$$

Equation (4.10), along with some trigonometry, allows us to eliminate θ, so we have

$$\frac{x - \sin\theta'\sqrt{x^2 + z^2}}{\ell} = \frac{\cos\theta'\sqrt{x^2 + z^2} - z}{x' - x}. \tag{4.14}$$

Moving the radicals to one side and squaring gives a fourth order polynomial in x, the algebraic solution of which is straightforward, if tedious. The closed form of the solution is too cumbersome to be useful, but an algorithm exists for computing the roots of an arbitrary quartic equation.[4] The position x at the entrance to the magnet determines θ and R, and hence p_{zx}/Z, via Eqs. (4.9) through (4.12). In practice, an iterative numerical procedure is used to find these quantities.

In an ideal dipole magnet, the component p_y of momentum parallel to the magnetic field is conserved, as is p_{zx}, the magnitude of the component normal to the field. Hence, the out-of-plane angle $\varphi \equiv \arctan(p_y/p_{zx})$ is conserved, so the vertical component of momentum may be reconstructed by using the vertical position information from the detectors to measure φ and multiplying p_{zx}, obtained from the previous procedure, by $\tan\varphi$. Using the charge magnitude measured via the energy loss in the scintillators, we determine the momentum of each candidate.

After having associated vector momenta with each candidate, we must take into account that candidates may occasionally share hits in the various detectors. A final algorithm selects the largest subset of the candidates that share no hits. These candidates are finally the reconstructed *tracks* produced by Quanah.

4.2.2 Momentum resolution

I use a somewhat simpler model of the magnetic deflection to compute the momentum resolution. We assume that all angles are small, and further

[4]See, *e. g.,* Birkhoff and Mac Lane [Bir 53], p. 114 ff.

that particle trajectories are straight line segments with a single bend at the center of the magnet. We call this the "single bend" model, and we refer to the plane that bisects the magnetic field region normal to the z-axis as the "bend center" of the magnet. We will retain the notation of Sec. 4.2.1, but we will make a few new definitions: the position of the bend center is $z_{\mathrm{bc}} \equiv z + \ell/2$ and the x coordinate of the intersection of the trajectory with the bend center is $x_{\mathrm{bc}} \equiv x' - \theta'\ell/2$. Also, we will refer to the transverse momentum or p_t "kick" Δp_t given by the magnet. This is proportional to the field integral $\int B \cdot dl$ of the magnet. The constant of proportionality, in appropriate units, is the speed of light c (see App. D). With these definitions and the assumption of small angles, we can write

$$\theta = \frac{x_{\mathrm{bc}}}{z_{\mathrm{bc}}} \tag{4.15}$$

and

$$\delta\theta = \frac{\delta x_{\mathrm{bc}}}{z_{\mathrm{bc}}}. \tag{4.16}$$

The p_t kick is just the change in p_x imparted by the magnet to a particle carrying unit charge and is constant. Hence,

$$\frac{p_{zx}}{Z} = \frac{\Delta p_t}{\theta' - \theta}. \tag{4.17}$$

In addition, $p_x = \theta p_{zx}$, so

$$\frac{p_x}{Z} = \frac{\theta}{\theta' - \theta}\Delta p_t. \tag{4.18}$$

Taking derivatives of Eqs. (4.17) and (4.18), we find

$$\left\langle \frac{\delta p_{zx}^2}{p_{zx}^2} \right\rangle = \left(\frac{p_{zx}}{Z\Delta p_t} \right)^2 \left\langle \delta\theta'^2 - 2\delta\theta\delta\theta' + \delta\theta^2 \right\rangle, \tag{4.19}$$

$$\left\langle \frac{\delta p_x^2}{p_{zx}^2} \right\rangle = \left(\frac{p_{zx}}{Z\Delta p_t} \right)^2 \left\langle \theta'^2\delta\theta^2 - 2\theta\theta'\delta\theta\delta\theta' + \theta^2\delta\theta'^2 \right\rangle, \tag{4.20}$$

where the angle brackets denote a statistical average.

The angles θ and θ' are determined by linear regression from N independent position measurements from the two drift chambers, each with resolution σ. We use standard error analysis[5] to find

$$\left\langle \delta\theta'^2 \right\rangle = \frac{\sigma^2}{N\Delta z^2}, \tag{4.21}$$

$$\langle \delta\theta\delta\theta' \rangle = -\frac{\overline{z - z_{\mathrm{bc}}}}{z_{\mathrm{bc}}}\frac{\sigma^2}{N\Delta z^2}, \tag{4.22}$$

$$\left\langle \delta\theta^2 \right\rangle = \frac{\overline{(z - z_{\mathrm{bc}})^2}}{z_{\mathrm{bc}}^2}\frac{\sigma^2}{N\Delta z^2}, \tag{4.23}$$

where

$$\Delta z^2 \equiv \overline{(z - \bar{z})^2} \tag{4.24}$$

$$= \overline{z^2} - \bar{z}^2 \tag{4.25}$$

and the bars denote averaging over the N measurements.

Plugging Eqs. (4.21)–(4.25) into (4.19) and (4.20), we finally obtain

$$\frac{\delta p_{zx}^2}{p_{zx}^2} = \left(\frac{p_{zx}}{Z\Delta p_t}\right)^2 \frac{\sigma^2\zeta^2}{N\Delta z^2 z_{\mathrm{bc}}^2}, \tag{4.26}$$

$$\delta p_x^2 = \frac{\delta p_{zx}^2}{p_{zx}^2}\left[(p_x - p_0)^2 + p_1^2\right], \tag{4.27}$$

where

$$\zeta^2 \equiv \bar{z}^2 + \Delta z^2, \tag{4.28}$$

$$p_0 \equiv -\Delta p_t \frac{\zeta^2 - 2z_{\mathrm{bc}}\bar{z}}{\zeta^2}, \tag{4.29}$$

$$p_1 \equiv \Delta p_t \frac{z_{\mathrm{bc}}\Delta z}{\zeta^2} \tag{4.30}$$

[5]See, *e. g.*, Ch. 6 of Bevington [Bev 92].

and we have suppressed the angle brackets indicating the statistical average.

We now consider the vertical component p_y of the momentum. Again, all angles within the acceptance of our spectrometer are sufficiently small that for this purpose we can define

$$\varphi \equiv \frac{y_{\mathrm{TC}}}{z_{\mathrm{TC}}} \tag{4.31}$$

and

$$p_y = \varphi p_z = \varphi p_{zx} \tag{4.32}$$

to order θ, where y_{TC} and z_{TC} are the y and z coordinates, respectively, of the measurement at the tracking chamber. Hence we have

$$p_y = \frac{y_{\mathrm{TC}}}{z_{\mathrm{TC}}} p_{zx}. \tag{4.33}$$

Because θ and φ are small, we also have

$$p = p_{zx} \tag{4.34}$$

ignoring terms of quadratic and higher order in θ and φ, where p is the total magnitude of the momentum vector. Hence

$$\frac{\delta p}{p} = \frac{\delta p_{zx}}{p_{zx}}. \tag{4.35}$$

From Eqs. (4.32) and (4.34) we see

$$\delta p_y^2 = \delta\varphi^2 p^2 + \varphi^2 \delta p^2, \tag{4.36}$$

$$= \delta\varphi^2 p^2 + p_y^2 \left(\frac{\delta p}{p}\right)^2. \tag{4.37}$$

We have seen from Eq. (4.19) that $\delta p/p = \alpha p$, where α is constant, so we can write

$$\delta p_y^2 = \left(\delta\varphi^2 + \alpha^2 p_y^2\right) p^2. \tag{4.38}$$

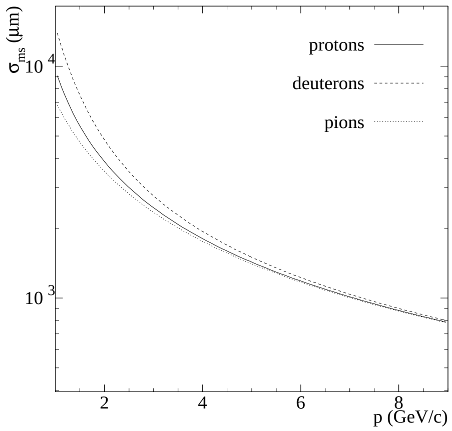

Figure 4.10: Position resolutions at DC2 due to multiple scattering in air.

For the value of the magnetic field used, the field integral $\int B \cdot dl$ is 0.273 T·m, corresponding to a p_t kick Δp_t of 81.8 MeV/c (see App. D), and the momentum resolution corresponding to the 300 μm position resolution of each drift plane of the chambers is $\delta p/p \approx (0.1\%/\mathrm{GeV})\, pc/|Z|$.

The momentum resolution over our momentum range is dominated by multiple scattering in the apparatus, mostly in the 7 m of air between the target and DC2. Multiple scattering effectively increases the uncertainty σ of the position resolution at each chamber. The momentum-dependent contribution from multiple scattering to the resolution at a distance z from the target is

$$\sigma_{\mathrm{ms}}(p, z) = \frac{1}{\sqrt{3}} z \theta_0(p, z) \tag{4.39}$$

where

$$\theta_0(p, z) \equiv \left(\frac{13.6\, Z\ \mathrm{MeV}}{\beta c p}\right) \sqrt{\frac{z}{X_0}} \left(1 + 0.038 \ln \frac{z}{X_0}\right) \tag{4.40}$$

Table 4.3: Multiple scattering coefficients K_{ms} in μm·GeV for the different targets and the two drift chambers.

	2% Al	1% Pb	2% Pb
DC2	7019	7023	7028
DC3	15254	15261	15267

is the rms scattering angle and X_0 is the radiation length of the material.[6] Equations (4.39) and (4.40) only hold for scattering through a single homogeneous medium. In our case, the medium is inhomogeneous, or at best piecewise homogeneous, so we use the expression for Δx in Eq. (E.12) from App. E to obtain $\sigma_{\mathrm{ms}}(p, z)$. In general,

$$\sigma_{\mathrm{ms}}(p, z) = K_{\mathrm{ms}}(z) \frac{Z}{\beta p}. \tag{4.41}$$

The coefficient K_{ms} is listed in Tab. 4.3 for each different combination of target and drift chamber, using the information in Tab. 2.1. The function $\sigma_{\mathrm{ms}}(p)$ is plotted in Fig. 4.10 for DC2 neglecting the target contribution, which is small.

We must account in our calculations for the fact that $\sigma_{\mathrm{ms}}(p, z)$ is different at each tracking chamber due to the different distances through which particles

[6]See, *e. g.*, the "Review of Particle Properties" [Rev 94], p. 1253 ff., and references therein.

scatter. At each chamber, the effective resolution $\sigma_{\text{eff}}(p, z)$ is

$$\sigma^2_{\text{eff}}(p, z) \equiv \sigma^2 + \sigma^2_{\text{ms}}(p, z). \tag{4.42}$$

Over most of our momentum range σ_{ms} is considerably larger than σ, so we generally just let $\sigma_{\text{eff}}(p, z) = \sigma_{\text{ms}}(p, z)$. Because the effective resolution of each chamber is now different, we cannot use Eqs. (4.21)–(4.23) directly, but standard methods allow us to do a similar computation with arbitrary errors.

Because each drift chamber is quite thin compared with the distance between them, each of the wire measurements within a chamber takes place essentially at the same z coordinate. Effectively each chamber provides a single measurement. Precisely, let the positions of DC2 and DC3, respectively, be z_2 and z_3. The momentum-dependent multiple-scattering dominated position resolutions at the two chambers are σ_2 and σ_3, and the chambers make N_2 and N_3 measurements, respectively. The measurements themselves are denoted by x_2 and x_3, which have resolutions $\sigma_2/\sqrt{N_2}$ and $\sigma_3/\sqrt{N_3}$. So we find that

$$\theta' = \frac{x_3 - x_2}{z_3 - z_2}, \tag{4.43}$$

and

$$x_{\text{bc}} = x_2 - \theta'(z_2 - z_{\text{bc}}), \tag{4.44}$$

which can be written

$$x_{\text{bc}} = \frac{x_2(z_3 - z_{\text{bc}}) - x_3(z_2 - z_{\text{bc}})}{z_3 - z_2}. \tag{4.45}$$

So we find

$$\left\langle \delta\theta'^2 \right\rangle \;=\; \frac{1}{(z_3 - z_2)^2}\left(\frac{\sigma_2^2}{N_2} + \frac{\sigma_3^2}{N_3}\right), \tag{4.46}$$

$$\langle \delta\theta\delta\theta' \rangle = -\frac{1}{(z_3 - z_2)^2}\left[\frac{\sigma_2^2}{N_2}\frac{z_3 - z_{\rm bc}}{z_{\rm bc}} + \frac{\sigma_3^2}{N_3}\frac{z_2 - z_{\rm bc}}{z_{\rm bc}}\right], \tag{4.47}$$

$$\left\langle \delta\theta^2 \right\rangle = \frac{1}{(z_3 - z_2)^2}\left[\frac{\sigma_2^2}{N_2}\left(\frac{z_3 - z_{\rm bc}}{z_{\rm bc}}\right)^2 + \frac{\sigma_3^2}{N_3}\left(\frac{z_2 - z_{\rm bc}}{z_{\rm bc}}\right)^2\right], \tag{4.48}$$

which we substitute in Eqs. (4.19) and (4.20) to obtain the momentum resolutions.

We find

$$\left(\frac{\delta p}{p}\right)^2 = \left(\frac{p}{Z\Delta p_t}\right)^2 \frac{z_2^2 z_3^2}{z_{\rm bc}^2(z_3 - z_2)^2}\left(\frac{\sigma_2^2}{N_2 z_2^2} + \frac{\sigma_3^2}{N_3 z_3^2}\right), \tag{4.49}$$

or, introducing K_2 and K_3 for the coefficients $K_{\rm ms}$ at each drift chamber and letting $N_2 = N_3 = N' = 5.4$ (see the discussion of wire efficiencies in Sec. 4.5 below) we have

$$\left(\frac{\delta p}{p}\right)^2 = \left(\frac{1}{\beta\Delta p_t}\right)^2 \frac{z_2^2 z_3^2}{N' z_{\rm bc}^2(z_3 - z_2)^2}\left(\frac{K_2^2}{z_2^2} + \frac{K_3^2}{z_3^2}\right). \tag{4.50}$$

We finally compute the momentum resolution due to multiple scattering in all the materials in the spectrometer, using the values of $K_{\rm ms}$ in Tab. 4.3. We find $\delta p/p \approx 4.8\%/\beta$, where β is the particle's velocity relative to the speed of light. This number is approximately independent of target, as can be seen from the small variation from target to target of the numbers in Tab. 4.3. This prediction is plotted in Fig. 4.11 along with measured resolutions obtained by determining simultaneously at each momentum the proton and deuteron mass widths, as discussed in Ch. 7. We know

$$\left(\frac{\delta m}{m}\right)^2 = \left(\beta\gamma^2\right)^2\left(\frac{\delta t}{z}\right)^2 + \left(\frac{\delta p}{p}\right)^2, \tag{4.51}$$

and by measuring the mass widths for two different peaks at the same momentum, we can extra δt and $\delta p/p$. The data, unfortunately, were obtained by

Figure 4.11: Momentum resolution *vs.* momentum due to multiple scattering measured in Si + Al collisions. The curves plotted are computed from Eq. 4.50.

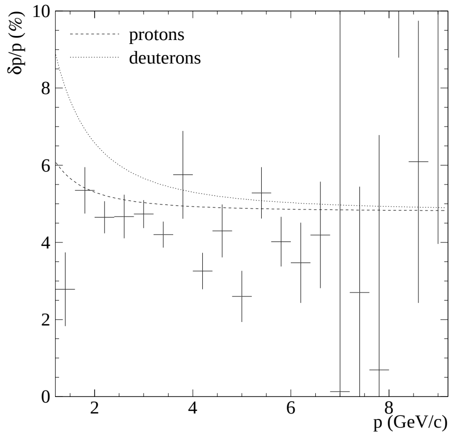

naively assuming that the proton and deuteron would have the same momentum resolution at a given momentum, which is only true for high momenta, so the low-momentum comparison is not very meaningful.

4.3 Particle Identification

Reconstruction of the tracks also allows measurement of the lengths of the total flight paths of the particles, which together with the time-of-flight determined by the scintillators, yields the velocity β of each particle. The time-of-flight indicated by each photomultiplier tube is corrected for "slewing," the dependence on pulse height of the time indicated by the TDC. After the slewing correction is applied, we determine the mean time of the top and bottom tubes. To find the time offset t_0 for every counter, we employ an

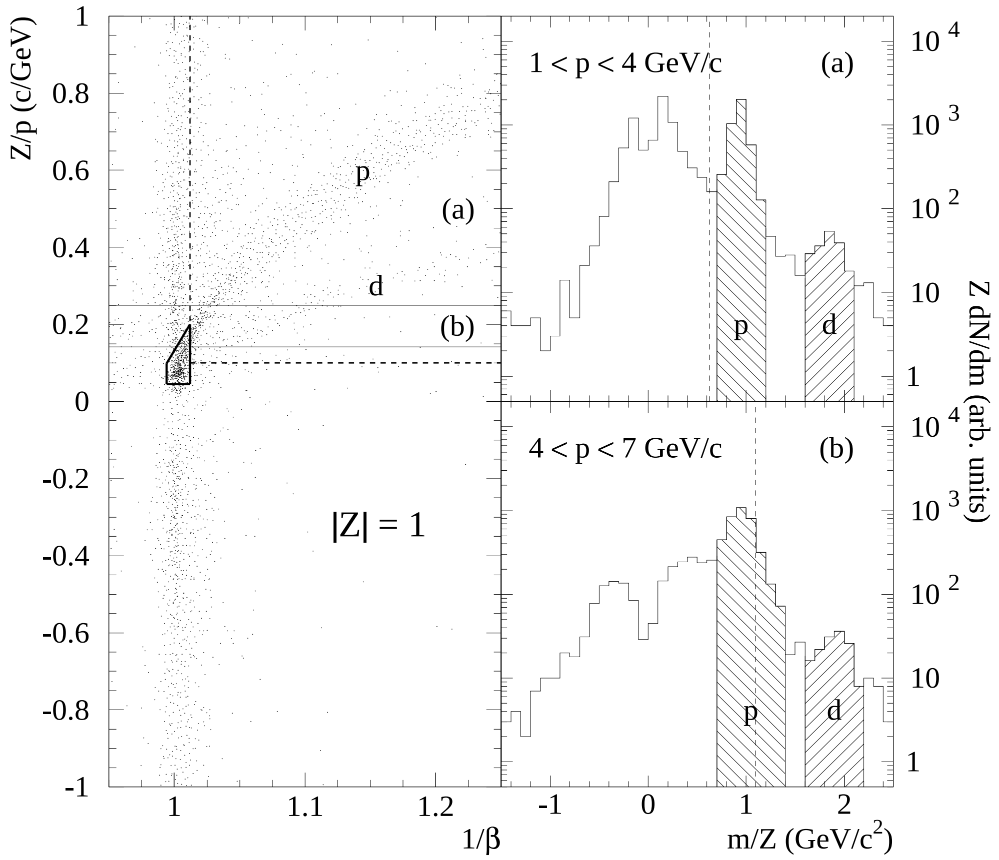

Figure 4.12: Particle identification by measurement of velocity β and rigidity p/Z for $|Z| = 1$. Solid lines in the left-hand panel mark the boundaries between the momentum bins, labeled a and b, on the right-hand side, for $Z = +1$. Above and to the right of the dashed lines in the left panel, particles are identified by mass cuts illustrated by the hatched regions in the two right panels. Tracks that fall in the region containing $\beta = 1$ and $p = 10$ GeV/c indicated by the trapezoid in the left panel are also assumed to be protons (see text). Dashed lines in the right hand panels indicate $\beta = 0.988$, corresponding to the vertical dashed line in the left-hand panel, for the highest momentum in each bin.

iterative procedure, using the measurement of velocity and momentum, and hence the mass, associated with each track. Having identified protons and pions, we use their known masses and well-determined momenta to predict their times-of-flight, hence obtaining t_0.

The measurement of β, together with the momentum measurement, determines the mass of each particle (Fig. 4.12). We identify particles with mass resolution that is good at low momenta and deteriorates gradually with increasing momentum, though still allowing separation of protons from pions up to a momentum of about 7 GeV/c. Protons can only be separated from kaons below 2 or 3 GeV/c, but the kaon rate is very low, and most of the scintillators lie 31 m from the target after which distance most kaons will have decayed, so there is essentially no kaon background in the proton mass peak. Protons and deuterons are identified by a momentum-dependent mass cut for $\beta < 0.988$ and $p < 10$ GeV/c. Outside of this region, protons are identified by a cut in the $1/\beta$-Z/p plane as indicated by the trapezoid in Fig. 4.12.

The dashed vertical lines in Fig. 4.12 are drawn where $\beta = 0.988$ for the highest momentum in each bin. To the right of each of these lines, particles are identified by mass measurement. Because the momentum bins shown are broad (3 GeV/c), the $\beta = 0.988$ line moves considerably between the edges of the bin, so in a region to the left of each dashed line some protons (of higher momenta) are identified by mass cuts. To the left of this region in each momentum bin, proton identification is done entirely by the trapezoidal cut in the left panel of Fig. 4.12.

4.4 Acceptance and Geometric Efficiency

Protons are accepted in the phase space region indicated by the contour lines in the left panel of Fig. 4.13 determined by the distribution of protons measured in the spectrometer. Fluctuations in the contour lines are due to limited statistics. The right edge of the acceptance is a line at $p = 22$ GeV/c, above which beam rapidity deuterons become a significant background. Between 9 and 22 GeV/c, we cannot distinguish protons from deuterons, but as discussed in Ch. 7, the deuteron-proton ratio is low enough that the background introduced by assuming all tracks in the trapezoidal region of Fig. 4.12 are protons is on the percent level. The pion-proton ratio at these momenta is even lower. The left edge is determined by the geometry of the apparatus and the magnitude of the magnetic field. Note that for $y \geq 1.5$ the acceptance includes $p_t = 0$, and we accept low p_t protons even below $y = 1$, allowing precise measurement of the low p_t part of the spectra to very low rapidities. For $y \geq 2.4$ we accept most, if not all, protons, regardless of their transverse momenta, and we have good sensitivity to the shapes of the transverse momentum spectra; conversely, below $y = 2.4$ we lose sensitivity to the shapes and accept a decreasing fraction of the protons with decreasing rapidity.

Deuterons are accepted in the phase space region indicated in the right panel of Fig. 4.13. The right edge of the acceptance is a line at $p = 9$ GeV/c. Above this momentum it is impossible to separate deuterons from protons via time-of-flight measurement. The left edge is again determined by geometry and the magnetic field. Also indicated in Fig. 4.13 is the most probable transverse

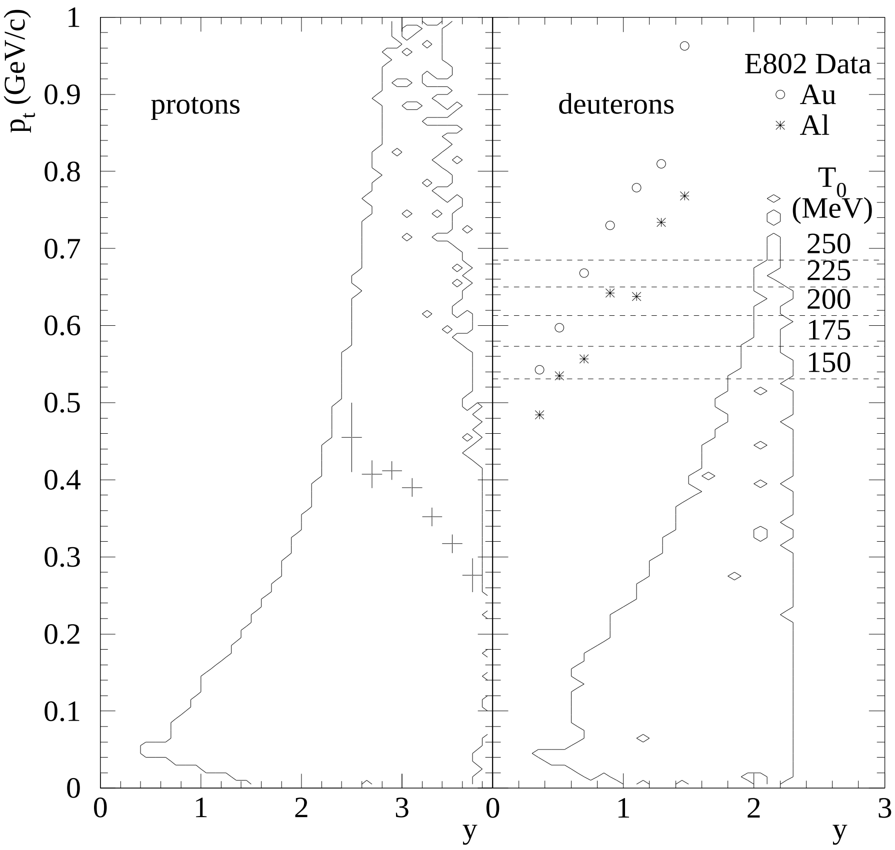

Figure 4.13: Phase space acceptance of the E814 forward spectrometer for protons and deuterons. Solid crosses in the proton plot indicate the most likely transverse momentum as a function of y. For deuterons, the location $\sqrt{m_d T_0}$ of a hypothetical peak for various values of a slope parameter T_0 is given by dashed lines. The peak locations observed by E802 in central collisions are plotted also [Par 92].

momentum for each rapidity bin. For the protons this information is obtained from our measured spectra (see Ch. 5). For deuterons we use the values of T_0 [see Equation (1.5)] measured by E802 [Par 92]; note that because in each case T_0 is much smaller than the deuteron mass, to leading order in T_0/m_d the most probable transverse momentum is given by $\sqrt{m_d T_0}$ (see App. C). The dashed lines are the most probable transverse momenta for deuteron inverse slope parameters from 150 to 250 MeV.

For each rapidity y and transverse momentum p_t we accept a different fraction of the protons and deuterons produced. For example, at and near $p_t = 0$, we accept all protons above rapidity 1.5, since the spectrometer lies on the beam axis; for this case, the geometric efficiency ϵ_{geo} is unity. For larger p_t, ϵ_{geo} decreases and eventually only particles generated with azimuthal angle φ near π ($p_x = -p_t$) will enter the spectrometer. In general, neglecting subtle effects, ϵ_{geo} is equal to the fraction of 2π accepted in azimuth for a given y and p_t. To calculate the geometric efficiency, I used the GEANT detector simulation package [Bru 84], which allows proper implementation of the strength of the magnetic field and the intersection of various detector systems with the collimator opening. This calculation includes effects of beam divergence, multiple scattering, *etc.*

In the acceptance calculation, incident beam trajectories are determined randomly using the distributions measured by the BVERs. Both in the data and in the simulation, angles and hence y and p_t are measured relative to the measured or simulated horizontal beam angle on an event-by-event basis, rather than with respect to the fixed laboratory coordinate frame.

Figure 4.14: Geometric efficiency for protons in the rapidity range $3.2 < y < 3.4$. Errors are due to the statistics of the Monte Carlo.

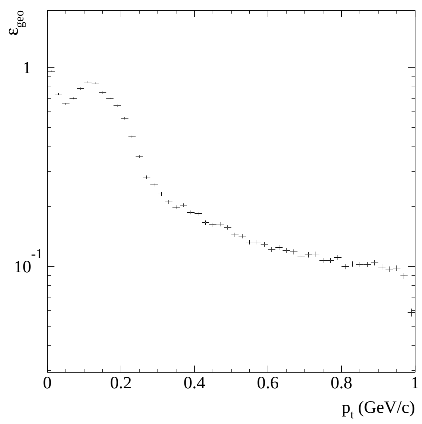

Also, both in the data and in the simulation, a fiducial cut is made inside the collimator acceptance, requiring $\theta_x < 10$ mrad and $|\theta_y| < 16$ mrad, since at the physical boundaries of the collimator opening, $\epsilon_{\rm geo}$ falls to 0 in a way dependent on the *exact* location of the collimator. Although these angles form the boundaries of our acceptance in p_y and positive p_x, they lie well within the acceptance in p_t, since θ_x may go out to -115 mrad. Hence, without this fiducial cut, any uncertainty in the collimator position would translate to large variations in the correction factor $1/\epsilon_{\rm geo}$, which could result in artificial structures in the p_t spectra.

An example of the geometric efficiency $\epsilon_{\rm geo}$ thus obtained is shown in Fig. 4.14 for $3.2 \leq y < 3.4$. The dip near $p_t = 50$ MeV/c is caused by excluding the scintillator slat crossed by the heavy ion beam. The raw data obtained from the spectrometer are divided by $\epsilon_{\rm geo}$ to produce final transverse momentum

Figure 4.15: Distribution of the number n_w of wires per element in DC2. The mean is 5.42 out of 6. The dashed histogram is a binomial distribution with the same mean and total number of elements.

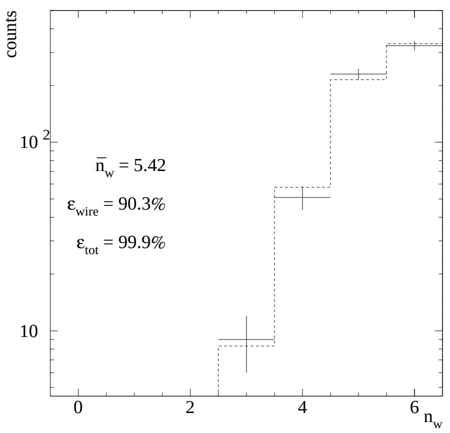

spectra.

4.5 Track Reconstruction Efficiency

In addition to the momentum-dependent geometric efficiency correction, a global (momentum-independent) correction has to be made for the efficiency of the tracking hardware and software. The hardware efficiency of the tracking chambers themselves is essentially 100%. In each chamber the pattern recognition code, Quanah, only requires three of the six wire planes to register the presence of the track. The individual wire efficiency has been measured to be 90% (see Fig. 4.15). Since the number of wires firing is observed to obey a binomial distribution, the overall inefficiency of each chamber requiring three or more wires is about 10^{-3}. The pad planes are not required by Quanah for track reconstruction. If they are present, they are used, but the average track multiplicities in the spectrometer are low enough (about 5 for Si + Al, 1.5 for Si + Pb in typical central collisions) that the information from the drift sections is usually sufficient to reconstruct a track and point unambiguously to a scintillator for time-of-flight information. The pad plane efficiency is around 95%, with the exception of the beam region (see above), so for most tracks the pad information is available. Even when pad information is not available, vertical position information is obtained from the scintillators, albeit with considerably poorer resolution. Vertical information is always present for the tracks considered in this analysis. Timing information will not be present for tracks that strike the same scintillator slat as the beam particle. The geometric inefficiency introduced by ignoring the scintillator beam region is taken into account in the computation described in Sec. 4.4 above. Because the occupancy is low (around 10% in the case of Si + Al; 3% for Si + Pb) we can identify tracks with $|Z| = 1$ by a cut below three times and above half the pulse height of minimum ionizing particles. After this cut, the scintillator efficiency is about 90%. Because of the large distances between the various detectors, the overall efficiency of the reconstruction procedure is found to be 72% $\pm$3% (stat) from visual inspection of about 250 events. We estimate an overall systematic uncertainty of about 10% on the normalization of the differential multiplicities presented later.

Chapter 5

Proton Transverse Momentum Spectra

Figures 5.1 through 5.7 show proton transverse mass spectra in rapidity and centrality bins for the Al and Pb targets. Some of the spectra shown have already been presented elsewhere [Bar 93a, Dee 93, Bar 94b].

As demonstrated in Fig. 5.8 and previously discussed in Refs. [Bar 93a, Dee 93, Bar 94b], the Boltzmann [Eq. (1.4)] spectra fit the data well, but m_t only varies by about 40% over the entire range covered, so there is no visible difference in our acceptance between a Boltzmann spectrum and one in which the invariant multiplicity or cross section is exponential in m_t, as in Eq. (1.5) (although the values of T_B and T_0 differ of course). Cole [Col 93] has reached a similar conclusion for data from E802 for central Si + Au collisions. We favor the Boltzmann parametrization because there the slope has a direct physical interpretation as a temperature and can be compared with other measures of the temperature.

Near beam rapidity ($y_B = 3.44$) and $p_t = 0$, a steep component of the transverse momentum spectrum emerges (see Figs. 5.1 through 5.7), which we

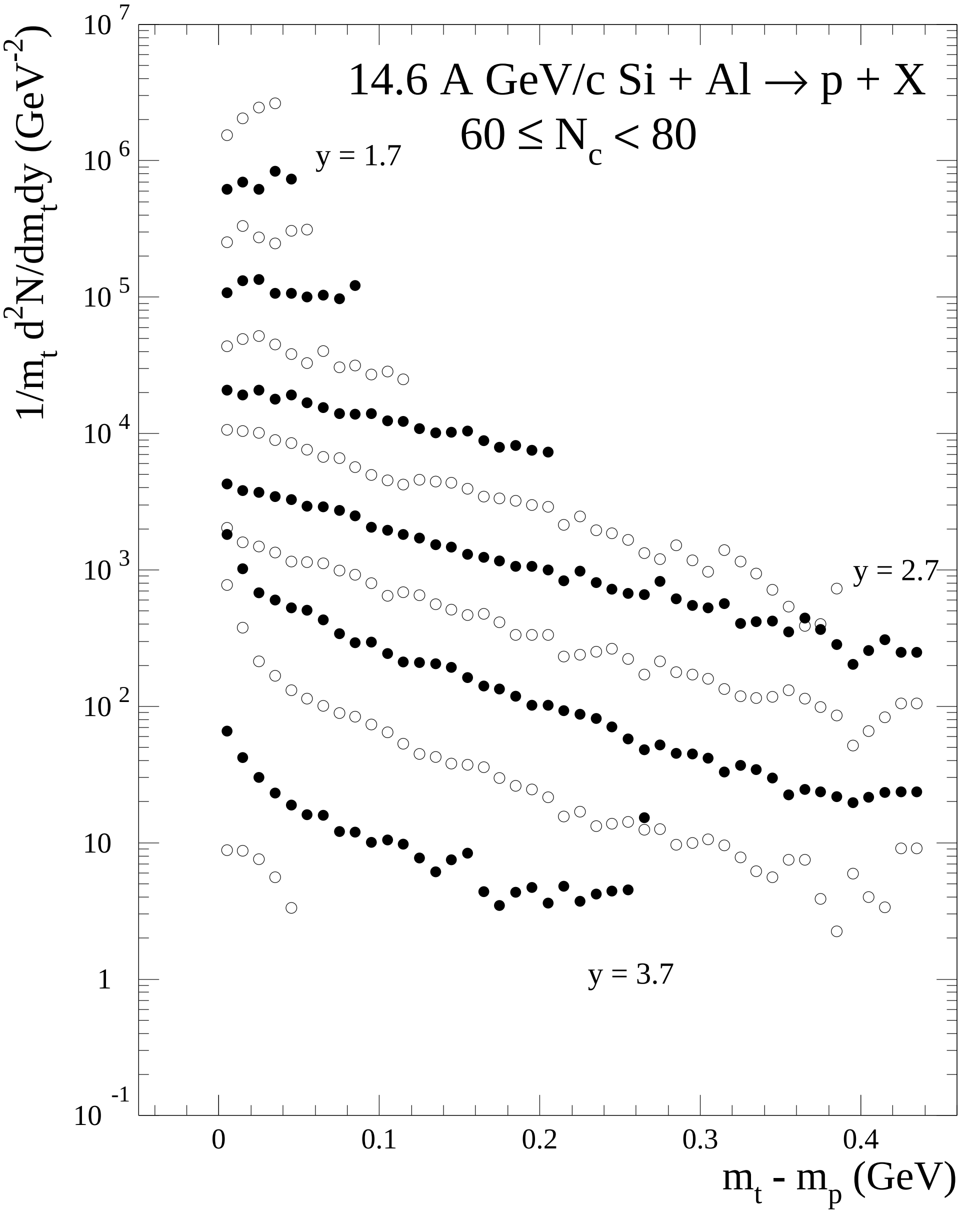

Figure 5.1: Proton invariant multiplicities *vs.* transverse mass for Si + Al in 0.2 unit rapidity bins for $60 \leq N_c < 80$. Starting with the bin at $y = 3.7$, the spectra are multiplied by increasing powers of 2.5 in order to display them simulaneously. Errors are not shown. The point-to-point scatter illustrates the size of statistical errors, though it also indicates some of the spectrometer systematics. See the spectra in Fig. 5.8 for an indication of statistical errors.

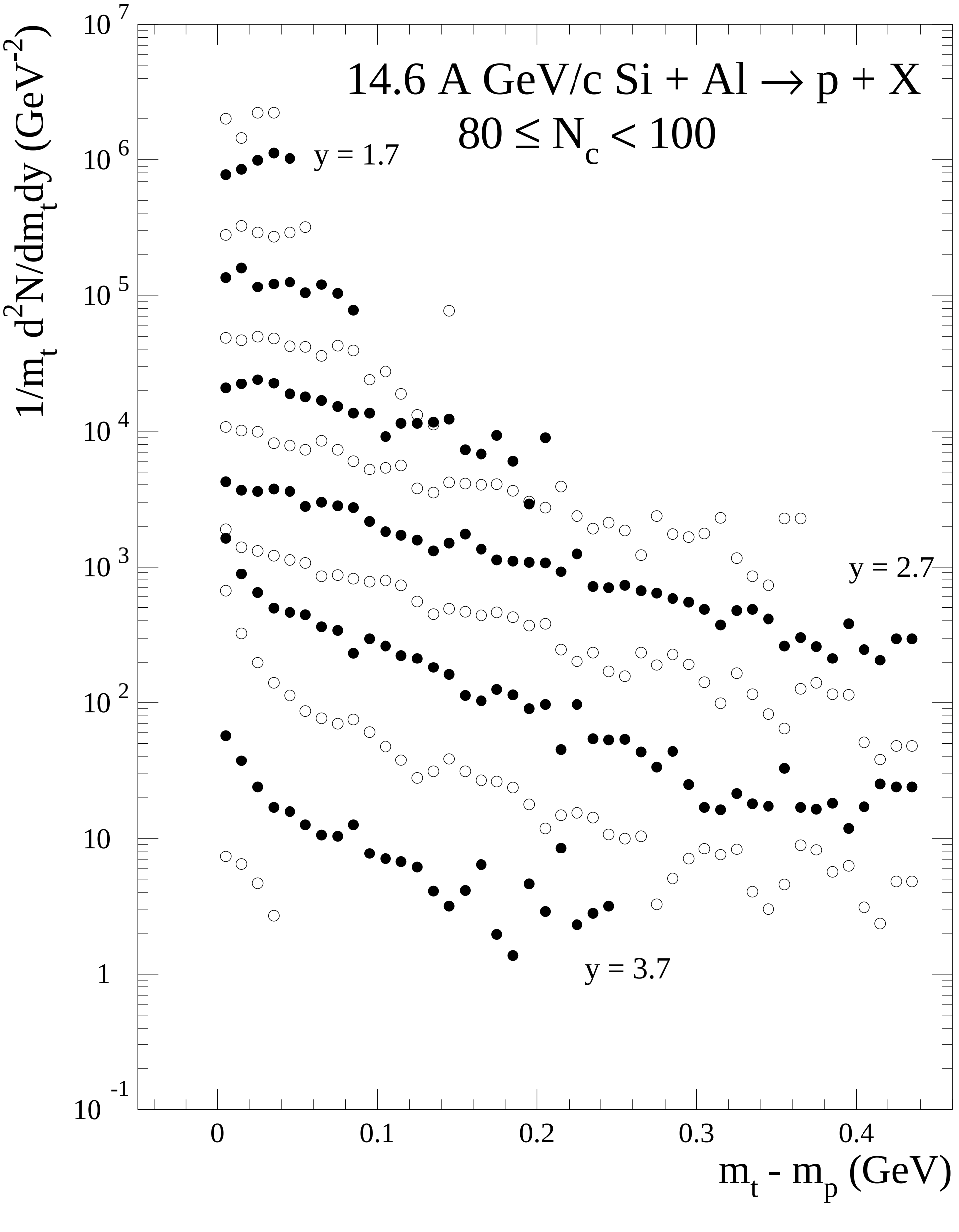

Figure 5.2: Proton invariant multiplicities *vs.* transverse mass for Si + Al in 0.2 unit rapidity bins for $80 \leq N_c < 100$.

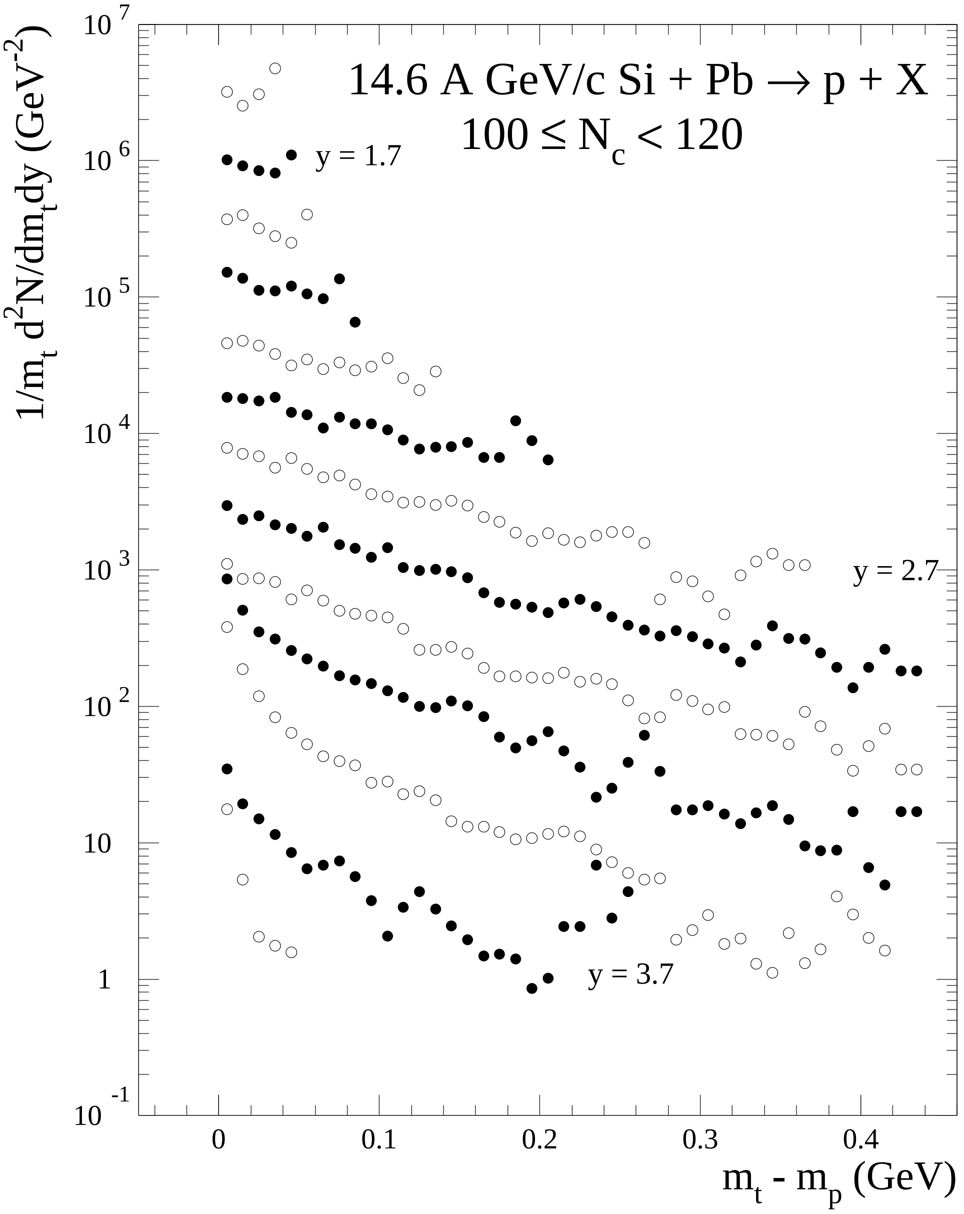

Figure 5.3: Proton invariant multiplicities *vs.* transverse mass for Si + Pb in 0.2 unit rapidity bins for $100 \leq N_c < 120$.

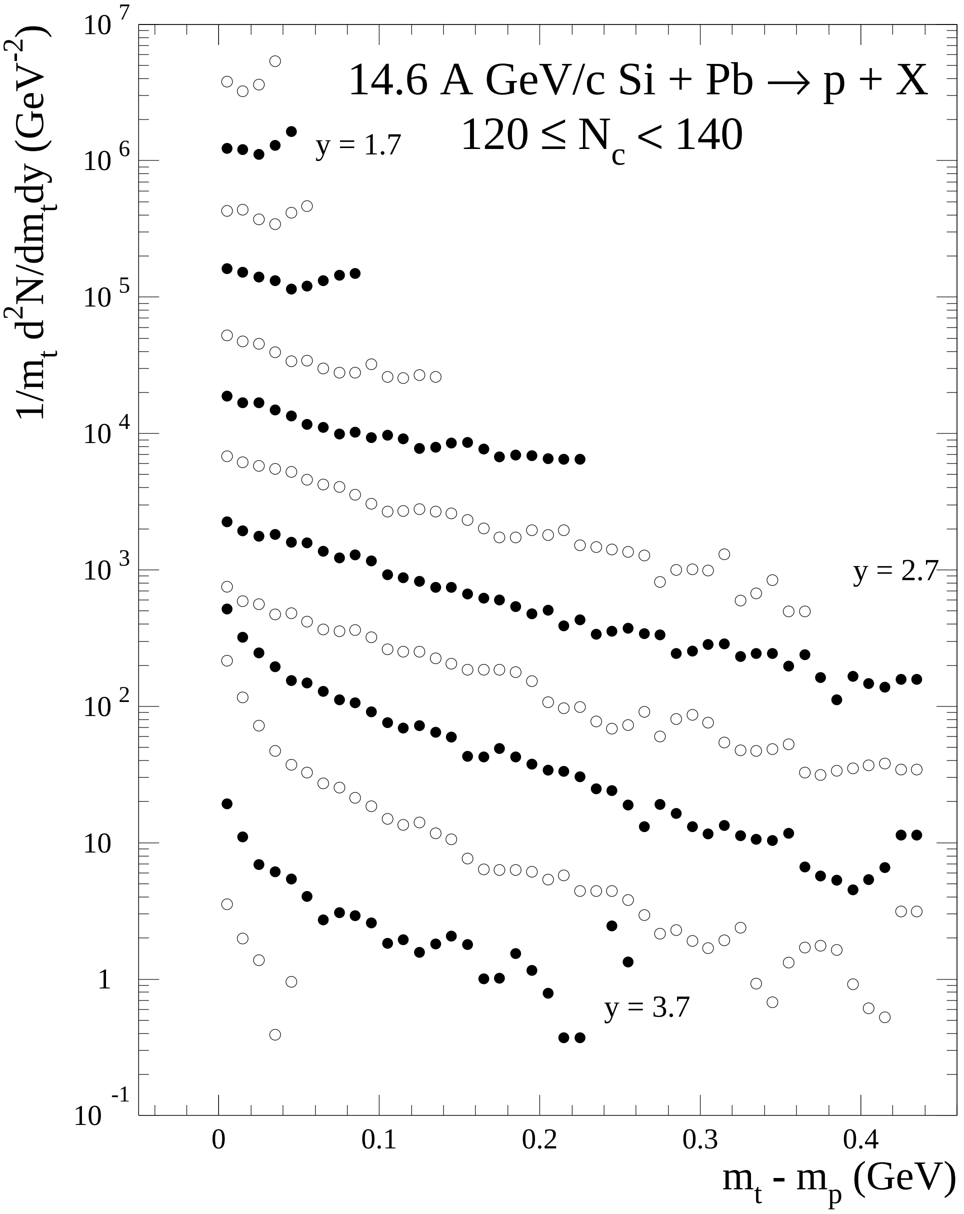

Figure 5.4: Proton invariant multiplicities *vs.* transverse mass for Si + Pb in 0.2 unit rapidity bins for $120 \leq N_c < 140$.

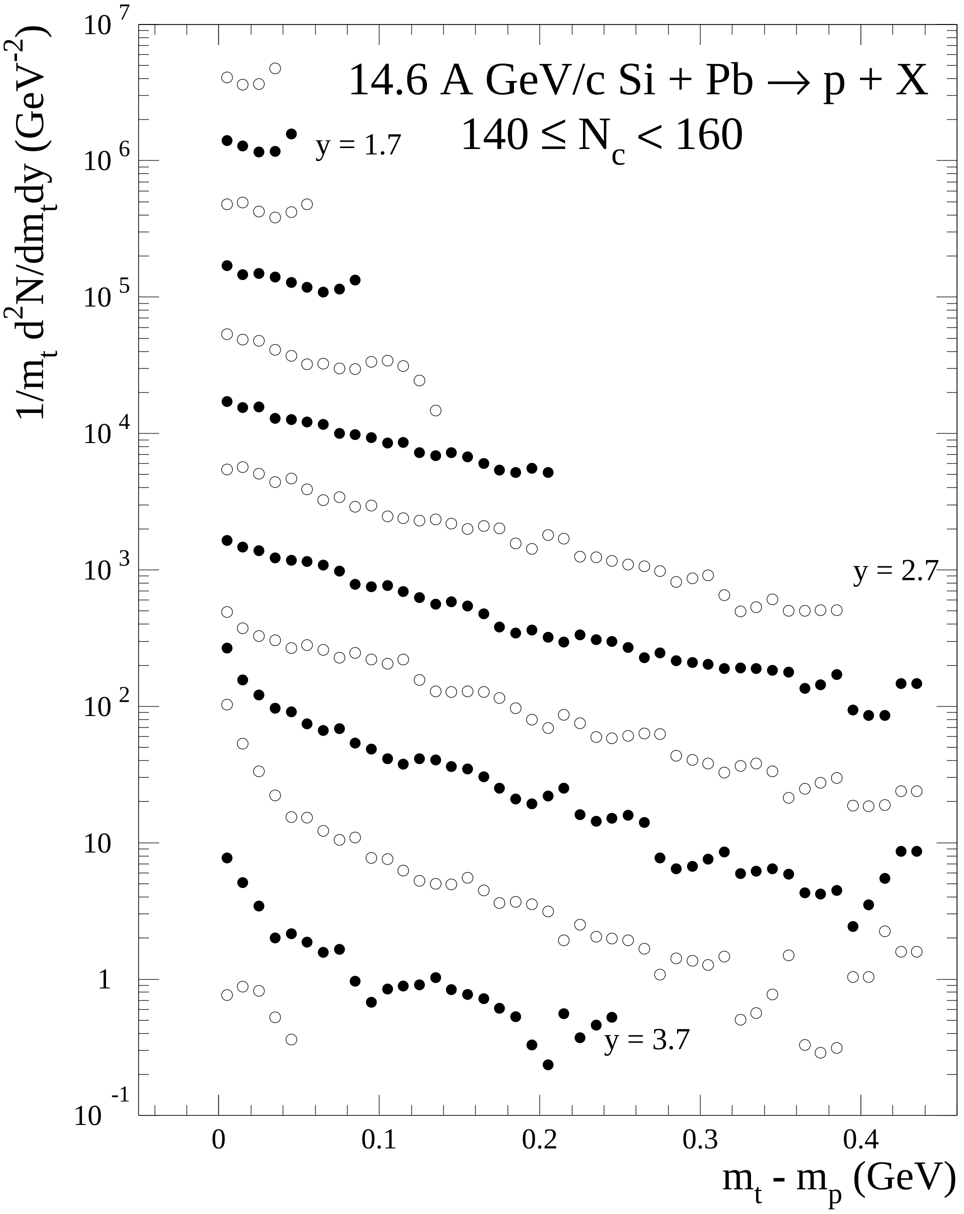

Figure 5.5: Proton invariant multiplicities *vs.* transverse mass for Si + Pb in 0.2 unit rapidity bins for $140 \leq N_c < 160$.

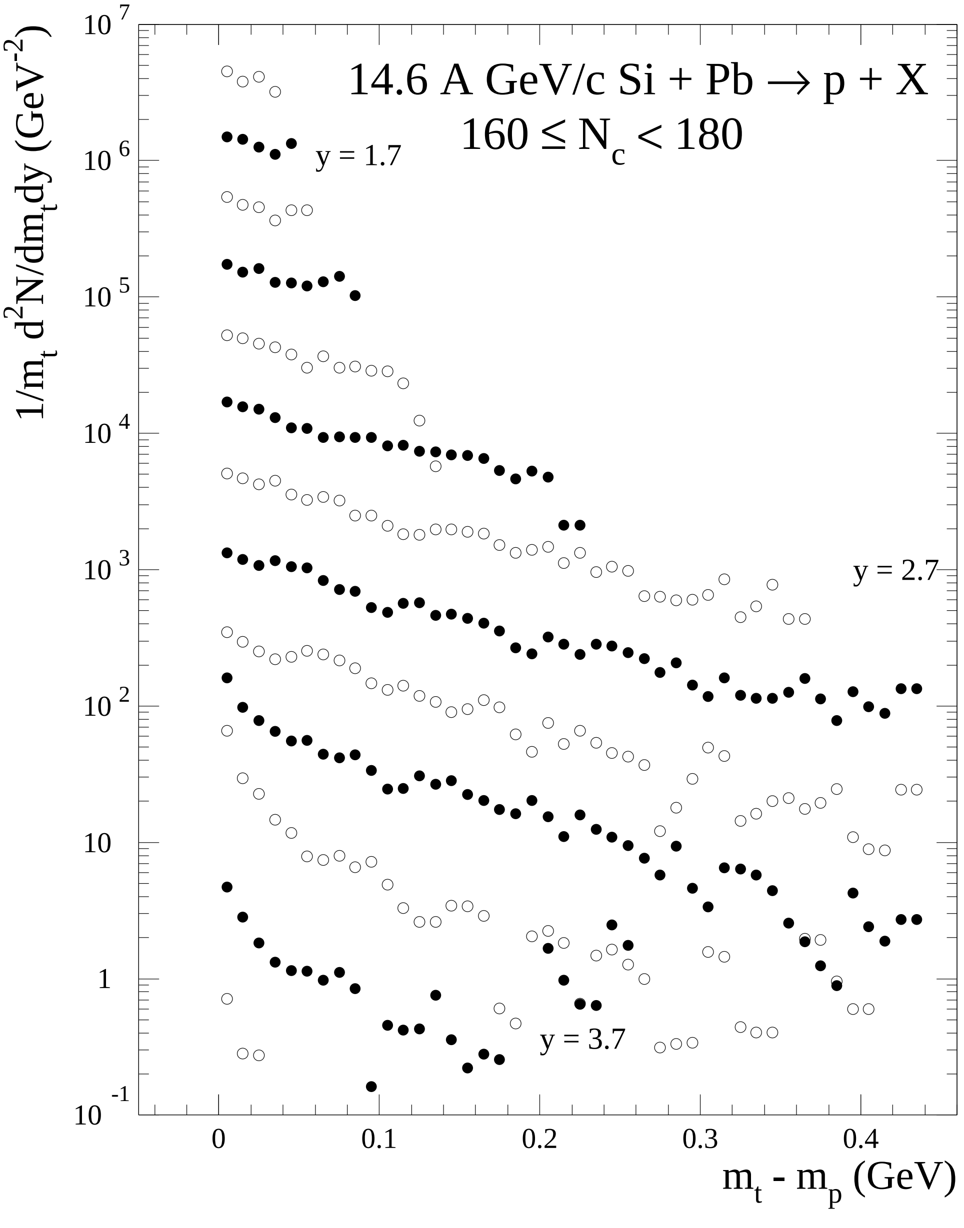

Figure 5.6: Proton invariant multiplicities *vs.* transverse mass for Si + Pb in 0.2 unit rapidity bins for $160 \leq N_c < 180$.

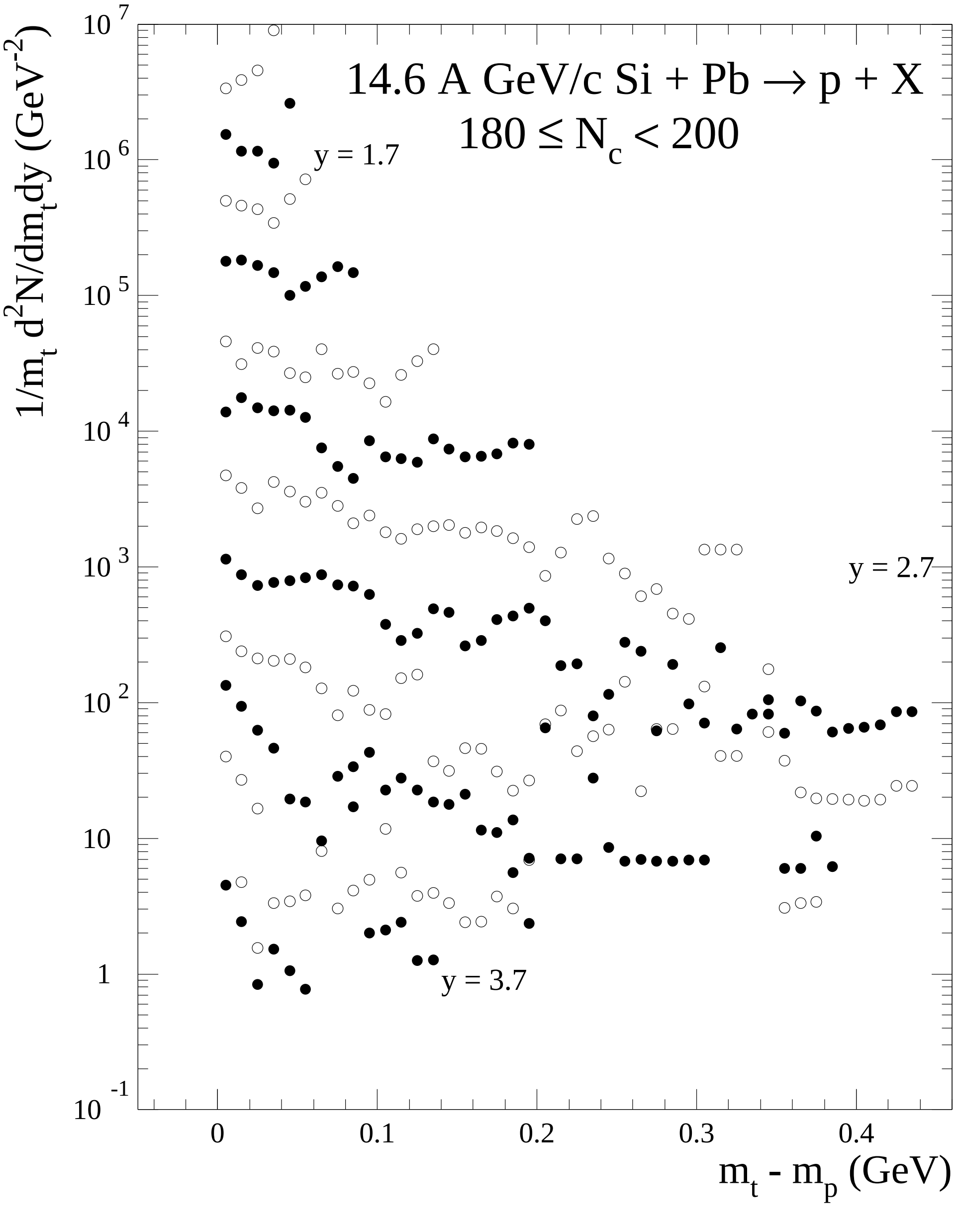

Figure 5.7: Proton invariant multiplicities *vs.* transverse mass for Si + Pb in 0.2 unit rapidity bins for $180 \leq N_c < 200$.

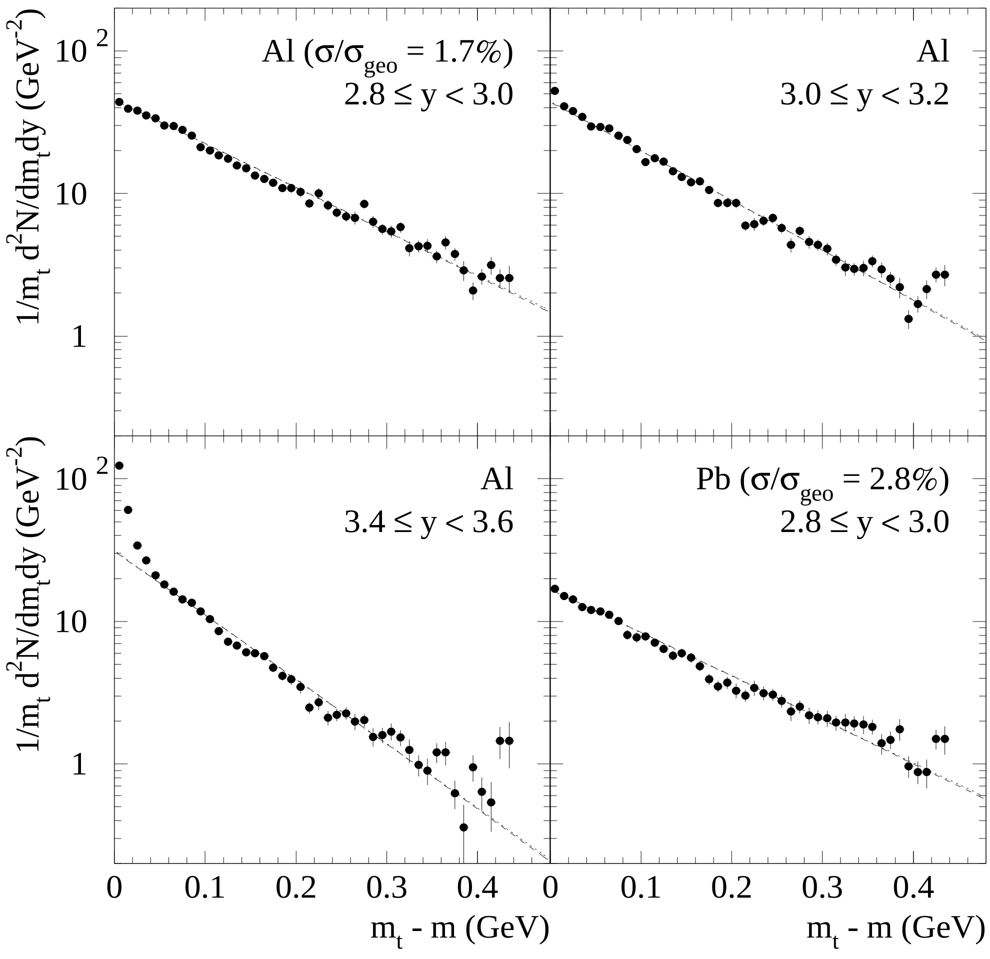

Figure 5.8: Proton invariant yields *vs.* transverse mass for 14.6A GeV/c Si + Al ($60 \leq N_c < 80$), Pb ($140 \leq N_c < 160$) $\rightarrow$ p + X at different rapidities. In each panel are plotted two fits: the dashed line is a Boltzmann curve, and the dotted line is an exponential. The two curves are virtually indistinguishable. Errors are statistical.

identify with protons that interact at most elastically in these collisions. For Si + Al and for the less central Si + Pb, the target and projectile do not fully overlap, so some of these protons are projectile "spectators" that do not interact with the target nucleus because they do not make contact with it. This component is present even in central Si + Pb collisions, however, where the target and projectile fully overlap, so all projectile nucleons encounter the target nucleus. The steep component near $p_t = 0$ and beam rapidity corresponds to the small fraction of projectile protons that do not undergo a strong interaction in traversing the target nucleus. This component has been discussed in detail previously [Bar 92a, Bar 90] and will not be further addressed here. In rapidity bins where this component is present, it has been excluded from the slope fits, but it is of course included when we later compute dN/dy by integrating over m_t.

Figs. 5.9 and 5.10 show proton slope parameters T_B and T_0 *vs.* rapidity y for several different centralities in the systems Si + Al and Si + Pb, respectively. These numbers are tabulated in App. F. The open symbols for the nearly symmetric system in Fig. 5.9 are reflections of the solid symbols about $y = 1.7$. In each figure, T_B is plotted in the top panel along with two extrapolations, labeled A and B, used later to compute dN/dy. In the bottom panel of each figure, T_0 from our measurement is plotted along with data from E802 [Abb 94] and extrapolations A′ and B′ of T_0 equivalent to the extrapolations A and B of T_B indicated in the top panel.

Now we wish to determine the degree to which T_B reflects the actual temperature of the system. Comparison of T_B with pion, kaon, lambda and

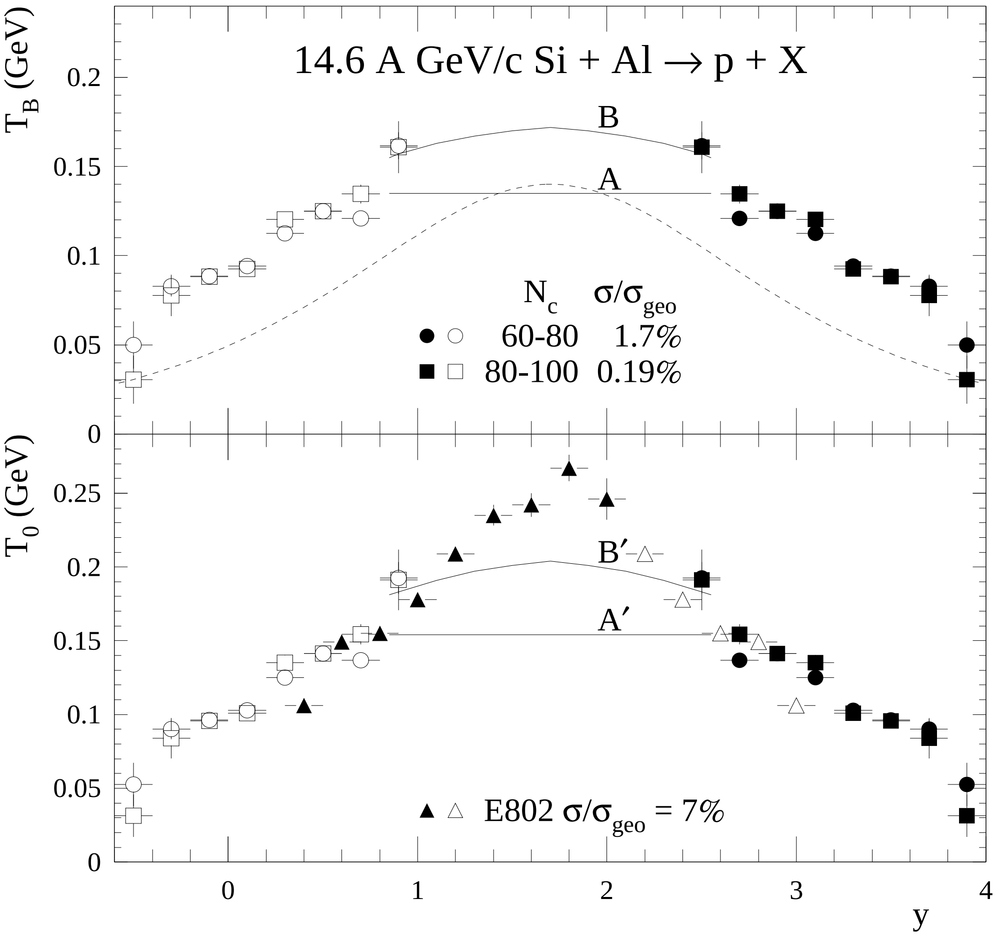

Figure 5.9: Proton transverse mass inverse slope parameters as a function of rapidity for two different centralities. In each case, the data from $y > 2.4$ (solid symbols) are reflected about $y = 1.7$ and plotted for $y < 1.0$ (open symbols). The top panel also shows the two extrapolations, labeled A and B, used to obtain dN/dy. The bell-shaped dashed curve in the top panel indicates the prediction for an isotropically emitting thermal model with 140 MeV temperature. The results from E802 [Abb 94] are shown for the top 7% of the geometric cross-section, again reflected about mid-rapidity. Also shown in the bottom panel are extrapolations A′ and B′ of T_0 equivalent to the extrapolations A and B of T_B in the top panel.

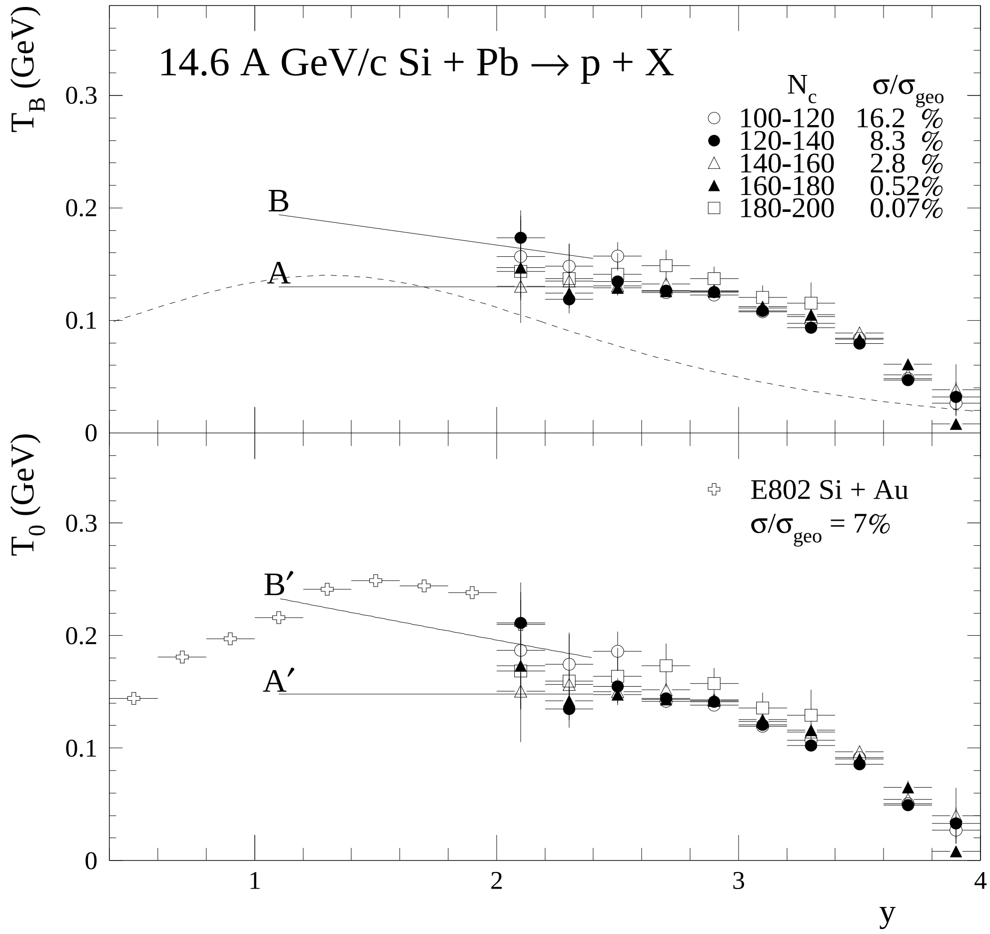

Figure 5.10: Proton transverse mass inverse slope parameters as a function of rapidity for different centralities. The top panel shows the two extrapolations, labeled A and B, used to compute dN/dy. The bottom panel shows T_0 as measured by E802 [Abb 94] for the top 7% of the geometric cross-section and two extrapolations, labeled A′ and B′ equivalent to A and B in the top panel. The dashed curve is the prediction of an isotropically emitting thermal model with 140 MeV temperature and center-of-momentum rapidity $y_{\mathrm{cm}} = 1.3$.

deuteron slopes [Par 92, Sta 92, Sta 93] shows no dependence on beam momentum if rapidity is normalized to the beam rapidity and the same centrality is selected. Near midrapidity the slope parameter T_B does increase systematically with particle mass, however, suggesting transverse expansion of the system with uniform velocity. Since T_B is a measure of a particle's average transverse momentum, one expects a contribution from thermal motion in the form of a temperature and an additional contribution proportional to $m\gamma\beta_t$, where β_t is the mean transverse expansion velocity. If β_t is the same for all particle species, heavier particles will have larger mean transverse momenta, and larger values of T_B. An independent measure of the temperature is obtained from the population of nucleon resonances [Bro 91] and our data on pion spectra give a value of $T = 140 \pm 20$ MeV [Sta 93, Hem 93, Bar 94c]. Using this temperature, simultaneous consideration of deuteron, proton, kaon and pion transverse slopes has yielded an average transverse expansion velocity of 0.33–0.39 [Bra 94]. Costales performed a similar investigation, but without this additional constraint on the temperature, he obtained somewhat different numerical results [Cos 90].

If the system were emitting particles isotropically, one would expect to see slopes similar to what is indicated by the bell-shaped curves in the top panels of Figs. 5.9 and 5.10, *i. e.,* $T_B = T\,\mathrm{sech}(y - y_{\mathrm{cm}})$, where $T \approx 140$ MeV is the system's temperature. The proton slope parameters lie well above these curves in each case, indicating a significant additional effect, such as the transverse flow discussed above. Longitudinal expansion, if present, will broaden the rapidity dependence of T_B, also raising the measured values at forward and backward rapidities. Note that in the absence of any other information, an isotropic model fit to the proton slopes alone would yield $T \gtrsim 225$ MeV for Si + Al and even higher values for Si + Pb. Such a high temperature is inconsistent with direct data on nucleon resonance populations [Hem 93, Bar 94c] and slopes of transverse momentum spectra for other hadrons, in particular pions [Abb 94]. Furthermore, even assuming these high temperatures, an isotropic thermal model does not reproduce in detail the rapidity dependence shown in Figs. 5.9 and 5.10 (see also the discussion in Refs. [Bar 93a, Dee 93, Bar 94b]).

In Fig. 5.10, we see for $y > 2.6$ a systematic increase in T_B in the most central collisions. To show this effect clearly, we present in Fig. 5.11 T_B *vs.* N_c for Si + Pb in several different rapidity bins. In each case, we observe a small but systematic increase in T_B with increasing centrality. This is demonstrated in the insert in Fig. 5.11, where we have plotted $\Delta T_B \equiv T_B|_{N_c=190} - T_B|_{N_c=110}$ *vs.* rapidity. In each bin, ΔT_B is significantly greater than zero. From a simple geometric model, one expects full overlap between between the Si and Pb nuclei when $\sigma/\sigma_{\rm geo} = 10\%$, or when $N_c \approx 120$, but the increase in T_B occurs well above that value. This effect may indicate the onset of a phase transition as predicted by van Hove [Van 82] and born out by later hydrodynamic calculations [Kat 86, Ruu 88].

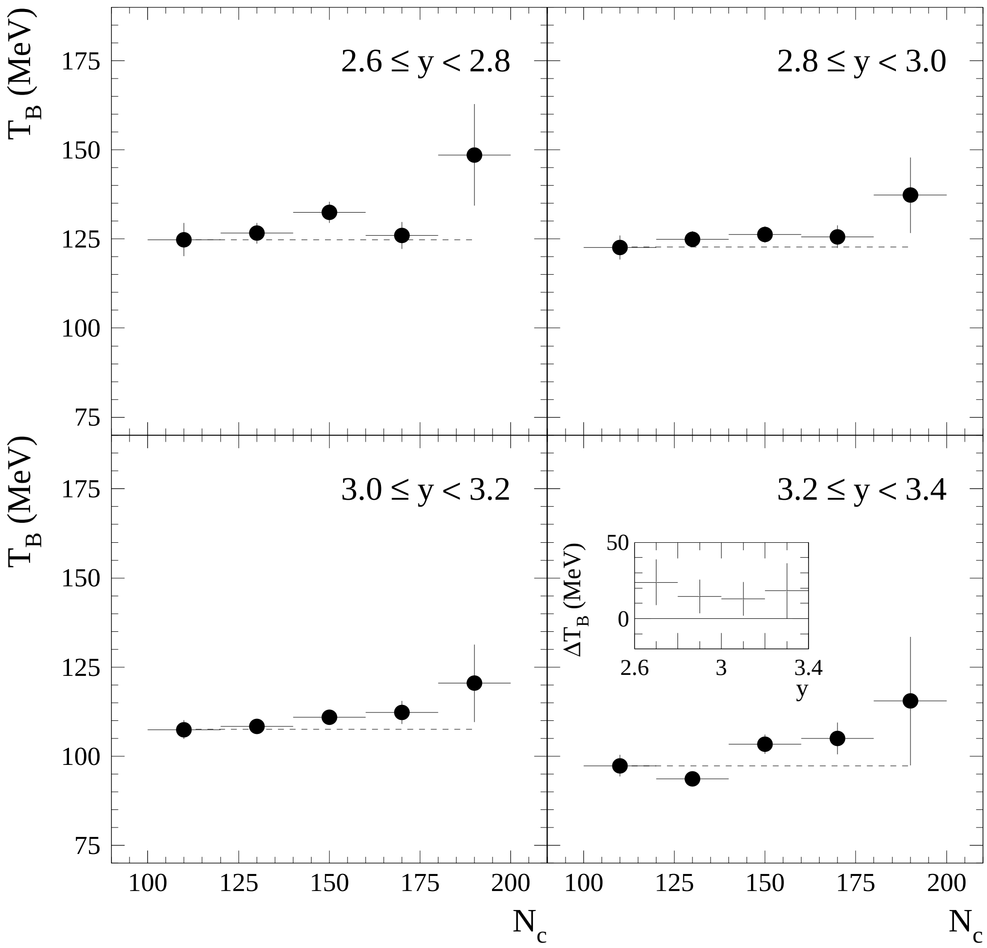

Figure 5.11: Proton transverse mass inverse slope parameters T_B as a function of charged-particle multiplicity for Si + Pb in different rapidity bins. A horizontal line through the first data point is shown to illustrate the gradual centrality dependence of the data. The insert in the last panel shows $\Delta T_B \equiv T_B|_{N_c=190} - T_B|_{N_c=110}$ with statistical error as a function of rapidity.

Chapter 6

Proton Rapidity Distributions

As indicated in Fig. 4.13, the spectrometer's acceptance in p_t decreases rapidly below $y \approx 2.4$. Forward of this rapidity, most protons are accepted, regardless of their transverse momenta, and we have good sensitivity to T_B. Therefore, integrating the double differential multiplicity to the acceptance limit yields most of the rapidity distribution dN/dy, and we extend the integral to arbitrarily large p_t analytically using the parametrization in Eq. (1.4). Below $y \approx 2.4$, however, the integral to the acceptance limit forms a diminishing fraction of dN/dy and we cannot precisely determine the slope of the p_t spectrum; but we do measure the magnitude of the spectrum, in particular the intercept at $p_t = 0$. We can therefore deduce dN/dy in this region if we assume values for T_B by extrapolating the data from the region where we do measure them to the lower rapidities. The curves labeled A and B in the upper panel of each of Figs. 5.9 and 5.10 indicate two different extrapolations considered for each target. Using extrapolation A in each case forms essentially a lower bound on dN/dy since all available data show a systematic increase of slopes toward mid-rapidity [Sta 92], and dN/dy is an increasing function of T_B for a fixed intercept at $p_t = 0$. We consider extrapolation B a more realistic estimate, but it places by no means an upper limit on dN/dy. We tabulate the values of dN/dy thus obtained, using extrapolation B for $y < 2.4$, in App. F.

The squares and circles in Fig. 6.1 are the resulting rapidity distributions for Si + Al for two different centrality bins using for $y < 2.4$ extrapolation B. The results of using extrapolation A are indicated for each centrality by a line for $1.1 < y < 2.3$. The variation in dN/dy between the two different extrapolations gives us an estimate of about 20% for the systematic error on our measurement at mid-rapidity.

Though the parametrization given in Eq. (1.4) depends exponentially on T_B, dN/dy varies only slowly with the slope parameter. Our measurement fixes the $p_t = 0$ intercept, A_B. Varying the slope makes the biggest difference at large p_t, where the yield is very small. More precisely, using the notation of Eq. (1.4):

$$\frac{dN}{dy} = \int_m^\infty \frac{d^2N}{dm_t\,dy} dm_t = A_B\, m T_B \left(1 + 2\frac{T_B}{m} + 2\frac{T_B^2}{m^2}\right). \tag{6.1}$$

Since T_B is considerably less than the proton mass and A_B is fixed by our measurement, dN/dy depends essentially linearly on the value of T_B used.

For the most central collisions, corresponding to $80 \leq N_c < 100$ or $\sigma/\sigma_{\text{geo}} = 0.19\%$, the general shape of the rapidity distribution in the bottom panel of Fig. 6.2 is fairly flat over three units of rapidity, with no peak near beam rapidity, indicating no significant nuclear transparency even in this relatively small, symmetric system. For a thermal system isotropically emitting

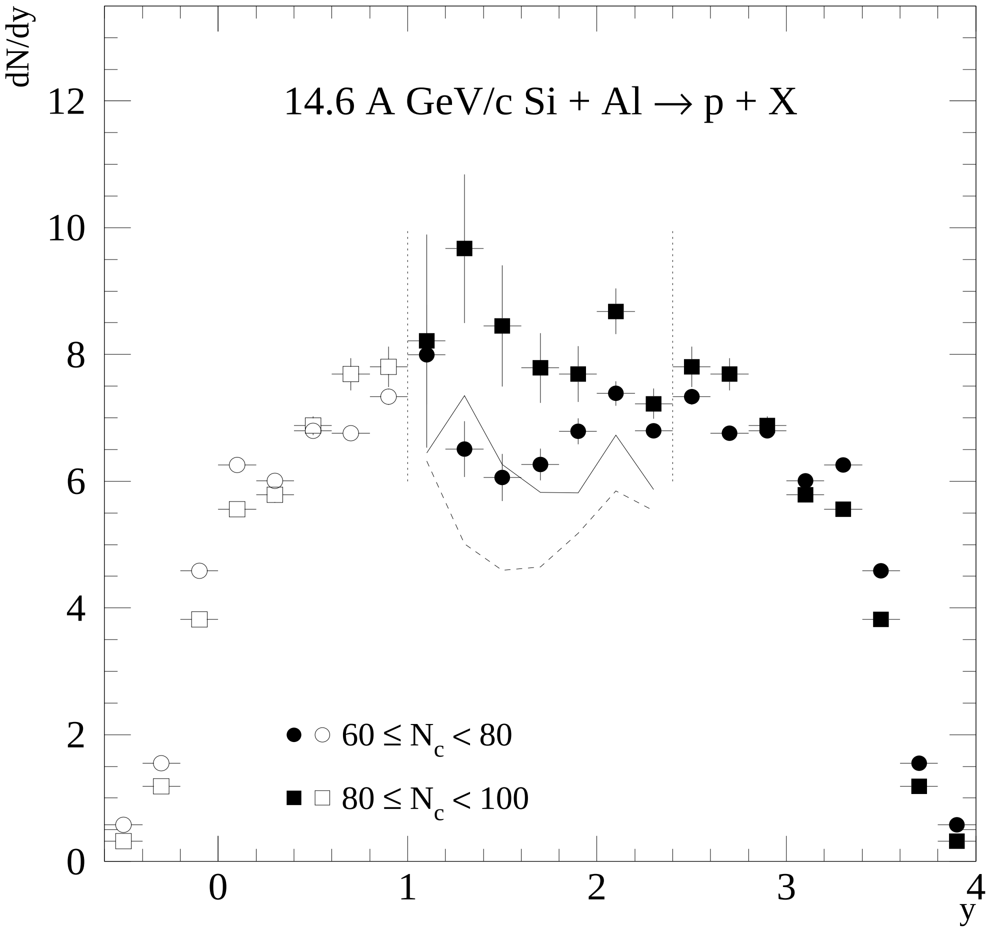

Figure 6.1: Proton rapidity distributions for Si + Al, two different centralities. The points plotted for $1 < y < 2.4$ are the results of using extrapolation B of T_B (see Fig. 5.9). The solid line indicates the results of extrapolation A for the more central data. The dashed line is the same for the less central data. The vertical dotted lines at $y = 1.0$ and 2.4 delimit the region where we use extrapolated values of T_B to compute dN/dy.

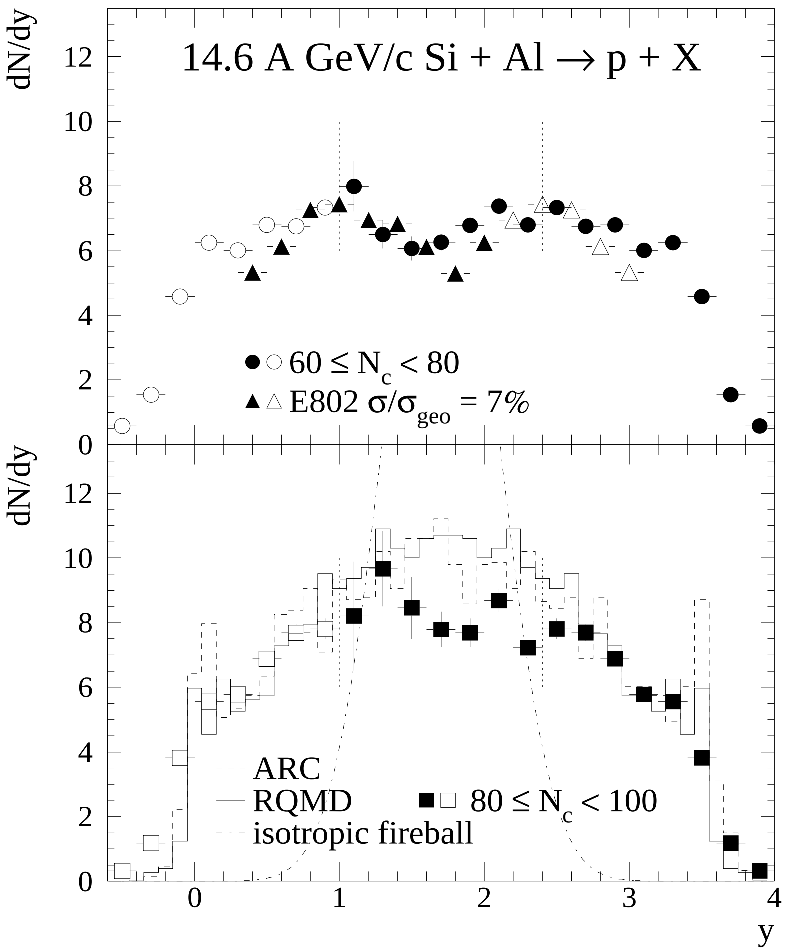

Figure 6.2: Proton rapidity distributions for Si + Al. The top panel compares the data for $\sigma/\sigma_{\text{geo}} = 2\%$, using extrapolation B in the midrapidity region, with data measured by E802 for $\sigma/\sigma_{\text{geo}} = 7\%$ [Abb 94]. The bottom panel compares the data for $\sigma/\sigma_{\text{geo}} = 0.2\%$ with several models.

protons, one expects from Eq. (6.1):

$$\frac{dN}{dy} \propto e^{-\alpha}\left(1 + 2\alpha^{-1} + 2\alpha^{-2}\right) \tag{6.2}$$

where $\alpha = (m/T)\cosh(y - y_{\text{cm}})$. When $m = 938$ MeV/c^2, the proton mass, and $T = 140$ MeV, this distribution is well approximated by a Gaussian with $\sigma = 0.38$, a distribution much narrower than the data. The mean proton energy loss in the collision center-of-momentum frame computed from the upper half of the rapidity distribution in Fig. 6.2 is 0.91 GeV, 52% of the initial proton kinetic energy in this frame. The mean rapidity shift of projectile protons $\langle \Delta y \rangle$ is 0.85, in exact agreement with Parsons' analysis of E802 data [Par 93]. This could be an indication of incomplete stopping: 61% compared to the value of $\langle \Delta y \rangle \approx 1.4$ computed from the isotropic distribution in Eq. (6.2) for $T = 140$ MeV (see Appendix B).

Alternately, the larger width of the proton rapidity distribution may also indicate longitudinal expansion of the system after stopping. In the collision center-of-momentum frame, the mean rapidity of forward-going protons $\langle y_{\text{cm}} \rangle$ is 0.87, so the mean longitudinal velocity is $\langle \beta_z^{\text{cm}} \rangle = \tanh\langle y_{\text{cm}} \rangle = 0.70$. The mean rapidity-averaged transverse momentum $\langle p_t \rangle$ is 610 MeV/c, and the mean energy $\langle E_{\text{cm}} \rangle$ is 1.79 GeV, so the mean transverse velocity $\langle \beta_t^{\text{cm}} \rangle = \langle p_t \rangle / \langle E_{\text{cm}} \rangle = 0.34$, about half of the mean longitudinal velocity. The observed shape of the rapidity distribution is indeed well reproduced by a source expanding longitudinally with velocity $\langle \beta_z^{\text{cm}} \rangle \gtrsim 0.5$ [Bra 94]. From consideration of transverse momentum spectra of different particle species, as discussed in Ch. 5 above, a transverse expansion velocity of about 0.33–0.39 can be deduced [Bra 94], indicating that longitudinal expansion considerably exceeds transverse expansion. A study of longitudinal velocities β_z *vs.* time in the hadronic cascade model RQMD [Xu priv] has shown a steep decrease during the first few fm/c after the start of the collision, followed by a gradual increase until pions and protons have the same longitudinal velocity of about 0.6. This result supports the hypothesis of strong stopping and subsequent longitudinal expansion that explained inclusive E_t and N_c distributions [Bra 89].

Also plotted in Fig. 6.2 are rapidity distributions from the ARC [Sch 92] and RQMD [Sor 89, Jah 92] hadronic cascade codes. These results are obtained by imposing experimental cuts on the events generated by the models, not by selecting the impact parameter; the total charged particle multiplicity into the acceptance of the E814 multiplicity detector is selected just as in the data. The overall agreement is good, though at mid-rapidity both models lie above the data. This discrepancy could be resolved by increasing the values of T_B we use to compute dN/dy below $y = 2.4$, which would in fact be closer to E802's measurement of T_0, but it would worsen our agreement with the E802 measurement of dN/dy (see below).

Both models predict small peaks at target and beam rapidities ($y = 0$ and 3.4) which are not present in the data. The model predictions do not exhibit such behavior in the asymmetric system Si + Pb, however (see Fig. 6.6 below). Since the peaks are only present in the nearly symmetric system, where full overlap occurs with vanishing probability, they are probably due to details in the nuclear surface parametrization.

The proton rapidity distribution measured by E802 [Abb 94] in Si + Al for the upper 7% of the geometric cross-section is also plotted in the top panel of Fig. 6.2. Again, the solid triangles are the directly measured data; the open ones are the same data reflected about mid-rapidity. These data lie below ours at mid-rapidity, but they are for less central collisions. For Si + Pb collisions (shown in Fig. 6.4 below) we see significant changes in dN/dy with centrality increasing even well beyond the value of $\sigma/\sigma_{\text{geo}} \approx 10\%$ expected for full nuclear overlap in a simple geometric model, and we observe a significant increase at mid-rapidity with increasing centrality in the Si + Al data in Fig. 6.1 even in very central collisions. Therefore the larger dN/dy values in our data at $\sigma/\sigma_{\text{geo}} = 1.7\%$ and 0.2% as compared to the more peripheral E802 data are expected. Note that in fact for the points at mid-rapidity, we have used slope constants below the ones measured by E802 for more peripheral collisions (see Fig. 5.9).

With decreasing N_c, one observes the formation of a sharper shoulder, though still not a peak, near beam rapidity in the Si + Al proton rapidity distribution, and a corresponding decrease in the central region. The decrease at mid-rapidity is somewhat larger than the increase at the forward rapidities, however. Table 6.1 shows the integral $N_p \equiv 2\int_{1.72}^{4.0} dN/dy \cdot dy$ of the proton rapidity distribution in each N_c bin for the two different extrapolations of T_B (N_p^A and N_p^B) and the number of statistical standard deviations N_σ by which the two integrals differ for each extrapolation. This demonstrates that the increase in total proton multiplicity with increasing N_c is significant. Note that this does not include the possible effect of an increase in T_B with centrality; where a slope is not measured, dN/dy is computed using the same value of

Table 6.1: Total proton multiplicity N_p in Si + Al for different charged-particle multiplicity bins. The proton multiplicity $N_p^{\rm tot} \equiv N_p^B + 1.4$ in the third column is adjusted for Λ hyperon and deuteron production (see text). The numbers in parentheses for RQMD and ARC in the last columns include an estimated 1.3 protons lost to Λ hyperon production in the models. Errors are statistical.

N_c	N_p^A	N_p^B	$N_p^{\rm tot}$	$N_p^{\rm ARC}$	$N_p^{\rm RQMD}$
70	23.0 ± 0.1	25.3 ± 0.2	26.7 ± 0.2	29.1 (30.4)	29.2 (30.0)
90	23.5 ± 0.3	26.3 ± 0.3	27.7 ± 0.3	29.8 (31.1)	29.7 (30.5)
N_σ	1.6	2.8	2.8		

T_B at a given rapidity for each centrality. The increase may be an effect of triggering on extremely large charged particle multiplicities.

Baryon number, charge and isospin are of course still conserved, but the overall proton multiplicity may be affected by production of hyperons, light nuclei, proton-antiproton pairs (although negligible here [Bar 93b]), and charge exchange. If more protons are produced due to charge exchange, the conservation laws imply fewer neutrons and more negative than positive and neutral pions. Requiring an increase in charged particle multiplicity essentially selects more resonance decays into charged particles, *e. g.,* $\Delta^0 \rightarrow \mathrm{p}\pi^-$ *vs.* $\Delta^0 \rightarrow \mathrm{n}\pi^0$. That this is a plausible explanation for this effect is in fact demonstrated by a similar variation of N_p with N_c in both ARC and RQMD, as shown in Table 6.1. Note that in spite of Λ production, at these large values of N_c, the total number of protons is greater than 29 in the models, significantly exceeding the 27 protons of the target and projectile nuclei. This effect underscores the importance of implementing experimental trigger conditions properly in models when comparing to data.

The total experimental number of protons N_p^B reported in Table 6.1 for each centrality is somewhat less than the corresponding numbers from ARC and RQMD. Although this discrepancy is of the same order as the systematic error, we still have to consider protons lost to production of hyperons and light nuclei. To estimate the effect of Λ hyperon production on the proton rapidity distribution, I used the GEANT package. We generated Λ particles with a Gaussian rapidity distribution having unit σ as observed by E810 [Eis 92b] and a Boltzmann-like transverse momentum distribution having T_B = 160 MeV

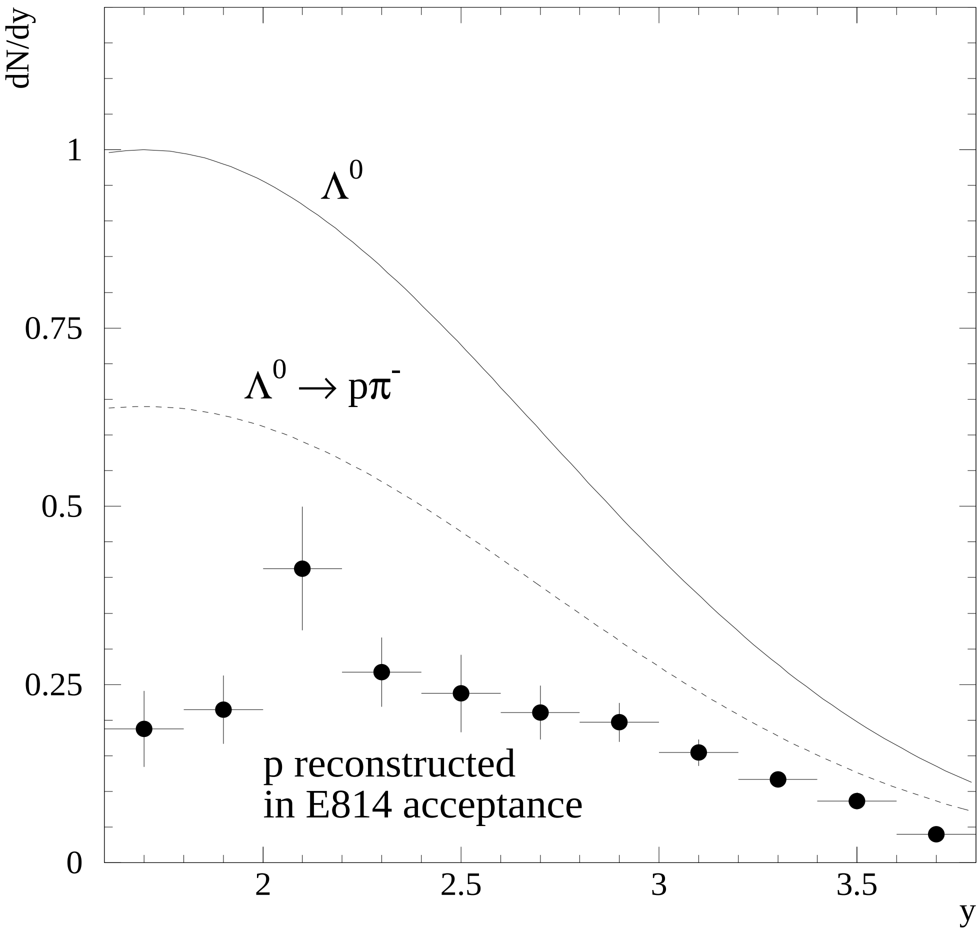

Figure 6.3: Rapidity distribution of charged tracks identified as protons from lambda decay in a GEANT simulation. The solid curve is the simulation input, chosen to resemble the measurement of E810 [Eis 92b] for Si + Si. The dashed curve is the solid one multiplied by the 64% branching ratio for lambda decay into protons and negative pions. The points indicate the multiplicity of those particles accepted in the E814 apparatus and reconstructed as protons.

independent of rapidity. These generated particles were tracked through the apparatus by GEANT, allowing them to decay along the way. For charged particles (protons and negative pions) from these decays that struck the tracking chambers and scintillators downstream and also pointed back into the magnet aperture, the momenta and flight path lengths were reconstructed in the same way as the data. GEANT also allowed computation of the time-of-flight of each particle. Using these reconstructed momenta, path lengths and times-of-flight, we calculated the "masses" of the particles via $m = p/\beta\gamma$, identified protons via the process outlined in Sec. 4.3 and computed the rapidity and transverse momentum spectra of these decay products as the analysis routine did with the data. The rapidity distribution of these reconstructed protons is shown in Fig. 6.3.

For each Λ that decays into a proton and negative pion (64%), we detect an average of 0.51 proton. Considering associated production in a system with nearly equal proton and neutron numbers, each Λ produced removes 0.5 proton from the system on average. For each Λ produced, therefore, we lose an average of $0.5 - 0.64 \times 0.51 = 0.17$ proton. Reference [Eis 92b] indicates that there are 2.5 Λ particles produced per collision, so we estimate an average of 0.43 proton lost to Λ production and decay per collision.

Next we consider the final-state protons bound in nuclei. In Ch. 7, we will show good agreement for the deuteron yields at $p_t = 0$ from both E814 and E802, despite differences in acceptance and centrality. We therefore use the overall deuteron yield of 1.0 per collision reported by Parsons [Par 93] for Si + Al. A measurement of $A = 3$ nuclei by E814 [Bar 94a] indicates that for these purposes nuclei heavier than deuterons can be neglected. We estimate that $0.43 + 1.0 \approx 1.4$ protons are not visible in the experimental proton data due to production of hyperons and light nuclei. Note that in the RQMD and ARC computations, the Λ particles produced do not decay. If 2.5 Λ particles are produced per collision, in accordance with the E810 data [Eis 92b], about 1.3 will be lost per collision, so the proton multiplicity from the model predictions should be increased by 1.3 for purposes of this comparison, as indicated by the numbers in parentheses in the last column. As indicated in Table 6.1, $N_p^{\mathrm{tot}} \equiv N_p^B + 1.4$, which includes the protons lost to hyperon and deuteron production, is still less than the models by about 3 protons, but this difference is within the systematic errors. Larger slope constants than we have used in our extrapolation for $y < 2.4$ would diminish the discrepancy, for example.

Next we turn to proton rapidity distributions in the asymmetric system Si + Pb, wherein the projectile completely overlaps the target nucleus in the upper 10% of the geometric cross-section. In Fig. 6.4 we plot dN/dy for several different centrality bins in Si + Pb collisions. Again we have used extrapolation B (see Fig. 5.10) to obtain the transverse-momentum-integrated rapidity distribution for $y < 2.4$, introducing by our estimate about a 20% systematic error in these values at midrapidity. We observe a very systematic decrease at forward rapidities and a corresponding increase at mid-rapidity with increasing centrality. As noted above, this effect persists well beyond the value of N_c expected for full overlap between the Si and Pb nuclei. This again emphasizes the importance of applying proper centrality cuts when comparing data to models or other experiments. For the least central events ($\sigma/\sigma_{\mathrm{geo}} < 16.2\%$), in

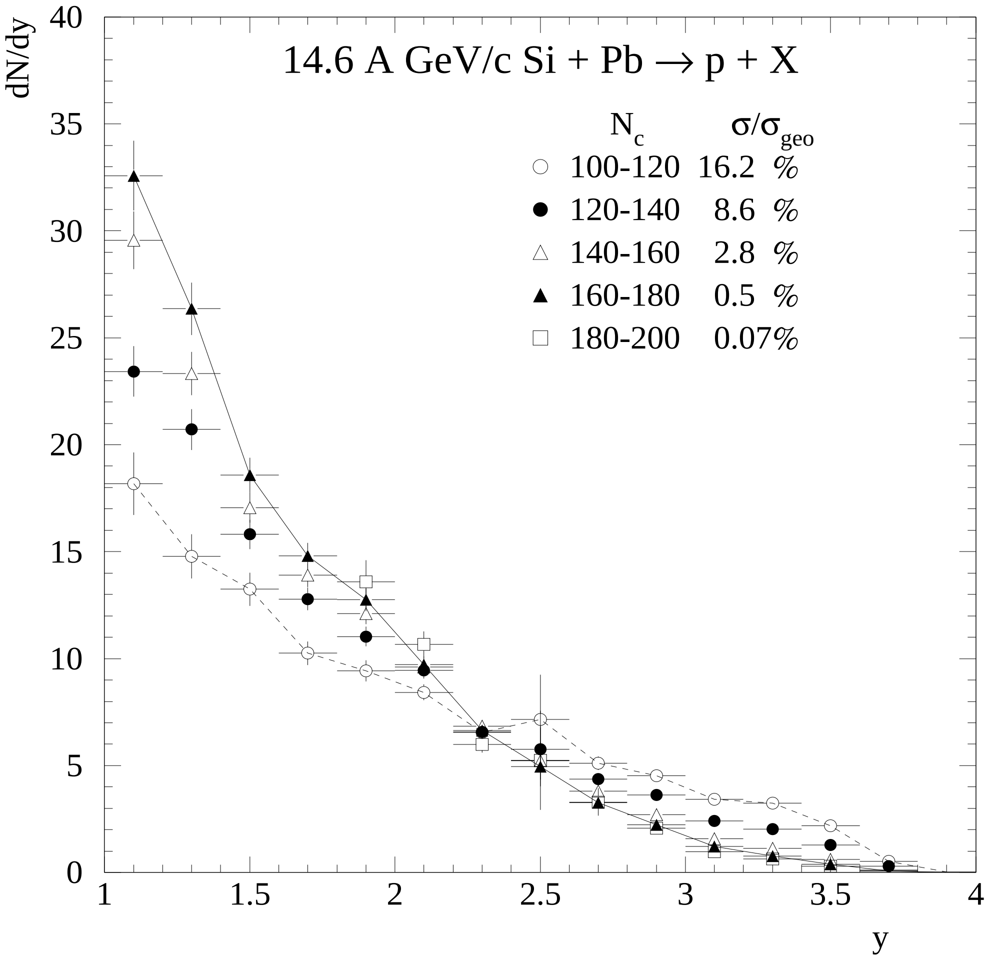

Figure 6.4: Proton rapidity distributions dN/dy for Si + Pb for different centralities.

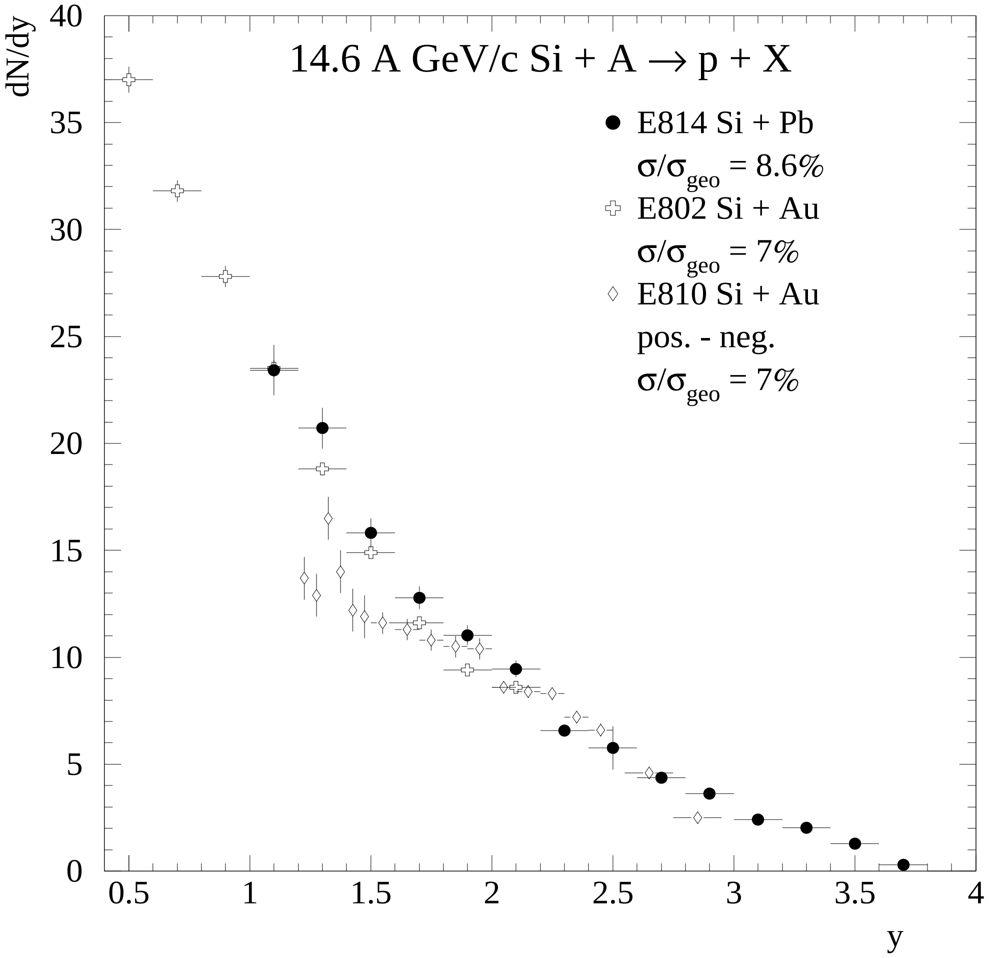

Figure 6.5: Proton rapidity distributions from Si + Pb compared with Si + Au data from E802 [Abb 94] and E810 [Eis 92a].

which the Si and Pb nuclei do not fully overlap, a shoulder begins to develop at $y = 3.4$, but for the higher centralities, there is no indication of any shoulder or peak at beam rapidity, indicating an absence of nuclear transparency at this beam energy.

In this asymmetric system beyond full overlap ($\sigma/\sigma_{\rm geo} \lesssim 10\%$), forward-going protons from the Si projectile nucleus must traverse more matter in crossing the Pb target nucleus (each projectile nucleon undergoes an average of 6–7 collisions crossing the target) than their counterparts in the target (each target nucleon in the overlap region experiences an average of about 3 collisions crossing the projectile nucleus), many of which are spectators and do not interact at all with the projectile nucleus. Hence, we obtain more information about stopping by studying the fate of projectile nucleons, which enter the collision with positive center-of-momentum rapidities. These nucleons can undergo large rapidity shifts, placing them in the backward center-of-momentum hemisphere after the collision, but we can obtain a conservative estimate of the mean rapidity shift by focusing on forward going final-state nucleons. We follow Parsons' [Par 93] lead and integrate the rapidity distribution down from $y = 4$ until we find 14 protons, the number in the projectile. Considering our data for $160 \leq N_c < 180$, the most central data where the statistics are still good, we find that $\int_{1.46}^{4.0} dN_p/dy \cdot dy = 14$, so for the sake of this argument, we consider all final-state protons above $y = 1.46$ to be projectile participants. We find the average rapidity in this range to be $\langle y \rangle = 2.01$, yielding an average rapidity shift $\langle \Delta y \rangle = 1.43$, in good agreement with Parsons' result for the top 7% of the geometric cross-section. This is a lower limit on the rapidity shift, since some of the protons in the region $y > 1.46$ may have originated in the target nucleus, so some of the projectile protons may have ended up below this rapidity. A measurement of neutron and proton multiplicities in Si + Pb collisions near $p_t = 0$ for $y > 1.6$ shows that the neutron-proton ratio in this region more closely resembles the 4:3 of the projectile-target-overlap cylinder system than the projectile's 1:1 [Bar 92a], suggesting that the colliding participants mix rather thoroughly. This suggests that the mean rapidity shift would be considerably larger than the lower limit of 1.43 deduced above. Ambiguity in the center-of-momentum frame for this asymmetric system precludes a measurement of the mean center-of-momentum energy or velocity, unfortunately.

Figure 6.5 compares our data for $120 \leq N_c < 140$ with data from E802 [Abb 94] and E810 [Eis 92a]. The agreement among the three experiments is generally good, especially considering differences in acceptance, centrality selection, and other systematics. Also, the E810 data are taken in a Time Projection Chamber (TPC) without particle identification, so the data plotted are the difference between the distributions of positive and negative particles, so what is plotted is dN_{diff}/dy where $N_{\text{diff}} = N_{\text{p}} + N_{\pi^+} - N_{\pi^-} + N_{\text{K}^+} - N_{\text{K}^-} + \ldots$. The proton multiplicity is modified mostly by any differences between the multiplicities of positive and negative pions and kaons. The E810 data fall somewhat below the other data sets for $y \lesssim 1.6$, but because the TPC covers the forward 20° or so, or $\eta \gtrsim 1.7$, above $y \approx 1.7$, the TPC accepts all transverse momenta. Below this, the TPC acceptance begins to run out, and the systematic errors increase. A previous comparison with E802 data

[Bar 93a, Abb 90, Abb 91] did not demonstrate such good agreement.

Figure 6.6 compares our data for $\sigma/\sigma_{\rm geo} = 0.5\%$ with predictions of RQMD [Sor 89] and ARC [Pan 92, Sch 92] as well as the transparent “fire-streak” model of Chapman and Gyulassy [Cha 91, Cha 92]. This last model is based on a fit to earlier published E802 data [Abb 90, Abb 91] at midrapidity for the top 7% of the geometric cross-section and predicts a peak at $y \approx 2.5$ based on conservation of baryon number, energy and momentum. It implies a nucleonic scattering length in the nuclear medium greater than 20 fm. The predictions of this model strongly contradict our data. The two cascade models achieve good agreement, however.

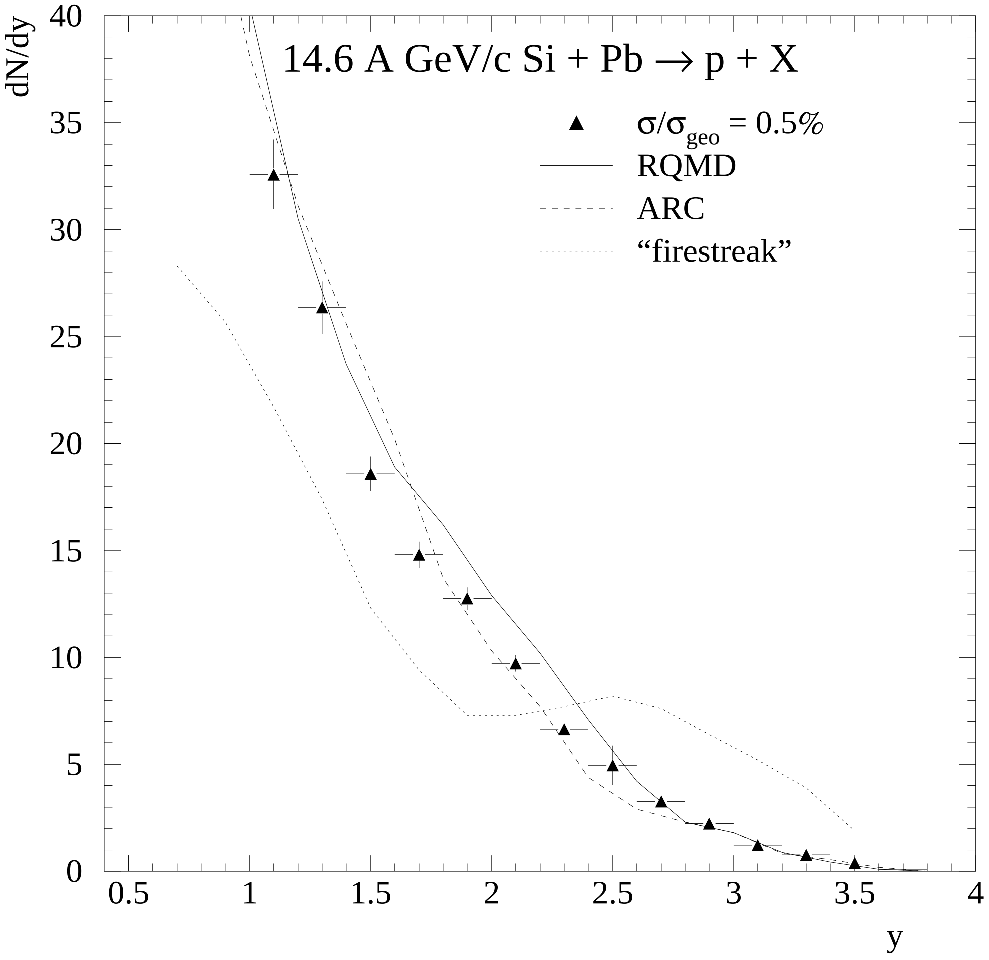

Figure 6.6: Proton rapidity distribution for Si + Pb, $160 \leq N_c < 180$ compared with predictions of RQMD [Sor 89], ARC [Pan 92, Sch 92] and the transparent "firestreak" model of Chapman and Gyulassy [Cha 91, Cha 92].

Chapter 7

Deuteron-Proton Ratios

We also observe deuterons in this data set. Because their rate is significantly lower than that of the protons, background from the tail of the proton distribution and from misidentified tracks becomes a serious consideration. To estimate the magnitude of this background, we analyzed the mass spectrum in each 1 GeV/c momentum bin (see Fig. 7.1), fitting the sum of Gaussians and a background function to each bin:

$$g(m) = C_p e^{-\frac{(m-m_p)^2}{2\sigma_p^2}} + C_d e^{-\frac{(m-m_d)^2}{2\sigma_d^2}} + Ae^{-Bm} + C, \tag{7.1}$$

where m_p and m_d are not the known proton and deuteron masses, but free parameters determined from the data. The nine parameters thus extracted were used to compute the ratio of the number of counts inside the deuteron gate used in the analysis to the number of deuterons in the Gaussian peak, above the background. The gate was determined visually to be the region of the mass axis where the deuteron peak was clearly visible. The deuteron and proton peak widths observed in Fig. 7.1 are well reproduced using the

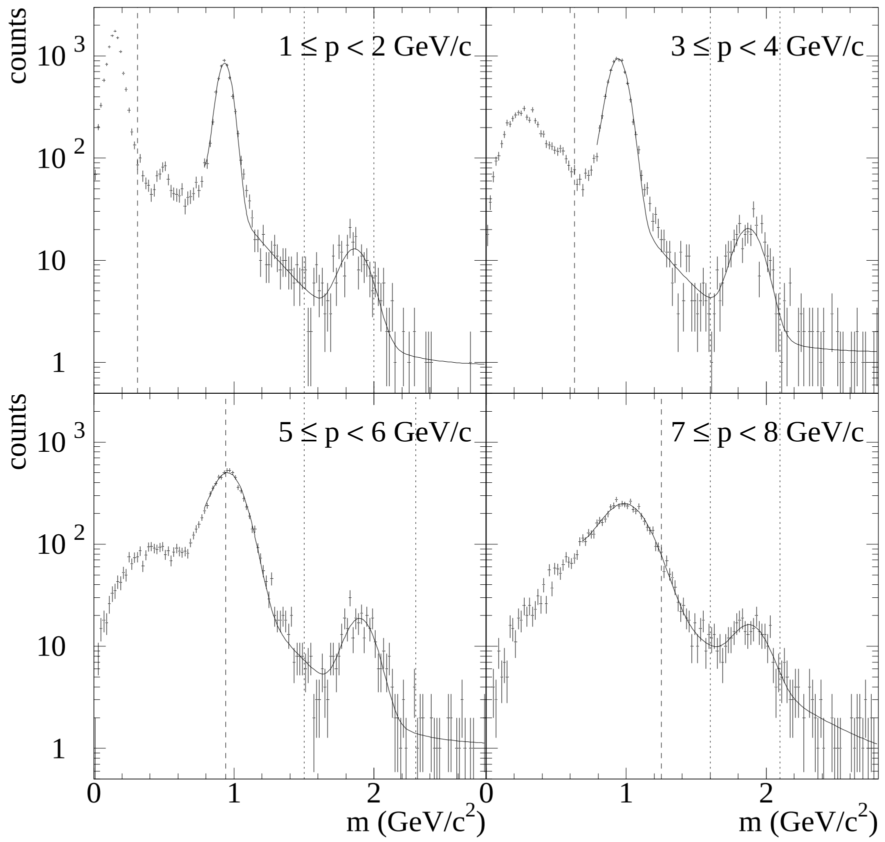

Figure 7.1: Mass spectra in 1 GeV/c momentum bins. Data for $m > 600$ MeV/c^2 are well described by the sum of two Gaussians and a background function, indicated by the solid lines plotted with each mass spectrum. A vertical dashed line is drawn where the velocity $\beta = 0.988$ for the highest momentum in each bin. To the right of this line in each bin particle identification is done using particle mass (see the discussion in Sec. 4.3). Dotted lines in each plot indicate the deuteron gates used. Errors are statistical.

momentum and time-of-flight resolutions quoted in Secs. 4.2.2 and 2.2 via

$$\left(\frac{\delta m}{m}\right)^2 = \left(\beta\gamma^2\right)^2 \left(\frac{\delta t}{z}\right)^2 + \left(\frac{\delta p}{p}\right)^2, \tag{7.2}$$

neglecting variations and uncertainties in particle flight paths.

Let the deuteron gate be delimited by two masses m_1 and m_2 ($m_1 < m_2$). The integral of the background function in this region is

$$\begin{aligned} N_{\mathrm{bg}}(\mathrm{gate}) &= \int_{m_1}^{m_2} \left(Ae^{-Bm} + C\right) dm & (7.3) \\ &= \frac{A}{B}\left(e^{-Bm_1} - e^{-Bm_2}\right) + C(m_2 - m_1). & (7.4) \end{aligned}$$

The tail of the proton distribution will also contaminate the deuteron sample. The number of protons in the deuteron gate will be

$$\begin{aligned} N_p(\mathrm{gate}) &= \int_{m_1}^{m_2} C_p e^{-\frac{1}{2}\frac{(m-m_p)^2}{\sigma_p^2}} dm & (7.5) \\ &= \sqrt{\frac{\pi}{2}} C_p \sigma_p \left[\mathrm{erf}\left(\frac{m_2 - m_p}{\sqrt{2}\sigma_p}\right) - \mathrm{erf}\left(\frac{m_1 - m_p}{\sqrt{2}\sigma_p}\right)\right], & (7.6) \end{aligned}$$

where

$$\mathrm{erf}(x) \equiv \frac{2}{\sqrt{\pi}} \int_0^x e^{-u^2} du \tag{7.7}$$

is the standard error function.

Similarly, the number of deuterons in the gate is

$$N_d(\mathrm{gate}) = \sqrt{\frac{\pi}{2}} C_d \sigma_d \left[\mathrm{erf}\left(\frac{m_2 - m_d}{\sqrt{2}\sigma_d}\right) - \mathrm{erf}\left(\frac{m_1 - m_d}{\sqrt{2}\sigma_d}\right)\right]. \tag{7.8}$$

The total number of deuterons is

$$N_d = \sqrt{2\pi} C_d \sigma_d. \tag{7.9}$$

Figure 7.2: Effective deuteron background $\xi_{\rm bg}$ *vs.* momentum for Si + Al, Pb. The line plotted with each histogram indicates the parametrization used when performing the background subtraction at each momentum.

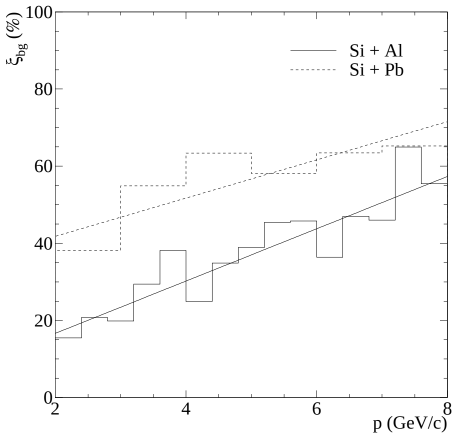

Taking into account that the deuteron gates do not admit all deuterons [$N_d > N_d(\text{gate})$], we compute the effective relative background

$$\xi_{\rm bg} = \frac{N_{\rm bg}(\text{gate}) + N_p(\text{gate}) + N_d(\text{gate}) - N_d}{N_{\rm bg}(\text{gate}) + N_p(\text{gate}) + N_d(\text{gate})}. \tag{7.10}$$

Hence

$$1 - \xi_{\rm bg} = \frac{N_d}{N_{\rm bg}(\text{gate}) + N_p(\text{gate}) + N_d(\text{gate})}. \tag{7.11}$$

The denominator in Eqs. (7.10) and (7.11) is the total number of counts in the mass gate that identifies deuterons. When we multiply this number by $1-\xi_{\rm bg}$, we obtain N_d, the total number of deuterons.

This background, for each target, is plotted in Fig. 7.2 in bins of momentum. In principle, this analysis should be done in bins of both rapidity and transverse momentum, but because the yields do not vary much with p_t at fixed rapidity within our limited deuteron acceptance, and we hence measure only the yields close to $p_t = 0$, there is a one-to-one correspondence between rapidity and the magnitude of momentum for our purposes. This background may also vary with centrality in principle, but visual inspection of the mass spectra as a function of centrality shows that it does not vary much, so we use a centrality-independent background subtraction. We parametrize the background with a linear function of momentum (solid and dashed lines in Fig. 7.2) which is used to correct the yields observed in the data. We estimate that this parametrization introduces a systematic uncertainty of about 15% into the low-transverse-momentum deuteron yields presented here.

Figure 7.3 shows the measured invariant deuteron yields near $p_t = 0$ determined from the present data. As suggested by Fig. 4.13, we have little sensitivity to the slopes of the deuteron spectra, which are essentially flat within our acceptance. We determine the $p_t = 0$ intercepts by averaging the relatively constant deuteron yields within our acceptance limits. Also shown are extrapolations to $p_t = 0$ of the E802 data [Par 92] using their measured fit parameters. Parsons tabulates both Boltzmann [Eq. (1.4)] and m_t-exponential [Eq. (1.5)] parameters for deuteron spectra. The difference in the intercepts obtained by using the two different parametrizations is negligible. The agreement is very good between the two experiments, especially considering the slight differences in centrality, target, and the uncertainty of the extrapolation. Figure 7.4 shows deuteron-proton ratios dN_d/dN_p near $p_t = 0$ for the Al and Pb targets and different centralities. Proton intercepts are determined by fits to the spectra in Figs. 5.1 to 5.7. The observed deuteron-proton ratios are

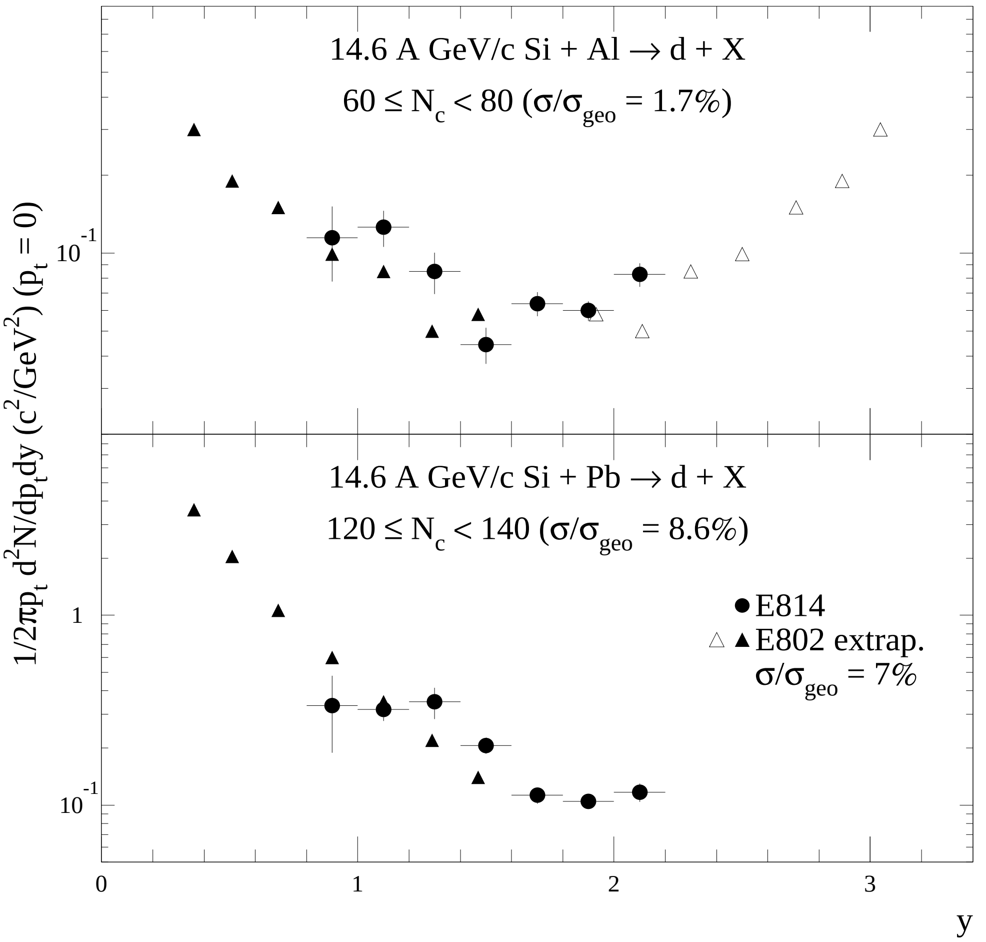

Figure 7.3: Low-transverse-momentum invariant deuteron yields. Along with the present data are shown extrapolations to $p_t = 0$ of data from E802 [Par 92] measured at larger p_t for Si + Al, Au collisions.

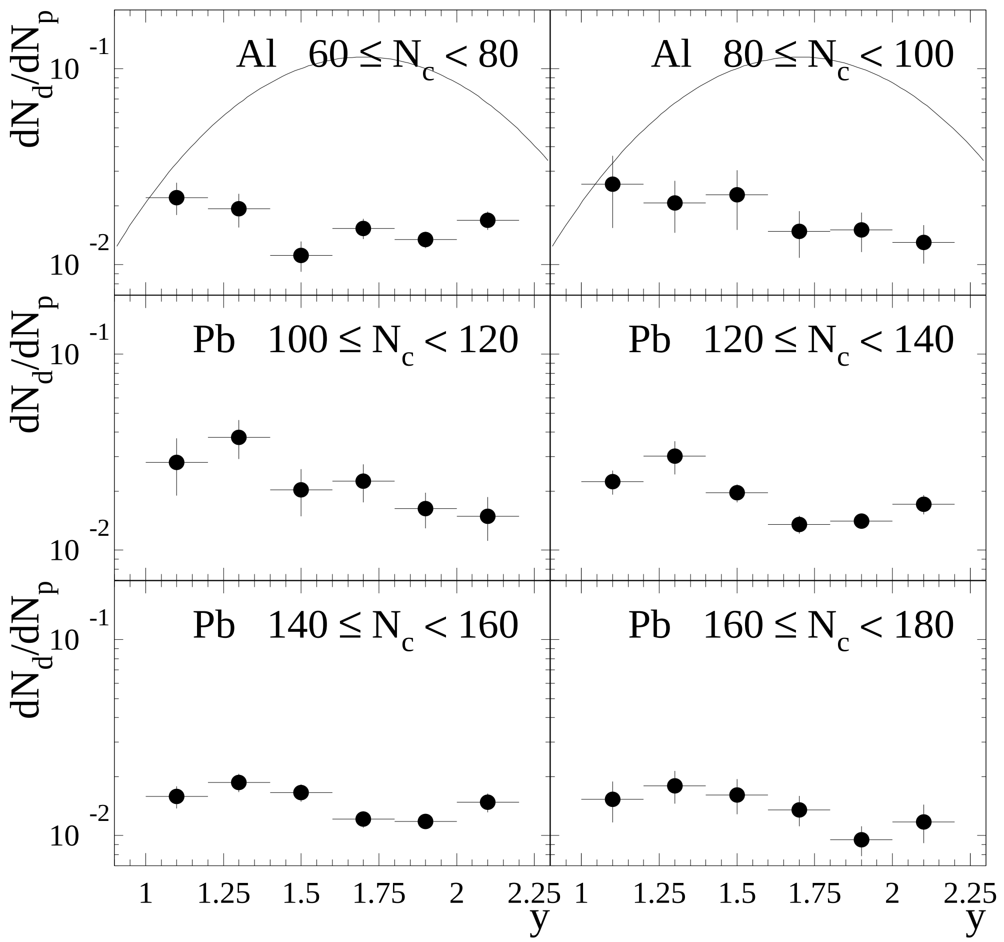

Figure 7.4: Low-transverse-momentum deuteron-proton ratios *vs.* rapidity for 14.6A GeV/c Si + Al, Pb $\rightarrow$ p, d + X at different centralities. The curves plotted in the top two panels for the Al target are the predictions of an isotropically emitting thermal model with 140 MeV temperature and 540 MeV baryon chemical potential.

rather low, about 1.5–3%, and show little dependence on centrality or rapidity. The agreement between the present deuteron yields and results obtained earlier in a different configuration of E814 [Bar 94a] over a smaller rapidity range is very good. Note that the ratios of the p_t-integrated deuteron and proton yields measured by E802 [Par 92] are larger—about 5%—because the measured deuteron slope constants are much larger than those of the protons.

Figure 7.4 also shows for Si + Al the prediction of an isotropic thermal model for the deuteron-proton ratio when $p_t = 0$ [*cf.* Eq. (1.4)]:

$$\lim_{p_t \to 0} \frac{d^2N_d/dy\, p_t dp_t}{d^2N_p/dy\, p_t dp_t} = \frac{m_d}{m_p} e^{-\frac{(m_d - m_p)\cosh(y - y_{\rm cm}) - (\mu_d - \mu_p)}{T}} \tag{7.12}$$

$$\approx 2 \exp\left(- \frac{m_n \cosh(y - y_{\rm cm}) - \mu_B}{T} \right) \tag{7.13}$$

where $m_d \approx 1.88$ GeV/c^2 is the deuteron mass, $m_{p,n}$ are the nucleon masses, $\mu_p = \mu_B = 510$–540 MeV is the baryon chemical potential, obtained from consideration of the volume, temperature and particle species ratios [Bra 93, Bra 94], $\mu_d = 2\mu_B$ is the deuteron chemical potential, and $T = 140$ MeV is the temperature. The temperature and the baryon chemical potential fix the magnitude of this ratio. The isotropic thermal curves (solid lines in Fig. 7.4) peak very sharply at mid-rapidity, in clear disagreement with the rather flat distribution of the data. Although a thermal model explains the data qualitatively [Bar 94a, Bra 94]—*e. g.,* it predicts the overall deuteron-proton ratio—it does not describe the differential distributions. This discrepancy appears to be another indication for longitudinal expansion. The protons have already been seen to be much wider than an isotropic distribution, and the deuterons are even wider.

Chapter 8

Conclusions

We have seen that proton transverse mass spectra are well described by Boltzmann parametrizations, a necessary though not sufficient condition for a thermalized system. Values of T_B as high as 150 MeV are observed for $y > 2.5$. These large values at forward rapidities, especially when considered simultaneously with those for other particle species, give a strong indication for transverse flow. For Si + Pb these values increase systematically with increasing centrality, even beyond the point of full overlap between the two nuclei—though one might improve on the statistical significance of this measurement. This result could indicate the onset of a phase transition.

We observe no significant nuclear transparency either in Si + Pb or in the symmetric system Si + Al. No peak is visible at or near beam rapidity in either system for very central collisions. This indicates a large degree of stopping and that a large baryon density is achieved in these collisions. In fact, to the extent that models like ARC and RQMD describe well the distributions of baryons in phase space, we can take seriously their predictions for configuration space distributions. RQMD [Sor 90] predicts a peak baryon density 7 times the normal nuclear value for central Si + Au collisions and an energy density of 1.75 GeV/fm^3, while ARC [Pan 92] predicts a peak baryon density around 8 times that of normal nuclear matter.

Our data for proton rapidity distributions agree well with those from other AGS experiments where they overlap. Among the different experiments we now have an almost complete measurement of the proton rapidity distribution over the entire rapidity interval for the asymmetric system Si + Pb (Au). The same is true for the symmetric system Si + Al, but using its symmetry and our extrapolation of T_B, E814 alone is able to provide a complete measurement of dN/dy in this case.

The rapidity distribution for Si + Al is much wider than that for an isotropically emitting thermal system, which may indicate only partial stopping, but more likely points to longitudinal expansion of the system after the collision. Deuteron-proton ratios at $p_t = 0$ are much flatter than for an isotropic thermal system as well, also suggesting longitudinal flow. Studies using RQMD support this hypothesis, indicating full stopping followed by longitudinal expansion.

We measure large projectile rapidity shifts at small impact parameters—0.85 for Si + Al, where the projectile nucleons undergo about 3 collisions each, and 1.43 for Si + Pb, where the projectile nucleons each experience more than 6 collisions—and in fact our measurements constitute a lower bound on the rapidity shift, which may be still larger. We conclude that at AGS energies we are still in the stopping regime, where large rapidity shifts imply large central baryon and energy densities. These large rapidity shifts at higher energies, such as will be achieved in the future at the Relativistic Heavy Ion Collider (RHIC) at BNL and the Large Hadron Collider (LHC) at CERN, will imply still higher central energy densities even when the central rapidity region is depleted of baryons.

The integral of the Si + Al rapidity distribution, which is the total number of protons in the final state, varies with charged particle multiplicity N_c. This effect is present in both ARC and RQMD as well. Selection of the charged particle multiplicity biases resonance decays to influence the number of protons in the final state.

The rapidity distributions of protons in both Si + Al and Si + Pb change significantly in even the most central collisions, well beyond full geometric overlap in the case of Si + Pb, demonstrating the importance of careful centrality selection when comparing data to models or other experiments.

Bibliography

[Abb 90] T. Abbott *et al.* (The E802 Collaboration), *Phys. Rev. Lett.* **64** (1990) 847.

[Abb 91] T. Abbott *et al.* (The E802 Collaboration), *Phys. Rev. Lett.* **66** (1991) 1567.

[Abb 94] T. Abbott *et al.* (The E802 Collaboration), *Phys. Rev. C* **50** (1994) 1024.

[Ani 80] R. Anishetty, P. Koehler and L. McLerran, *Phys. Rev. D* **22** (1980) 2793.

[Bar 85] T. Barklow *et al.,* SLAC scanner processor applications in the data acquisition system for the upgraded MARK II detector, SLAC–PUB–3781 (1985).

[Bar 90] J. Barrette *et al.* (The E814 Collaboration), *Phys. Rev. Lett.* **64** (1990) 1219.

[Bar 92a] J. Barrette *et al.* (The E814 Collaboration), *Phys. Rev. C* **45** (1992) 819.

[Bar 92b] J. Barrette *et al.* (The E814 Collaboration), *Phys. Rev. C* **46** (1992) 312.

[Bar 93a] J. Barrette *et al.* (The E814 Collaboration), *Z. Phys. C* **59** (1993) 211.

[Bar 93b] J. Barrette *et al.* (The E814 Collaboration), *Phys. Rev. Lett.* **70** (1993) 1763.

[Bar 94a] J. Barrette *et al.* (The E814 Collaboration), *Phys. Rev. C* **50** (1994) 1077.

[Bar 94b] J. Barrette *et al.* (The E814 Collaboration), *Phys. Rev. C* **50** (1994) 3047.

[Bar 94c] J. Barrette *et al.* (The E814 Collaboration), SUNY–RHI–94–10 (submitted to *Phys. Lett. B.*).

[Bev 92] P. R. Bevington and D. K. Robinson, *Data Reduction and Error Analysis for the Physical Sciences,* second ed. (McGraw-Hill, New York, 1992), 328 pp.

[Bir 53] G. Birkhoff and S. Mac Lane, *A Survey of Modern Algebra*, revised ed. (Mac Millan, New York, 1953), 472 pp.

[Bjo 76] J. D. Bjorken in *Current Induced Reactions,* Proceedings of the International Summer Institute on Theoretical Particle Physics, Hamburg 1975, edited by J. G. Körner, G. Kramer and D. Schildknecht (Springer-Verlag, Berlin, 1976), p. 93.

[Bra 84] H. Brafman *et al.,* The SLAC scanner processor: a fastbus module for data collection and processing, SLAC–PUB–3471 (1984).

[Bra 89] P. Braun-Munzinger and J. Stachel, *Phys. Lett. B* **216** (1989) 1.

[Bra 93] P. Braun-Munzinger for the E814 Collaboration in *Hot and Dense Matter,* Proceedings of the NATO ASI, Bodrum, Turkey, 1993, edited by W. Greiner, H. Stöcker and A. Gallmann (Plenum, New York, 1994), p. 419.

[Bra 94] P. Braun-Munzinger, J. Stachel, J. P. Wessels and N. Xu, SUNY–RHI–94–11 (to be published in *Phys. Lett. B.*).

[Bro 91] G. E. Brown, J. Stachel and G. M. Welke, *Phys. Lett. B* **253** (1991) 19.

[Bru 84] R. Brun *et al.,* GEANT 3 Users Guide, CERN Data Handling Division Report No. DD/EE/84-1, 1984 (unpublished).

[Bus 84] W. Busza and A. S. Goldhaber, *Phys. Lett.* **139B** (1984) 235.

[Cas 81] D. G. Cassel and H. Kowalski, *Nucl. Instrum. Methods* **185** (1981) 235.

[Cha 91] S. Chapman and M. Gyulassy, *Phys. Rev. Lett.* **67** (1991) 1210.

[Cha 92] S. Chapman and M. Gyulassy, *Phys. Rev. C* **45** (1992) 2952.

[Col 93] B. A. Cole for the E802 Collaboration in HIPAGS '93, Proceedings of Heavy Ion Physics at the AGS, Cambridge, Mass., 1993, edited by G. S. F. Stephans, S. G. Steadman and W. L. Kehoe (MITLNS–2158), p. 313.

[Cos 90] J. B. Costales, Ph. D. dissertation, MIT, 1990.

[Dat 85] S. Daté, M. Gyulassy and H. Sumiyoshi, *Phys. Rev. D* **32** (1985) 619.

[Dee 93] J. Dee for the E814 Collaboration in HIPAGS '93 (MITNLS–2158), p. 47.

[Eis 92a] S. E. Eiseman *et al.* (The E810 Collaboration), *Phys. Lett. B* **292** (1992) 10.

[Eis 92b] S. E. Eiseman *et al.* (The E810 Collaboration), *Phys. Lett. B* **297** (1992) 44.

[Fre 77] B. A. Freedman and L. D. McLerran, *Phys. Rev. D* **16** (1977) 1169.

[Gre 92] S. V. Greene, Ph. D. dissertation, Yale University, 1992.

[Hac 89] R. W. Hackenburg, The BNL Cross Assembler for the SSP, User's Guide, MPS Note 85 (1989); BNL Access Routines for the SSP, User's Guide, MPS Note 86 (1989).

[Hem 93] T. K. Hemmick for the E814 Collaboration in *Quark Matter '93,* Proceedings of the Tenth International Conference on Ultra-relativistic Nucleus-Nucleus Collisions, Borlänge, Sweden, 1993, edited by E. Stenlund *et al., Nucl. Phys.* **A566** (1994) 435c.

[Jac 75] J. D. Jackson, *Classical Electrodynamics,* second ed. (Wiley, New York, 1975) 848 pp.

[Jah 92] A. Jahns, H. Sorge, H. Stöcker and W. Greiner, *Z. Phys. A* **341** (1992) 243 and private communication.

[Kap 79] J. I. Kapusta, *Nucl. Phys.* **B148** (1979) 461.

[Kat 86] M. Kataja, P. V. Ruuskanen, L. McLerran and H. von Gersdorff, *Phys. Rev. D* **34** (1986) 2755.

[Pan 92] Y. Pang, T. J. Schlagel and S. H. Kahana, *Phys. Rev. Lett.* **68** (1992) 2743 and private communication.

[Par 92] C. G. Parsons, Ph. D. dissertation, MIT, 1992.

[Par 93] C. G. Parsons for the E802 Collaboration in HIPAGS '93 (MITLNS-2158), p. 72.

[Qua 82a] *Quark Matter Formation and Heavy Ion Collisions,* Proceedings of the Bielefeld Workshop, Bielefeld, Germany, 1982, edited by M. Jacob and H. Satz (World Scientific, Singapore, 1982), 586 pp.

[Qua 82b] "Quark matter formation and heavy ion collisions," edited by M. Jacob and J. Tran Thanh Van, *Phys. Reports* **88** (1982) 321.

[Raf 81] J. Rafelski and R. Hagedorn in *Thermodynamics of Quarks and Hadrons,* edited by H. Satz (North-Holland, Amsterdam, 1981).

[Rev 94] "Review of Particle Properties," *Phys. Rev. D* **50** (1994) Part I.

[Ruu 88] P. V. Ruuskanen, *Z. Phys. C* **38** (1988) 219.

[Sch 92] T. J. Schlagel, S. H. Kahana and Y. Pang, *Phys. Rev. Lett.* **69** (1992) 3290.

[Shu 79] E. V. Shuryak, *Phys. Lett.* **81B** (1979) 65.

[Shu 80] E. V. Shuryak, *Phys. Reports* **61** (1980) 71.

[Sor 89] H. Sorge, H. Stöcker and W. Greiner, *Ann. Phys. (NY)* **192** (1989) 266.

[Sor 90] H. Sorge, A. von Keitz, R. Mattiello, H. Stöcker and W. Greiner, *Phys. Lett. B* **243** (1990) 7.

[Sta 92] J. Stachel and G. R. Young, *Annu. Rev. Nucl. Part. Sci.* **42** (1992) 537.

[Sta 93] J. Stachel for the E814 Collaboration in *Quark Matter '93, Nucl. Phys.* **A566** (1994) 183c.

[Van 82] L. van Hove, *Phys. Lett. B* **118** (1982) 138.

[Xu priv] N. Xu (private communication).

Appendix A

The Rapidity Variable

Consider a spacetime with "1 + 1" dimensions—*i. e.,* one space and one time dimension. This is a Minkowski space, with a metric $ds^2 = dt^2 - dx^2$ (we use units where the speed of light $c = 1$). The relative minus sign between the space and time terms gives the Minkowski space a hyperbolic character. In a two-dimensional Euclidean space, the set of all points a given distance r from the origin is a circle (see Fig. A.1). In our Minkowski space, the set of all points with the same *interval* $I \equiv t^2 - x^2$ from the origin is a hyperbola. If the interval is timelike ($I > 0$) the hyperbola intersects the t axis. If the interval is spacelike ($I < 0$) the hyperbola intersects the x axis. If the interval is 0, the hyperbola is the light "cone."

Compare now a rotation in the Euclidean space with a Lorentz transformation in the Minkowski space (see Fig. A.2). If we rotate the Euclidean x-y space through an angle θ, we have

$$x' = x\cos\theta + y\sin\theta \tag{A.1}$$

$$y' = -x\sin\theta + y\cos\theta. \tag{A.2}$$

Figure A.1: (a) A circle in Euclidean space. (b) Two hyperbolae in Euclidean space, one with positive, one with negative interval I. The dashed diagonal lines illustrate the light "cone" ($I = 0$).

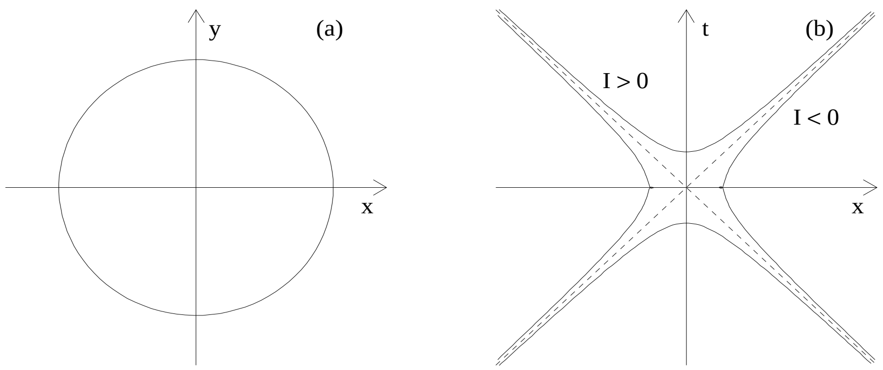

If we perform a Lorentz transformation on the Minkowski space to a frame moving with velocity v, we have

$$t' = \gamma(t - vx) \tag{A.3}$$

$$x' = \gamma(x - vt), \tag{A.4}$$

where $\gamma \equiv (1 - v^2)^{-\frac{1}{2}}$. If we define y such that $\tanh y \equiv v$, we have $\cosh y = \gamma$, $\sinh y = \gamma v$ and we can rewrite (A.3) and (A.4) as

$$t' = t\cosh y - x\sinh y \tag{A.5}$$

$$x' = -t\sinh y + x\cosh y \tag{A.6}$$

in analogy with (A.1) and (A.2). Further, in the Euclidean case, $\tan\theta$ is the slope of the x' axis in the x-y coordinate system; in the Minkowski case,

Figure A.2: (a) A rotation in Euclidean space. (b) A Lorentz boost in Minkowski space.

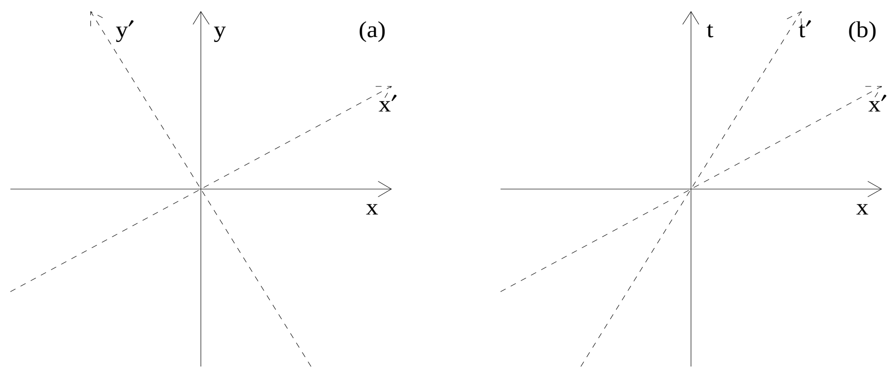

$\tanh y = v = dx/dt$, the "slope" of the t' axis in the t-x reference frame. These observations justify interpreting a Lorentz transformation as the Minkowski equivalent of a rotation. In addition, the parameter y is the Minkowski equivalent of a rotation angle.

Now consider a momentum four-vector p. We can define a velocity three-vector $\mathbf{v} \equiv \mathbf{p}/E$. We define the *rapidity* y of the four-vector with respect to the z axis:

$$y \equiv \operatorname{arctanh} v_z. \tag{A.7}$$

We can similarly define rapidities with respect to other axes; typically we refer to the z axis. Note that if $y > 0$, $v_z > 0$ and if $y < 0$, $v_z < 0$; $y = 0$ implies $v_z = 0$, so in this case the spatial part of the four-vector is normal to the z axis (v doesn't necessarily have to be 0). We also note that in the nonrelativistic limit, $y \to v_z$. If we define the *transverse momentum* $p_t \equiv \sqrt{p_x^2 + p_y^2}$ and the *transverse mass* $m_t \equiv \sqrt{m^2 + p_t^2}$ that correspond to this four-vector, we have two useful identities:

$$\begin{aligned} E &= m_t \cosh y \qquad \text{(A.8)} \\ p_z &= m_t \sinh y. \qquad \text{(A.9)} \end{aligned}$$

We can rewrite (A.7) in several ways, including

$$y = \frac{1}{2} \ln \left(\frac{E + p_z}{E - p_z} \right) \qquad \text{(A.10)}$$

and

$$y = \operatorname{arctanh} (v \cos \theta) \qquad \text{(A.11)}$$

where θ is the usual polar angle. Equation (A.11) demonstrates that y is not only a function of v, but also of θ. In particular, if we consider a massless particle, $v = 1$ and $\tanh y = \cos \theta$. In this case, the rapidity is just a measure of the angle θ. Even for a massive particle, we can define an analogous quantity, the *pseudorapidity* η :

$$\eta \equiv \operatorname{arctanh} \cos \theta. \qquad \text{(A.12)}$$

This is equivalent to $\eta = -\ln \tan \frac{\theta}{2}$. The pseudorapidity η is only a function of the angle θ, even when $v \neq 1$. If $\eta > 0$, $0 < \theta < \frac{\pi}{2}$ and if $\eta < 0$, $\frac{\pi}{2} < \theta < \pi$. If $\eta = 0$, $\theta = \frac{\pi}{2}$, so the corresponding vector is perpendicular to the z axis. The variables η and y always satisfy the following inequality:

$$|\eta| \geq |y| \qquad \text{(A.13)}$$

where the equality obtains if and only if $v = 1$ ($m = 0$).

Now we perform a Lorentz transformation on the four-vector p. If we transform to a frame moving with velocity $\mathbf{u} = u\hat{z}$, where $u = \tanh y_0$, we obtain a new four-vector p'. We can define a new velocity $\mathbf{v}' \equiv \mathbf{p}'/E'$ and a new rapidity $y' \equiv \operatorname{arctanh} v'_z$. This new rapidity satisfies

$$y' = y - y_0. \tag{A.14}$$

Hence, if we perform a Lorentz transformation, we only shift all rapidities by a constant, y_0; *i. e.,* rapidities add like angles. In particular, this means that an increment of rapidity dy is invariant under Lorentz transformations, and hence any rapidity distribution dN/dy is Lorentz invariant. *i. e.:*

$$\frac{dN}{dy'}(y' = y - y_0) = \frac{dN}{dy}(y). \tag{A.15}$$

We now consider the transformation properties of a distribution in three-dimensional momentum space, d^3N/d^3p. If we perform a Lorentz transformation to a frame moving with velocity $\mathbf{v} = v\hat{z}$, dp_x and dp_y (and in fact p_x and p_y) are invariant. We know that $p'_z = \gamma(p_z - vE)$, so

$$dp'_z = \gamma(dp_z - vdE). \tag{A.16}$$

Since $E = \sqrt{m_t^2 + p_z^2}$ and m_t is held fixed, $dE = p_z dp_z/E$. Finally, using $E' = \gamma(E - vp_z)$, we find

$$\frac{dp'_z}{E'} = \frac{dp_z}{E}, \tag{A.17}$$

so dp_z/E is Lorentz invariant. However, $dp_z/E = dy$, so this comes as no surprise, since we already observed that dy is Lorentz invariant. If we use the definitions of p_t and m_t and define $\varphi = \arctan(p_y/p_x)$, we can write

$$E\frac{d^3N}{d^3p} = \frac{1}{p_t}\frac{d^3N}{dp_t d\varphi dy} \tag{A.18}$$

$$= \frac{1}{m_t}\frac{d^3N}{dm_t d\varphi dy}, \tag{A.19}$$

each of which is Lorentz invariant. The latter two forms are obviously invariant under transformations in the z direction, since dy and the transverse degrees of freedom are all invariant; the first form is manifestly rotation-invariant, however, so all three forms are in fact invariant under Lorentz transformations in *any* direction. If we assume azimuthal symmetry—*i. e.,* no dependence on φ—we can integrate these distributions over φ to obtain:

$$E\frac{d^3N}{d^3p} = \frac{1}{2\pi p_t}\frac{d^2N}{dp_t dy} \tag{A.20}$$

$$= \frac{1}{2\pi m_t}\frac{d^2N}{dm_t dy}. \tag{A.21}$$

Appendix B

Rapidity Distributions From an Isotropic Thermal Source

Assume an isotropic thermal source in its center-of-momentum frame

$$\frac{d^3P}{d^3p} = Ae^{-\frac{E}{T}} \tag{B.1}$$

where d^3P/d^3p is the probability distribution in momentum space. Expressed in terms of rapidity and transverse mass, we have

$$\frac{d^2P}{dm_t\,dy} = A'm_t^2 \cosh y \, \exp\left(-\frac{m_t \cosh y}{T}\right). \tag{B.2}$$

Performing the integral over m_t, we find

$$\frac{dP}{dy} = Ce^{-\alpha}\left(1 + \frac{2}{\alpha} + \frac{2}{\alpha^2}\right) \tag{B.3}$$

where

$$\alpha = \frac{m}{T}\cosh y. \tag{B.4}$$

This distribution resembles a Gaussian near its peak. To find the effective Gaussian width σ_{eff}, we expand near $y = 0$. We note that a Gaussian near the peak is well approximated by

$$c\exp\left(-\frac{1}{2}\frac{y^2}{\sigma^2}\right) \approx c - \frac{c}{2}\frac{y^2}{\sigma^2}. \tag{B.5}$$

Equation (B.3) defines dP/dy as a function $h(y)$, the Maclaurin expansion of which yields

$$h(y) = h(0) + h'(0)y + \frac{1}{2}h''(0)y^2 + \mathcal{O}(y^3). \tag{B.6}$$

Comparison of Eqs. (B.5) and (B.6) yields a formula for σ_{eff} :

$$\sigma_{\text{eff}} = \sqrt{-\frac{h(0)}{h''(0)}}. \tag{B.7}$$

The function $h(y)$ is equal to $f(\alpha)$, where f is defined by Eq. (B.3). Rewriting Eq. (B.7) in terms of f, and defining $\alpha_0 \equiv m/T$, we find

$$\sigma^2_{\text{eff}} = -\frac{f(\alpha_0)}{\alpha_0 f'(\alpha_0)}. \tag{B.8}$$

Taking the derivative of f, we find

$$\sigma^2_{\text{eff}} = \frac{\alpha_0^2 + 2\alpha_0 + 2}{\alpha_0^3 + 2\alpha_0^2 + 4\alpha_0 + 4}. \tag{B.9}$$

For nucleons, *e. g.*, ($m = 0.94$ GeV/c^2) with $T = 0.14$ GeV, $\alpha_0 = 6.7$, so $\sigma_{\text{eff}} = 0.38$.

As $\alpha_0 = m/T \to 0$, (T much larger than m) α becomes arbitrarily small at any value of y. The leading term in Eq. (B.3) is then of order α^{-2}, so

$$h(y) = \frac{dP}{dy} \propto \frac{1}{\cosh^2 y}. \tag{B.10}$$

Taking the second derivative of Eq. (B.10) we find $\sigma_{\text{eff}} = 1/\sqrt{2} \approx 0.71$. We also obtain this value by setting α_0 to 0 in Eq. (B.9). This is the limiting value of σ_{eff}, beyond which it never increases, though the function described by Eq. (B.10) has long non-Gaussian tails.

Note that in any isotropic distribution $dP/d\Omega$, the solid angle distribution, is constant. This is proportional to $dP/(\sin\theta d\theta)$. Hence

$$\frac{dP}{d\eta} \propto \frac{1}{\cosh^2\eta}. \tag{B.11}$$

For massless particles $y = \eta$, and for ultrarelativistic particles $y \approx \eta$, so (B.10) is simply a consequence of isotropy in the ultrarelativistic limit.

Appendix C

Transverse Momentum Peaks

Transverse momentum spectra of massive particles at fixed rapidity in heavy ion collisions are often parametrized either as

$$\frac{d^2N}{dp_t dy} = A_B(y) p_t m_t \exp\left(-\frac{m_t}{T_B(y)}\right) \tag{C.1}$$

or as

$$\frac{d^2N}{dp_t dy} = A_0(y) p_t \exp\left(-\frac{m_t}{T_0(y)}\right), \tag{C.2}$$

where $m_t \equiv \sqrt{p_t^2 + m^2}$ is the particle's transverse mass and m is its mass. From now on we will only consider fixed rapidity, so we will suppress the rapidity arguments to the A's and T's.

In each case, one can take a derivative with respect to p_t and set it equal to 0 to find a condition for an extremum in $d^2N/dp_t dy$. In each case this is a maximum. After some algebra, we find:

$$m_t^3 - 2T_B m_t^2 - m^2 m_t + m^2 T_B = 0 \tag{C.3}$$

and

$$m_t^2 - T_0 m_t - m^2 = 0, \tag{C.4}$$

where m_t is the value of transverse mass at which the spectrum peaks.

If we measure the position of this peak, we can immediately find the values of T_B and T_0 :

$$\begin{aligned} T_B &= m_t \frac{m_t^2 - m^2}{2m_t^2 - m^2} && \text{(C.5)} \\ &= m_t \frac{p_t^2}{p_t^2 + m_t^2} && \text{(C.6)} \end{aligned}$$

and

$$T_0 = \frac{p_t^2}{m_t}, \tag{C.7}$$

where $p_t = \sqrt{m_t^2 - m^2}$ is the value of transverse momentum at which the spectrum peaks.

If instead we determine the parameters T_B and T_0 via other methods (*e. g.,* least-squares fits) and wish to determine the corresponding most likely transverse momentum, we must solve Eqs. (C.3) and (C.4) for m_t. Equation (C.4) is quadratic in m_t and hence easily solved:

$$m_t = \frac{1}{2}T_0 + \sqrt{\frac{1}{4}T_0^2 + m^2}, \tag{C.8}$$

yielding

$$p_t^2 = T_0 \left(\frac{1}{2}T_0 + \sqrt{\frac{1}{4}T_0^2 + m^2} \right) \tag{C.9}$$

for the most likely transverse momentum. Combining Eqs. (C.8) and (C.9) yields Eq. (C.7).

Equation (C.3) is cubic in m_t, however. While a solution exists for arbitrary cubic equations,[1] its closed form is complicated and not very instructive.

[1]See, *e. g.,* Birkhoff and Mac Lane [Bir 53], p. 112 ff.

In the case of protons and deuterons, however, both T_B and T_0 are much smaller than the masses of these particles, so it makes sense to solve Eq. (C.3) by expanding in orders of $\tau_B \equiv T_B/m$. If we define $\epsilon \equiv m_t/m - 1$, we can immediately solve Eq. (C.3) to leading order in τ_B :

$$\epsilon = \frac{\tau_B}{2}, \tag{C.10}$$

leading eventually to

$$p_t = \sqrt{mT_B}. \tag{C.11}$$

Interestingly enough, we arrive at a similar solution by expanding (C.9) in orders of $\tau_0 \equiv T_0/m$:

$$p_t = \sqrt{mT_0}. \tag{C.12}$$

If inverted, these would yield identical values for T_B and T_0, which we know from Eqs. (C.5), (C.6) and (C.7) to be slightly different. To take this difference into account, we must expand Eqs. (C.3) and (C.9) to the next higher order in τ_B, τ_0 and ϵ, all of which are of the same order [*cf.* Eq. (C.10)]. Equation (C.3) becomes

$$3\epsilon^2 + 2(1 - 2\tau_B)\epsilon - \tau_B = 0, \tag{C.13}$$

which ultimately yields

$$p_t = \sqrt{mT_B}\left(1 + \frac{3}{4}\frac{T_B}{m}\right). \tag{C.14}$$

If we similarly expand Eq. (C.9), we find

$$p_t = \sqrt{mT_0}\left(1 + \frac{1}{4}\frac{T_0}{m}\right). \tag{C.15}$$

If we equate the values of p_t yielded by Eqs. (C.14) and (C.15), we can find a relation between T_B and T_0, valid as long as these parameters are much smaller than the relevant particle masses:

$$T_0 = T_B \left(1 + \frac{T_B}{m}\right) \tag{C.16}$$

or equivalently

$$T_B = T_0 \left(1 - \frac{T_0}{m}\right) . \tag{C.17}$$

For protons with $T_B = 140$ MeV, *e. g.,* we find $T_0 - T_B \approx 20$ MeV. This result is obtained only via the location of the peak in the transverse momentum spectrum, but it agrees reasonably with values obtained via other methods, *e. g.* via fitting different functions to the entire spectrum.[2]

[2]See, *e. g.,* Ch. 5 and Ref. [Par 92].

Appendix D

Units of Momentum and Magnetic Rigidity

Consider a particle of charge q and momentum $\mathbf{p}$ traveling in a circle of radius R in a uniform magnetic field $\mathbf{B}$. The vectors $\mathbf{p}$ and $\mathbf{B}$ are orthogonal and their magnitudes are p and B, respectively. These quantities, when measured in SI (MKS) units, are related by

$$p = |q|BR. \tag{D.1}$$

If we multiply both sides of (D.1) by the speed of light c and divide by e, the charge on the proton, we find

$$\frac{pc}{e} = c|Z|BR \tag{D.2}$$

where we have defined $Z \equiv q/e$, the charge number, which is dimensionless. Each side of (D.2) is an energy divided by a charge, or an electric potential, measured in Volts. Numerically, $pc/e = p$ if p is measured in eV/c. Equivalently, we may use units where $e = c$. With this understanding, we can write

$$\frac{p}{|Z|} = cBR \tag{D.3}$$

Table D.1: The speed of light in different units.

value	*unit*
299792458	ms^{-1}
299792458	$(\mathrm{eV}/c)(\mathrm{Tm})^{-1}$
299.792458	$(\mathrm{MeV}/c)(\mathrm{Tm})^{-1}$
0.299792458	$(\mathrm{GeV}/c)(\mathrm{Tm})^{-1}$

where B is measured in Tesla (T) and R in meters (m). The speed of light is measured in m/s and has the exact numerical value 299792458. Equation D.3 allows us also to measure the speed of light in other units, as indicated in Tab. D.1. Because we usually work in units where $c = 1$, we can write, *e. g.:*

$$299.792458 \text{ MeV}/c = 1 \text{ Tm}. \tag{D.4}$$

Since we observed above that we are effectively using units where $e = c$, if we also choose our units such that $c = 1$, then $e = 1$, and we naturally measure charge in units of the proton charge.

Appendix E

Multiple Scattering

Consider a particle with charge number Z, velocity β and momentum p that traverses a medium. For convenience, we divide its trajectory into n segments. It begins at a position (z_0, x_0) and ends at a position (z_n, x_n). At each position (z_i, x_i) it has an angle θ_i. Define $\Delta z_i \equiv z_{i+1} - z_i$ for $i = 0, \ldots, n-1$. Adjacent positions are related by

$$x_{i+1} = x_i + \theta_i \Delta z_i \tag{E.1}$$

for small θ_i. For convenience, we also let $x_0 = z_0 = 0$. The nth position is therefore

$$x_n = \sum_{i=0}^{n-1} \theta_i \Delta z_i. \tag{E.2}$$

Each angle θ_i is related to the next angle by

$$\theta_{i+1} = \theta_i + a_i \tag{E.3}$$

where a_i is a randomly distributed angle whose mean is 0 and whose r. m. s. value is $(13.6\ \text{MeV}/\beta p) Z \sqrt{\Delta z_i / X_i}$, and X_i is the radiation length at the ith position.[1]

So using Eqs. (E.2) and (E.3) and some algebra we find

$$x_n = \theta_0 z_n + \sum_{i=0}^{n-2} a_i (z_n - z_{i+1}). \tag{E.4}$$

Since each of the a_i averages to 0, we have

$$\langle x_n \rangle = \theta_0 z_n \tag{E.5}$$

and

$$(x_n - \langle x_n \rangle)^2 = \sum_{i=0}^{n-2} \sum_{j=0}^{n-2} a_i a_j (z_n - z_{i+1})(z_n - z_{j+1}). \tag{E.6}$$

Since $\langle a_i a_j \rangle = \delta_{ij} \langle a_i^2 \rangle$, we also have for $\Delta x^2 \equiv \left\langle (x_n - \langle x_n \rangle)^2 \right\rangle$

$$\Delta x^2 = \sum_{i=0}^{n-2} \langle a_i^2 \rangle (z_n - z_{i+1})^2. \tag{E.7}$$

Using $\langle a_i^2 \rangle = (13.6 \text{ MeV}/\beta p)^2 Z^2 \Delta z_i / X_i$, we can write this as

$$\Delta x^2 = \left(\frac{13.6 \text{ MeV}}{\beta p} \right)^2 Z^2 \sum_{i=0}^{n-2} (z_n - z_{i+1})^2 \frac{\Delta z_i}{X_i}. \tag{E.8}$$

Taking the limit as each of the Δz_i approaches 0, we obtain an integral

$$\Delta x^2 = \left(\frac{13.6 \text{ MeV}}{\beta p} \right)^2 Z^2 \int_0^z \frac{(z - z')^2}{X(z')} dz' \tag{E.9}$$

where now $z \equiv z_n$ and $X(z')$ is the radiation length at position z'.

If X is piecewise constant, with values X_α in m regions from $z_{\alpha-1}$ to z_α, for $\alpha = 1, \ldots, m$, with $z_m = z$, we have

$$\Delta x^2 = \left(\frac{13.6 \text{ MeV}}{\beta p} \right)^2 Z^2 \frac{1}{3} \sum_{\alpha=1}^{m} \frac{[(z - z_{\alpha-1})^3 - (z - z_\alpha)^3]}{X_\alpha}, \tag{E.10}$$

---

[1] See, *e. g.*, the "Review of Particle Properties" [Rev 94], p. 1253 ff., and references therein.

which can be written

$$\Delta x^2 = \left(\frac{13.6\,Z\ \text{MeV}}{\beta p}\right)^2 \frac{1}{3}\sum_{\alpha=1}^{m} \frac{z_\alpha - z_{\alpha-1}}{X_\alpha} \times \left[3\left(z - \frac{1}{2}(z_\alpha + z_{\alpha-1})\right)^2 + \frac{1}{4}(z_\alpha - z_{\alpha-1})^2\right] \tag{E.11}$$

$$= \frac{1}{3}\sum_{\alpha=1}^{m} \theta_\alpha^2 \left[3\,(z - \bar{z}_\alpha)^2 + \Delta z_\alpha^2\right], \tag{E.12}$$

where $\theta_\alpha \equiv (13.6\,Z\ \text{MeV}/\beta p)\sqrt{(z_\alpha - z_{\alpha-1})/X_\alpha}$ is the r. m. s. scattering angle in the αth scattering medium, $\bar{z}_\alpha \equiv (z_\alpha + z_{\alpha-1})/2$ and $\Delta z_\alpha \equiv (z_\alpha - z_{\alpha-1})/2$. Equation E.12 gives us an *ad hoc* method of reintroducing the logarithmic term in the standard multiple scattering formula, which we could not till now include because of the limit to obtain the integral in Eq. (E.9).

For a single, homogeneous region of length z, Eq. (E.10) reduces to

$$\Delta x^2 = \frac{1}{3}\theta_0^2 z^2 \tag{E.13}$$

where $\theta_0 = (13.6\,Z\ \text{MeV}/\beta p)\sqrt{z/X_0}$ and X_0 is the radiation length of the material. This is equivalent to a single scattering through angle θ at a position $z' = z(1 - \frac{1}{\sqrt{3}})$.

The dependence of θ_0 on z and X_0 suggests a series of independent collisions, each of which alters the angle by an amount with the same standard deviation $\sigma = 13.6\,Z\ \text{MeV}/\beta p$. These standard deviations add in quadrature because the collisions are independent. Finally, $m = \Delta z_\alpha / X_\alpha$ is the mean number of collisions a particle experiences in region α, so the overall r. m. s. deflection will satisfy

$$\theta_{\text{rms}}^2 = m\sigma^2. \tag{E.14}$$

This gives us another means of calculating Δx^2. Before, we broke the particle's trajectory into a series of segments for the sake of taking a limit as the segment size approached zero and writing down an integral. The individual positions (z_i, x_i) did not correspond to individual collisions. This was only a mathematical device. Now we wish to consider a particle undergoing a series of collisions, each of which alters its angle by an amount with standard deviation σ.

So now we consider a series of n collisions. The particle as before starts at the origin: $x_0 = z_0 = 0$. Each collision takes place at a point (z_i, x_i). The particle initially has an angle θ_0, and at each collision point, this is altered by an amount a_{i-1}, so as before

$$x = \theta_0 z + \sum_{i=1}^{n} a_{i-1}(z - z_i) \tag{E.15}$$

$$\langle x \rangle = \theta_0 z \tag{E.16}$$

$$\Delta x^2 = \sum_{i=1}^{n} \langle a_{i-1}^2 \rangle (z - z_i)^2. \tag{E.17}$$

where now (z, x) is the final position of the particle. But now $\langle a_i^2 \rangle$ does not depend on Δz_i. Instead $\langle a_i^2 \rangle$ is just σ^2, so

$$\Delta x^2 = \sigma^2 \sum_{i=1}^{n} (z - z_i)^2. \tag{E.18}$$

We must average over all possible values of z_i to find a useful expression for Δx^2. The probability of interacting in dz is dz/X_0, where X_0 is the radiation length. For now we only consider a uniform medium so X_0 is constant. We can easily generalize the following result. We must integrate over all z_i using weights dz_i/X_0 and multiply by the probability of survival between collisions—e^{-m} where $m = z/X_0$—but then we must divide by the probability of undergoing exactly n collisions in the first place, which is $e^{-m}m^n/n!$. We obtain

$$\Delta x_n^2 = n!\sigma^2 \int_0^z \ldots \int_{z_{n-1}}^z \frac{dz_n \ldots dz_1}{z^n} \sum_{i=1}^n (z - z_i)^2. \tag{E.19}$$

Note that this does not depend on X_0. We have already specified that there will be exactly n collisions in the length z, so the interaction probability does not enter into the computation. Only later when we add terms for different numbers of collisions will X_0 enter again. Also, we have put the subscript n on Δx to indicate that this is specifically for n collisions.

We perform the integrals by making the substitutions $w_i \equiv 1 - z_i/z$, yielding

$$\Delta x_n^2 = n!\sigma^2 z^2 \int_0^1 \ldots \int_0^{w_{n-1}} dw_n \ldots dw_1 \sum_{i=1}^n w_i^2. \tag{E.20}$$

To illustrate the method we will use, let us perform explicitly the integration over w_n :

$$\Delta x_n^2 = n!\sigma^2 z^2 \int_0^1 \ldots \int_0^{w_{n-2}} dw_{n-1} \ldots dw_1 \left(\sum_{i=1}^{n-1} w_i^2 w_{n-1} + \frac{1}{3} w_{n-1}^3 \right). \tag{E.21}$$

We have separated out the term from the sum that contains two factors of w_n where the others contain none and done the integration explicitly. In general, when performing the kth integration (over w_{n-k}) we will begin with an integrand like

$$\frac{1}{k!} \sum_{i=1}^{n-k} w_i^2 w_{n-k}^k + f_k w_{n-k}^{k+2} \tag{E.22}$$

which is equal to

$$\frac{1}{k!} \sum_{i=1}^{n-k-1} w_i^2 w_{n-k}^k + \left(f_k + \frac{1}{k!} \right) w_{n-k}^{k+2}. \tag{E.23}$$

After integration, we will have

$$\frac{1}{(k+1)!}\sum_{i=1}^{n-k-1} w_i^2 w_{n-k-1}^{k+1} + \frac{f_k + \frac{1}{k!}}{k+3} w_{n-k-1}^{k+3} \tag{E.24}$$

which will be the integrand for the $(k+1)$th integration. If we substitute $k+1$ for k in the expression (E.22) and equate with the expression (E.24), we find a recursion relation for the f_k's:

$$f_{k+1} = \frac{f_k + \frac{1}{k!}}{k+3}. \tag{E.25}$$

From Eq. (E.21) we can see that $f_1 = \frac{1}{3}$. By inspection we find that $f_k = 1/[3(k-1)!]$ satisfies both the initial condition $f_1 = \frac{1}{3}$ and the recursion Eq. (E.25).

We will perform the last integration when $k = n-1$. Then we will have

$$\begin{aligned} \Delta x_n^2 &= n!\sigma^2 z^2 \int_0^1 \left(\frac{1}{3(n-2)!} + \frac{1}{(n-1)!}\right) w_1^{n+2} dw_1 && \text{(E.26)} \\ &= \frac{n}{3}\sigma^2 z^2. && \text{(E.27)} \end{aligned}$$

The overall variance of the position x is

$$\begin{aligned} \Delta x^2 &= e^{-m}\sum_{n=1}^{\infty}\frac{m^n}{n!}\Delta x_n^2 && \text{(E.28)} \\ &= \frac{m}{3}\sigma^2 z^2 e^{-m}\sum_{n=1}^{\infty}\frac{m^{n-1}}{(n-1)!} && \text{(E.29)} \\ &= \frac{m}{3}\sigma^2 z^2. && \text{(E.30)} \end{aligned}$$

where $m = z/X_0$ is the mean number of collisions and we have weighted all terms specified in Eq. (E.27) by their Poisson probabilities. This is exactly the result we found previously, in Eq. (E.13), *e. g.*

Appendix F

Data Tables

The following tables list numerical values of proton inverse slope parameters T_B and T_0, as shown in Figs. 5.9 and 5.10, proton rapidity distributions, as shown in Figs. 6.1 and 6.4, and low-transverse-momentum deuteron-proton ratios, as shown in Fig. 7.4, for both targets and all centralities. Proton rapidity distributions are computed using extrapolation B in the midrapidity region (see Figs. 5.9 and 5.10).

Table F.1: Si + Al, $60 \leq N_c < 80$

y	T_B (MeV)	T_0 (MeV)	dN_p/dy	dN_d/dN_p (%)
1.0–1.2			7.995 ± 0.786	2.2 ± 0.4
1.2–1.4			6.506 ± 0.443	1.9 ± 0.4
1.4–1.6			6.061 ± 0.372	1.1 ± 0.2
1.6–1.8			6.265 ± 0.249	1.5 ± 0.2
1.8–2.0			6.788 ± 0.202	1.3 ± 0.1
2.0–2.2			7.385 ± 0.193	1.7 ± 0.2
2.2–2.4			6.793 ± 0.120	
2.4–2.6	161.6 ± 7.6	192.5 ± 10.7	7.331 ± 0.126	
2.6–2.8	120.9 ± 2.3	136.7 ± 2.9	6.754 ± 0.114	
2.8–3.0	125.0 ± 1.7	141.3 ± 2.1	6.798 ± 0.076	
3.0–3.2	112.4 ± 1.8	125.0 ± 2.3	6.009 ± 0.063	
3.2–3.4	94.1 ± 1.3	102.8 ± 1.6	6.253 ± 0.052	
3.4–3.6	88.6 ± 1.6	96.3 ± 1.9	4.584 ± 0.038	
3.6–3.8	82.8 ± 5.7	90.1 ± 6.7	1.548 ± 0.097	
3.8–4.0	49.9 ± 13.1	52.6 ± 14.6	0.575 ± 0.071	

Table F.2: Si + Al, $80 \leq N_c < 100$

y	T_B (MeV)	T_0 (MeV)	dN_p/dy	dN_d/dN_p (%)
1.0–1.2			8.213 ± 1.680	2.6 ± 1.0
1.2–1.4			9.671 ± 1.174	2.1 ± 0.6
1.4–1.6			8.452 ± 0.955	2.3 ± 0.8
1.6–1.8			7.788 ± 0.551	1.5 ± 0.4
1.8–2.0			7.691 ± 0.442	1.5 ± 0.3
2.0–2.2			8.681 ± 0.363	1.3 ± 0.3
2.2–2.4			7.223 ± 0.240	
2.4–2.6	160.8 ± 14.5	191.4 ± 20.5	7.808 ± 0.318	
2.6–2.8	134.6 ± 5.2	154.4 ± 6.9	7.688 ± 0.251	
2.8–3.0	124.9 ± 3.3	141.2 ± 4.3	6.875 ± 0.148	
3.0–3.2	120.4 ± 4.2	135.0 ± 5.3	5.787 ± 0.120	
3.2–3.4	92.5 ± 2.8	100.9 ± 3.3	5.555 ± 0.095	
3.4–3.6	88.1 ± 3.5	95.8 ± 4.1	3.817 ± 0.068	
3.6–3.8	77.6 ± 11.6	84.0 ± 13.6	1.182 ± 0.052	
3.8–4.0	30.4 ± 13.6	31.4 ± 14.5	0.321 ± 0.083	

Table F.3: Si + Pb, $100 \leq N_c < 120$

y	T_B (MeV)	T_0 (MeV)	dN/dy	dN_d/dN_p (%)
1.0–1.2			18.184 ± 1.458	2.8 ± 0.9
1.2–1.4			14.788 ± 1.035	3.8 ± 0.8
1.4–1.6			13.242 ± 0.771	2.0 ± 0.6
1.6–1.8			10.258 ± 0.551	2.2 ± 0.5
1.8–2.0			9.422 ± 0.498	1.6 ± 0.3
2.0–2.2	156.8 ± 36.4	187.0 ± 51.7	8.427 ± 0.380	1.5 ± 0.4
2.2–2.4	148.2 ± 20.2	174.6 ± 28.0	6.553 ± 0.283	
2.4–2.6	157.1 ± 12.5	186.0 ± 17.6	7.146 ± 2.102	
2.6–2.8	124.8 ± 4.7	141.8 ± 6.1	5.108 ± 0.319	
2.8–3.0	122.7 ± 3.4	138.3 ± 4.3	4.527 ± 0.166	
3.0–3.2	107.5 ± 2.7	119.4 ± 3.3	3.418 ± 0.114	
3.2–3.4	97.3 ± 3.0	106.8 ± 3.6	3.240 ± 0.090	
3.4–3.6	84.3 ± 3.4	91.4 ± 4.0	2.177 ± 0.049	
3.6–3.8	48.3 ± 2.0	50.7 ± 2.3	0.531 ± 0.019	
3.8–4.0	26.4 ± 11.6	27.2 ± 12.3	0.021 ± 0.003	

Table F.4: Si + Pb, $120 \leq N_c < 140$

y	T_B (MeV)	T_0 (MeV)	dN/dy	dN_d/dN_p (%)
1.0–1.2			23.426 ± 1.185	2.2 ± 0.3
1.2–1.4			20.713 ± 0.952	3.0 ± 0.6
1.4–1.6			15.809 ± 0.681	2.0 ± 0.2
1.6–1.8			12.787 ± 0.526	1.4 ± 0.1
1.8–2.0			11.035 ± 0.465	1.4 ± 0.1
2.0–2.2	173.3 ± 24.4	211.1 ± 36.1	9.461 ± 0.392	1.7 ± 0.2
2.2–2.4	118.6 ± 7.6	134.9 ± 9.8	6.566 ± 0.246	
2.4–2.6	134.4 ± 5.4	155.0 ± 7.3	5.770 ± 1.014	
2.6–2.8	126.6 ± 2.9	144.0 ± 3.8	4.368 ± 0.193	
2.8–3.0	124.9 ± 2.2	141.2 ± 2.8	3.615 ± 0.099	
3.0–3.2	108.3 ± 1.8	120.4 ± 2.3	2.407 ± 0.064	
3.2–3.4	93.6 ± 2.0	102.3 ± 2.3	2.025 ± 0.041	
3.4–3.6	79.3 ± 2.2	85.5 ± 2.5	1.280 ± 0.022	
3.6–3.8	47.1 ± 1.5	49.4 ± 1.6	0.292 ± 0.009	
3.8–4.0	32.1 ± 13.0	33.2 ± 13.9	0.011 ± 0.001	

Table F.5: Si + Pb, $140 \leq N_c < 160$

y	T_B (MeV)	T_0 (MeV)	dN/dy	dN_d/dN_p (%)
1.0–1.2			29.557 ± 1.345	1.6 ± 0.2
1.2–1.4			23.325 ± 1.005	1.9 ± 0.2
1.4–1.6			17.061 ± 0.703	1.7 ± 0.2
1.6–1.8			13.901 ± 0.552	1.2 ± 0.1
1.8–2.0			12.116 ± 0.497	1.2 ± 0.1
2.0–2.2	130.4 ± 12.4	150.7 ± 16.6	9.611 ± 0.392	1.5 ± 0.2
2.2–2.4	135.1 ± 8.4	156.6 ± 11.3	6.838 ± 0.248	
2.4–2.6	130.6 ± 4.8	150.1 ± 6.4	5.226 ± 0.880	
2.6–2.8	132.5 ± 3.0	151.6 ± 3.9	3.810 ± 0.179	
2.8–3.0	126.3 ± 2.3	142.9 ± 2.9	2.699 ± 0.076	
3.0–3.2	111.0 ± 2.1	123.8 ± 2.6	1.587 ± 0.045	
3.2–3.4	103.4 ± 2.7	114.1 ± 3.2	1.124 ± 0.029	
3.4–3.6	89.0 ± 3.3	96.9 ± 3.9	0.610 ± 0.013	
3.6–3.8	51.6 ± 2.2	54.4 ± 2.4	0.127 ± 0.006	
3.8–4.0	38.3 ± 22.7	39.9 ± 24.7	0.004 ± 0.001	

Table F.6: Si + Pb, $160 \leq N_c < 180$

y	T_B (MeV)	T_0 (MeV)	dN/dy	dN_d/dN_p (%)
1.0–1.2			32.580 ± 1.627	1.5 ± 0.4
1.2–1.4			26.358 ± 1.220	1.8 ± 0.3
1.4–1.6			18.587 ± 0.815	1.6 ± 0.3
1.6–1.8			14.803 ± 0.618	1.4 ± 0.2
1.8–2.0			12.749 ± 0.523	1.0 ± 0.2
2.0–2.2	147.1 ± 19.7	173.4 ± 27.4	9.723 ± 0.383	1.2 ± 0.3
2.2–2.4	124.1 ± 9.3	142.1 ± 12.2	6.642 ± 0.245	
2.4–2.6	128.8 ± 6.1	147.7 ± 8.0	4.950 ± 0.929	
2.6–2.8	126.0 ± 3.8	143.3 ± 4.9	3.268 ± 0.171	
2.8–3.0	125.6 ± 3.2	142.0 ± 4.1	2.233 ± 0.080	
3.0–3.2	112.3 ± 3.3	125.4 ± 4.1	1.218 ± 0.045	
3.2–3.4	105.0 ± 4.4	116.1 ± 5.4	0.763 ± 0.030	
3.4–3.6	83.3 ± 5.1	90.3 ± 6.0	0.393 ± 0.016	
3.6–3.8	61.2 ± 5.1	65.2 ± 5.8	0.078 ± 0.012	
3.8–4.0	8.1 ± 3.1	8.2 ± 3.2	0.002 ± 0.001	

Table F.7: Si + Pb, $180 \leq N_c < 200$

y	T_B (MeV)	T_0 (MeV)	dN/dy
1.6–1.8			14.714 ± 0.988
1.8–2.0			13.598 ± 1.004
2.0–2.2	143.7 ± 45.9	168.7 ± 63.2	10.656 ± 0.610
2.2–2.4	137.2 ± 30.7	159.4 ± 41.4	5.987 ± 0.372
2.4–2.6	140.8 ± 18.8	163.6 ± 25.3	5.248 ± 2.323
2.6–2.8	148.6 ± 14.2	173.3 ± 19.4	3.295 ± 0.640
2.8–3.0	137.3 ± 10.6	157.3 ± 13.9	2.078 ± 0.208
3.0–3.2	120.4 ± 10.8	135.6 ± 13.7	0.978 ± 0.152
3.2–3.4	115.5 ± 18.0	129.2 ± 22.5	0.640 ± 0.120
3.4–3.6			0.298 ± 0.029
3.6–3.8			0.076 ± 0.027
3.8–4.0			0.001 ± 0.001